Atmos. Meas. Tech., 11, 4171–4215, 2018
https://doi.org/10.5194/amt-11-4171-2018

Atmospheric Measurement Techniques
Open Access
EGU

The MUSICA IASI CH_4 and N_2O products and their comparison to HIPPO, GAW and NDACC FTIR references

Omaira E. García[1], Matthias Schneider[2], Benjamin Ertl[2,3], Eliezer Sepúlveda[4,1], Christian Borger[2,a], Christopher Diekmann[2], Andreas Wiegele[2], Frank Hase[2], Sabine Barthlott[2], Thomas Blumenstock[2], Uwe Raffalski[5], Angel Gómez-Peláez[1,b], Martin Steinbacher[6], Ludwig Ries[7], and Angel M. de Frutos[4]

[1]Izaña Atmospheric Research Centre (IARC), Meteorological State Agency of Spain (AEMET), Santa Cruz de Tenerife, Spain
[2]Institute of Meteorology and Climate Research (IMK-ASF), Karlsruhe Institute of Technology (KIT), Karlsruhe, Germany
[3]Steinbuch Centre for Computing (SCC), Karlsruhe Institute of Technology, Karlsruhe, Germany
[4]Atmospheric Optics Group (GOA), University of Valladolid, Valladolid, Spain
[5]Swedish Institute of Space Physics, Kiruna, Sweden
[6]Swiss Federal Laboratories for Materials Science and Technology (Empa), Dübendorf, Switzerland
[7]Platform Zugspitze of GAW Global Observatory Zugspitze/Hohenpeissenberg, Federal Environmental Agency (UBA), Zugspitze, Germany
[a]now at: Satellite Remote Sensing Group, Max Planck Institute for Chemistry, Mainz, Germany
[b]now at: Meteorological State Agency of Spain (AEMET), Delegation in Asturias, Oviedo, Spain

Correspondence: Omaira E. García (ogarciar@aemet.es) and Matthias Schneider (matthias.schneider@kit.edu)

Received: 3 October 2016 – Discussion started: 18 January 2017
Revised: 16 June 2018 – Accepted: 19 June 2018 – Published: 18 July 2018

Abstract. This work presents the methane (CH_4) and nitrous oxide (N_2O) products as generated by the IASI (Infrared Atmospheric Sounding Interferometer) processor developed during the project MUSICA (MUlti-platform remote Sensing of Isotopologues for investigating the Cycle of Atmospheric water). The processor retrieves CH_4 and N_2O with different water vapour and water vapour isotopologues (as well as HNO_3) and uses a single a priori data set for all the retrievals (no variation in space and time). Firstly, the characteristics and errors of the products are analytically described. Secondly, the products are comprehensively evaluated by comparisons to the following reference data measured by different techniques and from different platforms as follows: (1) aircraft CH_4 and N_2O profiles from the five HIAPER Pole-to-Pole Observation (HIPPO) missions; (2) continuous in situ CH_4 and N_2O observations performed between 2007 and 2017 at subtropical and mid-latitude high-mountain observatories (Izaña Atmospheric Observatory and Jungfraujoch, respectively) in the framework of the WMO–GAW (World Meteorological Organization–Global Atmosphere Watch) programme; (3) ground-based FTIR (Fourier-transform infrared spectrometer) measurements made between 2007 and 2017 in the framework of the NDACC (Network for the Detection of Atmospheric Composition Change) at the subtropical Izaña Atmospheric Observatory, the mid-latitude station of Karlsruhe and the Kiruna polar site.

The theoretical estimations and the comparison studies suggest a precision for the N_2O and CH_4 retrieval products of about 1.5–3 % and systematic errors due to spectroscopic parameters of about 2 %. The MUSICA IASI CH_4 data offer a better sensitivity than N_2O data. While for the latter the sensitivity is mainly limited to the UTLS (upper troposphere–lower stratosphere) region, for CH_4 we are able to prove that at low latitudes the MUSICA IASI processor can detect variations that take place in the free troposphere independently from the variations in the UTLS region. We demonstrate that the MUSICA IASI data qualitatively capture the CH_4 gradients between low and high latitudes and between the Southern Hemisphere and Northern Hemisphere; however, we also

find an inconsistency between low- and high-latitude CH_4 data of up to 5 %. The N_2O latitudinal gradients are very weak and cannot be detected. We make comparisons over a 10-year time period and analyse the agreement with the reference data on different timescales. The MUSICA IASI data can detect day-to-day signals (only in the UTLS), seasonal cycles and long-term evolution (in the UTLS and for CH_4 also in the free troposphere) similar to the reference data; however, there are also inconsistencies in the long-term evolution connected to inconsistencies in the used atmospheric temperature a priori data.

Moreover, we present a method for analytically describing the a posteriori-calculated logarithmic-scale difference of the CH_4 and N_2O retrieval estimates. By correcting errors that are common in the CH_4 and N_2O retrieval products, the a posteriori-calculated difference can be used for generating an a posteriori-corrected CH_4 product with a theoretically better precision than the original CH_4 retrieval products. We discuss and evaluate two different approaches for such a posteriori corrections. It is shown that the correction removes the inconsistencies between low and high latitudes and enables the detection of day-to-day signals also in the free troposphere. Furthermore, they reduce the impact of short-term atmospheric dynamics, which is an advantage, because respective signals are presumably hardly comparable to model data. The approach that affects the correction solely on the scales on which the errors dominate is identified as the most efficient, because it reduces the inconsistencies and errors without removing measurable real atmospheric signals. We give a brief outlook on a possible usage of this a posteriori-corrected MUSICA IASI CH_4 product in combination with inverse modelling.

1 Introduction

After carbon dioxide (CO_2), CH_4 and N_2O are currently the most important well-mixed greenhouse gases (GHGs) as climate-forcing gases. Although they are much less abundant in the atmosphere than CO_2, their global warming potentials are significantly larger: CH_4 and N_2O are about 35 and 300 times, respectively, more efficient than CO_2 in trapping outgoing long-wave radiation, on a 100-year time horizon (Stocker et al., 2013). It is well recognized that the imbalance between their sources and sinks has unquestionably increased during the last few centuries, but the exact location, intensity and nature of CH_4 and N_2O sources and sinks are not as well understood as those for CO_2 (Crevoisier et al., 2009). The knowledge of today's CH_4 and N_2O sources and sinks, their spatial distribution and their variability in time are essential for understanding their role in the carbon and nitrogen cycles and for a reliable prediction of future atmospheric CH_4 and N_2O abundances. The latter is important for predicting radiative forcing as well as ozone recovery (both CH_4 and N_2O act as ozone-depleting substances). Existing observations of fluxes of CH_4 and N_2O from soils and oceans are still insufficient to adequately address these tasks (e.g. Huang et al., 2008; Kort et al., 2011).

Since the late 1980s, surface in situ measurements of CH_4 and N_2O are systematically taken within the WMO–GAW programme (World Meteorological Organization–Global Atmosphere Watch, https://www.wmo.int/, last access: 11 July 2018). These observations have proved to be very precise and, thus, are indispensable inputs for inverse methods and chemical transport models (e.g. Bousquet et al., 2011; Cressot et al., 2014). More recently, ground-based remote sensing FTIR (Fourier-transform infrared spectrometer) experiments have also routinely provided high-quality CH_4 and N_2O concentrations in the framework of the international networks NDACC (Network for the Detection of Atmospheric Composition Change, https://www2.acom.ucar.edu/irwg, last access: 11 July 2018, Schneider et al., 2005; Angelbratt et al., 2011; Sepúlveda et al., 2014; Ostler et al., 2014) and TCCON (Total Carbon Column Observing Network, http://tccon.caltech.edu/, last access: 11 July 2018, Wunch et al., 2011). However, both surface in situ and ground-based remote sensing measurements have limited geographical coverage. In this context, space-based remote sensing instruments have an outstanding importance due to their global coverage, allowing a global monitoring of the GHG distribution and thus improved investigations of sources and sinks and their variation in time and space.

The potential of space-based instruments to observe global CH_4 and N_2O distributions has extensively been reported in literature. Examples of satellite measurements using different spectral ranges and observing geometries are those from Envisat MIPAS (Michelson Interferometer for Passive Atmospheric Sounding, Payan et al., 2009; Plieninger et al., 2015), Envisat SCIAMACHY (SCanning Imaging Absorption SpectroMeter for Atmospheric CHartographY, Frankenberg et al., 2006), SCISAT-1 ACE (Atmospheric Chemistry Experiment, De Mazière et al., 2008), AURA TES (Tropospheric Emission Spectrometer, Wecht et al., 2012; Worden et al., 2012), GOSAT TANSO-FTS (Thermal And Near infrared Sensor for carbon Observation, Yokota et al., 2009) or AQUA AIRS (Atmospheric Infrared Sounder, Xiong et al., 2014, 2015). The thermal nadir instruments have the advantage of observing under a large variety of conditions (day and night, over land and ocean), increasing significantly their global coverage (Clerbaux et al., 2009; Wecht et al., 2012). Among the current thermal nadir sensors, IASI (Infrared Atmospheric Sounding Interferometer, Blumstein et al., 2004) has special relevance, because it combines high spatial coverage and a relatively good temporal resolution (the requirements for weather forecasting) and high spectral resolution (needed for trace gas retrievals) with a long-term data availability. Its mission is guaranteed until 2022 through the meteorological satellites MetOp, the space component of the EUMETSAT (European Orga-

nization for the Exploitation of Meteorological Satellites, https://www.eumetsat.int/website/, last access: 11 July 2018) Polar System (EPS) programme: the first sensor (IASI-A) was launched in October 2006 on-board MetOp-A, the second (IASI-B) was launched in September 2012 on-board MetOp-B and the third (IASI-C) is expected to be launched in October 2018 aboard MetOp-C. For the 2020s IASI-NG instruments (IASI new generation, Crevoisier et al., 2014) are scheduled. IASI-NG has a further-improved spectral resolution and radiometric performance and will be flown on three successive MetOp-SG (second generation) satellites of the EPS-SG system, giving a perspective of data records until the late 2030s. All this is very promising for monitoring atmospheric composition in the long term, and IASI and IASI-NG are key instruments for EUMETSAT's contribution to Copernicus, the European system for monitoring the Earth (e.g. Clerbaux et al., 2009; August et al., 2012).

In the last years, considerable efforts have been made in developing and improving algorithms for the retrieval of CH_4 and N_2O concentrations from IASI spectra. The first approaches provided CH_4 and N_2O observations using neural network schemes, but with a limited precision (e.g. Turquety et al., 2004; Crevoisier et al., 2009; Ricaud et al., 2009). Recently more sophisticated retrievals, based on optimal estimation methods, have been presented (e.g. Xiong et al., 2013; Masiello et al., 2016; De Wachter et al., 2017; Siddans et al., 2017), which are able to provide more precise CH_4 and N_2O estimations and to derive some information about their vertical distribution.

Within the European Research Council project MUSICA (MUlti-platform remote Sensing of Isotopologues for investigating the Cycle of Atmospheric water) an IASI processor has been developed for simultaneously retrieving different water vapour isotopologues, CH_4 and N_2O (Schneider and Hase, 2011; Wiegele et al., 2014; Schneider et al., 2016). In this paper the MUSICA IASI CH_4 and N_2O products are presented, characterized and comprehensively validated by using a multi-platform reference database. As validation references we consider (1) aircraft CH_4 and N_2O profiles from the five HIPPO (HIAPER Pole-to-Pole Observation) missions, (2) continuous in situ CH_4 and N_2O observations recorded within the WMO–GAW programme, and (3) ground-based FTIR measurements taken in the framework of the NDACC. This extensive validation exercise enables us to properly document the quality and long-term consistency of the MUSICA IASI CH_4 and N_2O products as well as their geographical uniformity. Moreover, we discuss and analytically characterize the a posteriori-calculated logarithmic-scale difference between the CH_4 and the N_2O retrieval products. We present two different approaches for this a posteriori calculations and evaluate their usefulness for correcting errors in the CH_4 retrieval product.

The paper is structured as follows: Sect. 2 presents the IASI sensor, the MUSICA IASI CH_4 and N_2O retrieval strategy, and the analytic method for characterizing the CH_4 and N_2O retrieval products as well as the a posteriori-corrected CH_4 product. The CH_4 and N_2O retrieval products as well as the a posteriori-corrected CH_4 product are then characterized in Sect. 3 (by describing vertical sensitivity and estimating errors). Sections 4, 5 and 6 extensively evaluate the data by comparisons to aircraft in situ profiles, continuous surface in situ data and ground-based remote sensing data. In Sect. 7 we discuss and evaluate an alternative a posteriori correction of CH_4 that only addresses the scales on which the errors are dominating and Sect. 8 briefly discusses the possible usage of these observation data in combination with inverse modelling. Section 9 summarizes the main results of this work and gives an outlook on possible future activities.

2 MUSICA IASI processing

2.1 The MetOp-IASI instrument

The IASI sensor is a Fourier-transform spectrometer developed by CNES (Centre National d'Etudes Spatiales, https://cnes.fr/fr, last access: 11 July 2018) in cooperation with EUMETSAT. It is on-board the EUMETSAT MetOp satellites, which operate in a polar low-Earth orbit since 2006. With 14 sun-synchronous orbits per day (09:30 and 21:30 Local Solar Time equator crossing) IASI can provide global observations twice per day. IASI measures thermal infrared radiation emitted by the Earth's surface and the atmosphere between 645 and 2760 cm^{-1} with an apodized spectral resolution of 0.5 cm^{-1} and scans the surface perpendicular to the satellite's flight track with 30 individual views, covering a surface swath width of about 2200 km. Each individual view consists of four individual ground pixels (IFOV) of about 12 km diameter at nadir. The calibrated IASI radiances for these 120 fields of view are disseminated by EUMETSAT as level 1C (L1C), together with additional information about observation geometry.

2.2 Atmospheric remote sensing retrieval principles

In this subsection we give a brief introduction into the analytic description of the remote sensing measurement that is in line with the suggestions of Rodgers (2000) and that follows the notation recommendations of TUNER (Towards Unified Error Reporting, https://www.imk-asf.kit.edu/, last access: 11 July 2018). The text is similar to Borger et al. (2017); however, we think that the repetition here is a very useful reference for this paper.

We measure $\boldsymbol{y}$ (the measurement vector, e.g. a thermal nadir spectrum in the case of IASI) and are interested in $\boldsymbol{x}$ (the atmospheric state vector). This problem can be written as

$$\boldsymbol{y} = \boldsymbol{F}(\boldsymbol{x}, \boldsymbol{b}), \tag{1}$$

where $\boldsymbol{F}$ is the forward model (simulates the interaction of radiation with the atmosphere) and the vector $\boldsymbol{b}$ represents

auxiliary parameters (like surface emissivity) or instrumental characteristics (like the instrumental line shape), which are not part of the retrieval state vector.

A direct inversion of Eq. (1) is generally not possible, because there are many atmospheric states $\boldsymbol{x}$ that can explain the same measurement $\boldsymbol{y}$. For solving this ill-posed problem the solution state is constrained by setting up a cost function:

$$[\boldsymbol{y} - \boldsymbol{F}(\boldsymbol{x}, \boldsymbol{b})]^T \mathbf{S}_{\mathbf{y},\text{total}}{}^{-1} [\boldsymbol{y} - \boldsymbol{F}(\boldsymbol{x}, \boldsymbol{b})] + [\boldsymbol{x} - \boldsymbol{x}_\text{a}]^T \mathbf{S}_\text{a}{}^{-1} [\boldsymbol{x} - \boldsymbol{x}_\text{a}]. \quad (2)$$

Here, the first term is a measure of the difference between the measured spectrum (represented by $\boldsymbol{y}$) and the spectrum simulated for a given atmospheric state (represented by $\boldsymbol{x}$), while taking into account the measurement signal that is not understood by the forward model ($\mathbf{S}_{\mathbf{y},\text{total}}$ is the covariance matrix of $\boldsymbol{y} - \boldsymbol{F}(\boldsymbol{x}, \boldsymbol{b})$). The second term of the cost function (Eq. 2) constrains the atmospheric solution state ($\boldsymbol{x}$) towards an a priori most likely state ($\boldsymbol{x}_\mathbf{a}$), whereby the kind and strength of the constraint are defined by the a priori covariance matrix $\mathbf{S}_\text{a}$. The constrained solution is reached at the minimum of the cost function (Eq. 2).

Due to the nonlinear behaviour of $\boldsymbol{F}(\boldsymbol{x}, \boldsymbol{b})$, the minimization is generally achieved iteratively. For the $(i+1)$th iteration it is

$$\boldsymbol{x}_{\boldsymbol{i+1}} = \boldsymbol{x}_\mathbf{a} + \mathbf{G_i}[\boldsymbol{y} - \boldsymbol{F}(\boldsymbol{x}_i, \boldsymbol{b}) + \mathbf{K_i}(\boldsymbol{x}_i - \boldsymbol{x}_\mathbf{a})]. \quad (3)$$

$\mathbf{K}$ is the Jacobian matrix (derivatives that capture how the measurement vector will change for changes in the atmospheric state $\boldsymbol{x}$). $\mathbf{G}$ is the gain matrix (derivatives that capture how the retrieved state vector will change for changes in the measurement vector $\boldsymbol{y}$). $\mathbf{G}$ can be calculated from $\mathbf{K}$, $\mathbf{S}_{\mathbf{y},\text{total}}$ and $\mathbf{S}_\text{a}$ as

$$\mathbf{G} = (\mathbf{K}^T \mathbf{S}_{\mathbf{y},\text{total}}{}^{-1} \mathbf{K} + \mathbf{S}_\text{a}{}^{-1})^{-1} \mathbf{K}^T \mathbf{S}_{\mathbf{y},\text{total}}{}^{-1}. \quad (4)$$

The averaging kernel is an important component of a remote sensing retrieval product and it is calculated as

$$\mathbf{A} = \mathbf{GK}. \quad (5)$$

The averaging kernel $\mathbf{A}$ reveals how a small change in the real atmospheric state vector $\boldsymbol{x}$ affects the retrieved atmospheric state vector $\hat{\boldsymbol{x}}$:

$$\hat{\boldsymbol{x}} - \boldsymbol{x}_\text{a} = \mathbf{A}(\boldsymbol{x} - \boldsymbol{x}_\text{a}). \quad (6)$$

The propagation of errors due to parameter uncertainties Δb can be estimated analytically with the help of the parameter Jacobian matrix $\mathbf{K_b}$ (derivatives that capture how the measurement vector will change for changes in the parameter $\boldsymbol{b}$). According to Eq. 3, using the parameter $\boldsymbol{b} + \boldsymbol{\Delta b}$ (instead of the correct parameter $\boldsymbol{b}$) for the forward model calculations will result in an error in the atmospheric state vector of

$$\boldsymbol{\Delta}\hat{\boldsymbol{x}} = -\mathbf{GK_b}\boldsymbol{\Delta b}. \quad (7)$$

The respective error covariance matrix $\mathbf{S}_{\hat{\mathbf{x}},\mathbf{b}}$ is

$$\mathbf{S}_{\hat{\mathbf{x}},\mathbf{b}} = \mathbf{GK_b S_b K_b}{}^T \mathbf{G}^T, \quad (8)$$

where $\mathbf{S_b}$ is the covariance matrix of the uncertainties $\boldsymbol{\Delta b}$. Noise on the measured radiances also affects the retrievals. The error covariance matrix for measurement noise ($\mathbf{S}_{\hat{\mathbf{x}},\text{noise}}$) is analytically calculated in analogy to Eq. (8) by $\mathbf{S}_{\hat{\mathbf{x}},\text{noise}} = \mathbf{GS}_{\mathbf{y},\text{noise}}\mathbf{G}^T$, where $\mathbf{S}_{\mathbf{y},\text{noise}}$ is the covariance matrix for noise in the measurement.

Rewriting Eq. (6) and considering the errors $\boldsymbol{\Delta}\hat{\boldsymbol{x}}$, the retrieved state $\hat{\boldsymbol{x}}$ can be written as

$$\hat{\boldsymbol{x}} = \mathbf{A}(\boldsymbol{x} - \boldsymbol{x}_\text{a}) + \boldsymbol{x}_\text{a} + \boldsymbol{\Delta}\hat{\boldsymbol{x}}. \quad (9)$$

2.3 Retrieval setup for CH_4 and N_2O

The MUSICA IASI retrieval focuses on the estimation of tropospheric water vapour concentrations and on the ratio between the isotopologues HDO and H_2O (Schneider and Hase, 2011; Wiegele et al., 2014; Schneider et al., 2015). The retrieval analyses the thermal emission spectra recorded by IASI in the 1190–1400 cm^{-1} spectral region by using the thermal nadir retrieval algorithm PROFFIT-nadir (Schneider and Hase, 2011; Wiegele et al., 2014). The PROFFIT-nadir code has been developed in support of the project MUSICA for analysing thermal nadir spectra and recently updated by including water continuum calculations according to the model MT_CKD v2.5.2 (Mlawer et al., 2012; Delamere et al., 2010; Payne et al., 2011). It is an extension of the PROFFIT code used for many years for analysing high-resolution solar absorption infrared spectra (PROFile Fit, Hase et al., 2004). Our processor is the MUSICA PROFFIT-nadir IASI processor. For simplicity in the following we call it the MUSICA IASI processor.

In the analysed IASI spectral region CH_4 and N_2O have important spectroscopic signatures and are retrieved simultaneously to the water vapour isotopologues. The CH_4 and N_2O VMR (volume mixing ratio) profiles are derived, on a logarithmic scale, using an ad hoc Tikhonov–Phillips constraint (Tikhonov, 1963) that mimics the inverse of a covariance matrix for a 10 % 1σ variability and a correlation length of 1.5 km in the free troposphere, 3 km in the tropopause region and 6 km in the stratosphere. Because the interferences of the water vapour isotopologues are very strong, the application of a sophisticated water vapour isotopologue retrieval method is indicated. The water vapour and water vapour isotopologue concentrations are retrieved by using an optimal estimation approach, whose settings have been described in detail in previous publications (Schneider and Hase, 2011; Wiegele et al., 2014; Schneider et al., 2016; Borger et al., 2017). In addition, the analysed spectral window contains HNO_3 and very weak CO_2 signatures. While HNO_3 is also simultaneously retrieved by a Tikhonov–Phillips constraint, the weak CO_2 signatures are taken into account by scaling a climatological CO_2 profile.

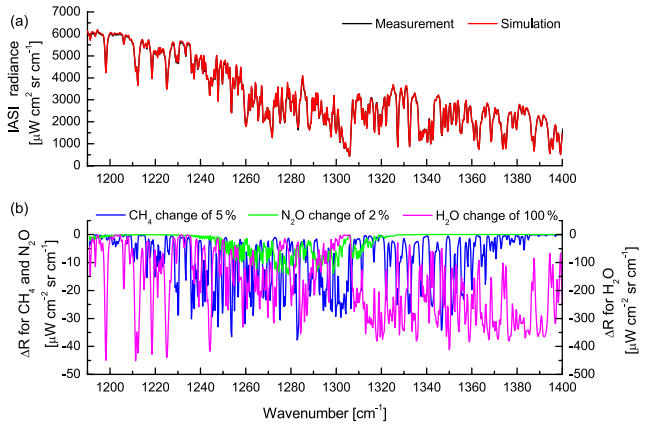

Figure 1. (a) Example of spectral radiances recorded by IASI and the corresponding PROFFIT-nadir simulation over a tropical ocean pixel (≈ 12°S) in winter. **(b)** Spectral changes in the IASI radiance (ΔR) due to a change in CH_4 of 5 %, in N_2O of 2 % and in H_2O of 100 % (please note the different y-axis scale for H_2O).

Figure 1 illustrates why a high-quality water vapour isotopologue retrieval is crucial for obtaining a CH_4 and N_2O product with reasonable quality. The figure shows an example of the radiances measured by IASI and simulated by PROFFIT-nadir in the spectral region used for the CH_4 and N_2O retrievals as well as the change in IASI radiances due to a change in CH_4 by +5 %, in N_2O by +2 % and in H_2O by +100 %, whereby 5, 2 and 100 % are typical values for the respective trace gas variations (please note the different y-axis scale for H_2O spectral signatures). As observed, the spectral signatures of H_2O variations are more than an order of magnitude stronger than the signatures of CH_4 and N_2O variations, indicating that the quality of the CH_4 and N_2O products depends strongly on a correct interpretation of the spectroscopic interferences of the water vapour isotopologues.

For all the fitted species we use a single a priori profile for all retrievals, i.e. the a priori data are the same for different days, seasons, years and locations. Therefore, all the observed atmospheric variations are induced by the IASI measurements and are not affected by varying a priori information (please see also discussion in Appendix A). The a priori profiles of CH_4 and N_2O are typical low-latitude profiles taken from WACCM (Whole Atmosphere Community Climate Model version 5, https://www2.acom.ucar.edu/, last access: 11 July 2018) provided by NCAR (National Center for Atmospheric Research, J. Hannigan, private communication). They are climatologies provided at a spatial resolution of 1.9° × 2.5° and averaged for the 2004–2006 period. The water vapour isotopologue a priori data are averages obtained from the isotopologue incorporated global general circulation model LMDZ (Risi et al., 2012).

The retrieval also fits the surface (skin) temperature and the atmospheric temperature profile, whereby the a priori temperatures are taken from the EUMETSAT IASI level 2 (L2) products and are updated for each IASI retrieval (i.e. they vary with latitude and time for each IASI pixel). Regarding the a priori variability, there is no constraint on the surface temperature. The allowed atmospheric temperature 1σ variations are 1 K at ground, 0.5 K in the free troposphere and 0.75 K above the tropopause. This altitude dependency follows roughly the altitude dependency of uncertainties in the EUMETSAT IASI L2 atmospheric temperature profiles (August et al., 2012). Details on the EUMETSAT L2 Product Processing Facility (PPF) software version changes that can affect the EUMETSAT IASI L2 atmospheric temperatures are listed in Table 1.

For the radiative transfer calculations the spectroscopic line parameters are taken from the HITRAN 2016 database (Gordon et al., 2017) for all the gases, except for the water vapour isotopologues. For the latter we use an improved spectroscopy based on HITRAN 2016, but modifying the line intensities (S) for the HDO absorption signatures by +10 % (Schneider et al., 2016). This modification is introduced to correct the bias documented in the IASI HDO products reported by Schneider et al. (2015).

Ocean emissivities are calculated according to Masuda et al. (1988) for three different wavenumbers enveloping the spectral retrieval range, while emissivities at land are taken from the Global Infrared Land Surface Emissivity Database (Seemann et al., 2008) provided as monthly means by the University of Wisconsin in Madison (http://cimss.ssec.wisc.edu/iremis/, last access: 11 July 2018). The assignation of ground altitude is done using the Global 30-Arc-Second Elevation Data Set (GTOPO30, http://eros.usgs.gov/elevation-products, last access: 11 July 2018). Note that the PROFFIT-nadir retrieval code does not consider the backscatter of solar light at the Earth's surface, but this is not critical for simulating the radiances below 2000 cm^{-1}.

In this study we only consider cloud-free scenes, based on EUMETSAT L2 cloud products. For details about the EUMETSAT IASI cloud-screening strategy, refer to August et al. (2012) and the "Products User Guide" (EUMETSAT, 2017). Here we present MUSICA IASI retrieval data that are filtered with respect to measurement noise and retrieval quality (residual-to-signal ratio in the fitted spectral window must be smaller than 0.004), cold scenes (surface temperature must be higher than 275 K) and the sensitivity to CH_4 and N_2O (see details in Sect. 3.2). All MUSICA IASI retrieval data (including those corresponding to high residual-to-signal ratio, low surface temperature, or low sensitivity to CH_4 and N_2O) are available at http://www.imk-asf.kit.edu/english/2746.php (last access: 11 July 2018) or by request to the authors.

Table 1. History of EUMETSAT level 2 PPF software modification and EUMETSAT level 2 data usage that can potentially affect the MUSICA IASI products.

Start date	PPF software	Relevance for MUSICA IASI product
27/11/2007	v4.0	Start of EUMETSAT operational level 2 data dissemination.
14/09/2010	v5.0.6	Improvement of the EUMETSAT level 2 middle–upper-tropospheric temperatures (August et al., 2012), which are subsequently used as a priori data by the MUSICA processor.
20/10/2011	v5.2.1	Change in the radiative transfer model used for EUMETSAT level 2 cloud-free optimal estimation retrievals of atmospheric temperatures (EUMETSAT, 2017), which are subsequently used as a priori data by the MUSICA processor.
30/09/2014	v6.0.5	Start using of EUMETSAT level 2 land surface emissivities (instead of IREMIS, Seemann et al., 2008) for MUSICA processing over land. Change in pressure gridding used by the EUMETSAT level 2 cloud-free optimal estimation retrievals of atmospheric temperatures (EUMETSAT, 2017), which are subsequently used as a priori data by the MUSICA processor.

2.4 A posteriori-calculated difference between CH_4 and N_2O

2.4.1 Motivation

When aiming for precise CH_4 observations from space-based platforms, the combination of the retrieved CH_4 observations a posteriori with the co-retrieved N_2O estimates has been proposed (Razavi et al., 2009; Worden et al., 2012; Alvarado et al., 2015; Siddans et al., 2017). Because the N_2O concentrations show a rather low short-term variability and their long-term increase is rather smooth (Stocker et al., 2013), significant variations in the N_2O retrieval product are likely due to errors. Assuming that errors in the simultaneously retrieved CH_4 and N_2O products are correlated, we can generate a combined product with reduced errors. The combination also reduces the signals in CH_4 and N_2O that have the same origin, like the shift in the tropopause altitude that similarly affects CH_4 and N_2O concentrations in the UTLS (upper troposphere–lower stratosphere) region.

We can work with the retrieved N_2O and CH_4 state vectors in the logarithmic scale and write the following in analogy to Eq. (9):

$$\begin{aligned}\hat{\boldsymbol{x}}_{\mathrm{N_2O}} &= \mathbf{A}_{\mathrm{N_2O}}(\boldsymbol{x}_{\mathrm{N_2O}} - \boldsymbol{x}_{\mathrm{a,N_2O}}) + \boldsymbol{x}_{\mathrm{a,N_2O}} + \boldsymbol{\Delta}\hat{\boldsymbol{x}}_{\mathrm{N_2O}},\\ \hat{\boldsymbol{x}}_{\mathrm{CH_4}} &= \mathbf{A}_{\mathrm{CH_4}}(\boldsymbol{x}_{\mathrm{CH_4}} - \boldsymbol{x}_{\mathrm{a,CH_4}}) + \boldsymbol{x}_{\mathrm{a,CH_4}} + \boldsymbol{\Delta}\hat{\boldsymbol{x}}_{\mathrm{CH_4}}. \quad (10)\end{aligned}$$

If we now calculate the difference between the state vectors (difference in the logarithmic scale), we get

$$\begin{aligned}\hat{\boldsymbol{x}}_{\mathrm{CH_4}} - \hat{\boldsymbol{x}}_{\mathrm{N_2O}} = \boldsymbol{x}_{\mathrm{a,CH_4}} - \boldsymbol{x}_{\mathrm{a,N_2O}} + \mathbf{A}_{\mathrm{CH_4}}(\boldsymbol{x}_{\mathrm{CH_4}} - \boldsymbol{x}_{\mathrm{a,CH_4}})\\ - \mathbf{A}_{\mathrm{N_2O}}(\boldsymbol{x}_{\mathrm{N_2O}} - \boldsymbol{x}_{\mathrm{a,N_2O}}) + \boldsymbol{\Delta}\hat{\boldsymbol{x}}_{\mathrm{CH_4}} - \boldsymbol{\Delta}\hat{\boldsymbol{x}}_{\mathrm{N_2O}}. \quad (11)\end{aligned}$$

The idea is that (i) the difference of the errors $\boldsymbol{\Delta}\hat{\boldsymbol{x}}_{\mathrm{CH_4}} - \boldsymbol{\Delta}\hat{\boldsymbol{x}}_{\mathrm{N_2O}}$ is much smaller than the errors in the individual products $\boldsymbol{\Delta}\hat{\boldsymbol{x}}_{\mathrm{CH_4}}$ or $\boldsymbol{\Delta}\hat{\boldsymbol{x}}_{\mathrm{N_2O}}$, and that (ii) as N_2O shares the dynamical variations of CH_4 in the tropopause region, the combined product has a weaker dependency on the tropopause altitude and potentially an improved representativeness of source and sink signals.

2.4.2 Theoretical treatment

By a simple matrix multiplication we can make a transformation from the $\{\ln[\mathrm{N_2O}], \ln[\mathrm{CH_4}]\}$ space into the $\left\{\ln[\mathrm{CH_4}] - \ln[\mathrm{N_2O}], \frac{\ln[\mathrm{CH_4}]+\ln[\mathrm{N_2O}]}{2}\right\}$ space. This transformation between basis systems has been discussed in detail for water vapour isotopologue states in Schneider et al. (2012) and the same approach can be applied for the N_2O and CH_4 states. The transformation matrix $\mathbf{P}$ is

$$\mathbf{P} = \begin{pmatrix} -\mathbb{I} & \mathbb{I} \\ \frac{1}{2}\mathbb{I} & \frac{1}{2}\mathbb{I} \end{pmatrix}. \quad (12)$$

Here, the four matrix blocks have the dimension (nol × nol), and $\mathbb{I}$ stands for an identity matrix.

The averaging kernel matrix of the transformed states can be calculated as

$$\mathbf{A}^{\mathbf{P}} = \mathbf{P}\mathbf{A}\mathbf{P}^{-1} = \begin{pmatrix} \mathbf{A}^{\mathbf{P}}_{\mathbf{11}} & \mathbf{A}^{\mathbf{P}}_{\mathbf{12}} \\ \mathbf{A}^{\mathbf{P}}_{\mathbf{21}} & \mathbf{A}^{\mathbf{P}}_{\mathbf{22}} \end{pmatrix}. \quad (13)$$

There are four matrix blocks with the dimension (nol × nol) and the kernels for the combined product $\hat{\boldsymbol{x}}_{\mathrm{CH_4}} - \hat{\boldsymbol{x}}_{\mathrm{N_2O}}$ are collected in the matrix block $\mathbf{A}^{\mathbf{P}}_{\mathbf{11}}$.

The errors for the transformed states can be calculated in analogy to Eq. (7):

$$\boldsymbol{\Delta}\hat{\boldsymbol{x}}^{\mathbf{P}} = -\mathbf{P}\mathbf{G}\mathbf{K}_{\mathbf{b}}\boldsymbol{\Delta}\boldsymbol{b} = \begin{pmatrix} \boldsymbol{\Delta}\hat{\boldsymbol{x}}^{\mathbf{P}}_{\mathbf{1}} \\ \boldsymbol{\Delta}\hat{\boldsymbol{x}}^{\mathbf{P}}_{\mathbf{2}} \end{pmatrix}. \quad (14)$$

The vector block $\boldsymbol{\Delta}\hat{\boldsymbol{x}}^{\mathbf{P}}_{\mathbf{1}}$ collects the error pattern of the a posteriori-calculated product $\hat{\boldsymbol{x}}_{\mathrm{CH_4}} - \hat{\boldsymbol{x}}_{\mathrm{N_2O}}$.

Similarly the error covariance matrix for the transformed states are calculated in analogy to Eq. (8):

$$\mathbf{S}^{\mathbf{P}}_{\hat{\mathbf{x}},\mathbf{b}} = \mathbf{P}\mathbf{G}\mathbf{K}_{\mathbf{b}}\mathbf{S}_{\mathbf{b}}{\mathbf{K}_{\mathbf{b}}}^{T}\mathbf{G}^{T}\mathbf{P}^{T} = \begin{pmatrix} \mathbf{S}^{\mathbf{P}}_{\hat{\mathbf{x}},\mathbf{b},\mathbf{11}} & \mathbf{S}^{\mathbf{P}}_{\hat{\mathbf{x}},\mathbf{b},\mathbf{12}} \\ \mathbf{S}^{\mathbf{P}}_{\hat{\mathbf{x}},\mathbf{b},\mathbf{21}} & \mathbf{S}^{\mathbf{P}}_{\hat{\mathbf{x}},\mathbf{b},\mathbf{22}} \end{pmatrix}. \quad (15)$$

The error covariances for the a posteriori-calculated product $\hat{\boldsymbol{x}}_{CH_4} - \hat{\boldsymbol{x}}_{N_2O}$ are collected in the matrix block $\mathbf{S}^{\mathbf{P}}_{\hat{\mathbf{x}},\mathbf{b},\mathbf{11}}$. The error covariance matrix for measurement noise is calculated by $\mathbf{S}^{\mathbf{P}}_{\hat{\mathbf{x}},\text{noise}} = \mathbf{PGS}_{\mathbf{y},\text{noise}}\mathbf{G}^T\mathbf{P}^T$. It also consists of four blocks and $\mathbf{S}^{\mathbf{P}}_{\hat{\mathbf{x}},\text{noise},\mathbf{11}}$ represents the errors covariance for the a posteriori-calculated product $\hat{\boldsymbol{x}}_{CH_4} - \hat{\boldsymbol{x}}_{N_2O}$.

The here-presented formalism enables us to analytically describe the characteristics and errors of the a posteriori-calculated product in analogy to the description of the individual CH_4 and N_2O retrieval products.

2.4.3 CH_4 correction on all scales

Because N_2O is relatively stable, the horizontal and vertical N_2O distribution might be captured reasonably well by atmospheric models. The a posteriori-calculated difference according to Eq. (11) can then be used together with N_2O model data for calculating a corrected CH_4 product by

$$\hat{\boldsymbol{x}}^{\mathbf{c}}{}_{CH_4} = (\hat{\boldsymbol{x}}_{CH_4} - \hat{\boldsymbol{x}}_{N_2O}) + \mathbf{A}_{N_2O}(\boldsymbol{m}_{N_2O} - \boldsymbol{x}_{a,N_2O}) + \boldsymbol{x}_{a,N_2O}. \quad (16)$$

Here $\boldsymbol{m}_{N_2O}$ is the N_2O distribution as obtained from accurate model simulations. In the corrected state vector $\hat{\boldsymbol{x}}^{\mathbf{c}}{}_{CH_4}$, a large part of the correlated N_2O and CH_4 retrieval errors will be removed.

The error of $\hat{\boldsymbol{x}}^{\mathbf{c}}{}_{CH_4}$ has two contributions. A first error contribution is the uncertainty involved in the interpretation of the IASI measurement and a second is the uncertainty involved in the N_2O model simulations. These second contribution is completely independent on the IASI measurement. Because we are not interested in the errors that are independent on the IASI measurements, we assume $\boldsymbol{m}_{N_2O} = \boldsymbol{x}_{a,N_2O}$ (i.e. a uniform N_2O distribution without horizontal, vertical and temporal variations) and get the following from Eq. (16):

$$\hat{\boldsymbol{x}}^{*}{}_{CH_4} = (\hat{\boldsymbol{x}}_{CH_4} - \hat{\boldsymbol{x}}_{N_2O}) + \boldsymbol{x}_{a,N_2O}. \quad (17)$$

In this paper we use the label CH_4^* for the product that has undergone the a posteriori processing according to Eq. (17) and has subsequently been transferred to the linear scale. A brief description of CH_4^* in the context of the other CH_4 products used in this paper is given in Table 2.

The variation in the CH_4^* product is driven by IASI measurements and not affected by external data (e.g. model simulations), and the evaluation of CH_4^* will reveal the errors in the corrected data that are linked to the IASI measurements. For analytically characterizing the CH_4^* product we can use $\mathbf{A}^{\mathbf{P}}_{\mathbf{11}}$, $\mathbf{\Delta}\hat{\boldsymbol{x}}^{\mathbf{P}}_{\mathbf{1}}$, $\mathbf{S}^{\mathbf{P}}_{\hat{\mathbf{x}},\mathbf{b},\mathbf{11}}$ and $\mathbf{S}^{\mathbf{P}}_{\hat{\mathbf{x}},\text{noise},\mathbf{11}}$ (according to Sect. 2.4.2). A validation by comparison to reference measurements can only by made if we have reference measurements of CH_4 and N_2O, because the CH_4^* product contains combined information on CH_4 and N_2O variations.

The here-presented correction addresses all temporal and spatial scales. All the variations in the original CH_4 retrieval product that are correlated to the variations in the N_2O retrieval product are removed. Please be aware that for the full reconstruction of CH_4 from CH_4^* accurate simulations of a full N_2O model are needed (see Eq. 16 and Appendix A). A correction of CH_4 according to Eq. (17) has already been discussed by Alvarado et al. (2015) for TES, but using variable N_2O a priori data. Our method works with a single N_2O a priori profile. Performing the correction after the retrieval process (a posteriori processing) makes the method rather flexible and allows applying different N_2O models for the full reconstruction of CH_4. This flexibility is an important difference compared to Siddans et al. (2017), where the correction supported by N_2O simulations is firmly implemented within the retrieval scheme.

3 Representativeness and error assessment

3.1 Averaging kernels

The averaging kernel matrix ($\mathbf{A}$) is an important output of the retrieval process. Its rows describe the altitude regions that are mainly represented in the retrieved target gas VMR profile (see Eq. 6).

Figure 2a shows the rows of $\mathbf{A}$ for the state {ln[N_2O], ln[CH_4]} for an observation over land during mid-latitude summer. The grey colour shows all rows and the red and blue colours represent the rows that represent the 3.6 and 10.9 km altitude, respectively. The panels in the diagonal of Fig. 2a represent the ln[N_2O] and ln[CH_4] kernels and the outer diagonal panels the cross kernels (the elements of these cross kernels have very low values). For the ln[N_2O] kernel we get a degree of freedom for signal (DOFS) value of 1.39. The DOFS value is calculated as the trace of the averaging kernel matrix and is a measure of sensitivity and the vertical resolution of the remote sensing data. The higher the DOFS value the more information is extracted from the measured radiances. In addition, we calculate the sum along the averaging kernel rows representing the altitudes of 3.6 and 10.9 km (in the following we call them Σ values). The closer the Σ value to unity the more sensitive are the retrieved values to real atmospheric variations. For ln[N_2O] we get a Σ values of 0.65 and 1.12 for 3.6 and 10.9 km altitude, respectively. The MUSICA IASI N_2O product has a good sensitivity in the upper troposphere–lower stratosphere (here represented by the 10.9 km altitude) and is only weakly sensitive to the free troposphere (here represented by 3.6 km altitude). For the ln[CH_4] kernels the DOFS value is 1.68, i.e. higher than for ln[N_2O]. The Σ values of 0.77 and 1.04 for 3.6 and 10.9 km altitude, respectively, reveal that in the UTLS region the CH_4 retrieval product has a similar sensitivity than the N_2O product; however, in the free troposphere the retrieval is more sensitive to CH_4 than to N_2O.

Figure 2b depicts the rows of $\mathbf{A}^{\mathbf{P}}$, i.e. the averaging kernel for the state $\left\{\ln[CH_4] - \ln[N_2O], \frac{\ln[CH_4]+\ln[N_2O]}{2}\right\}$, ac-

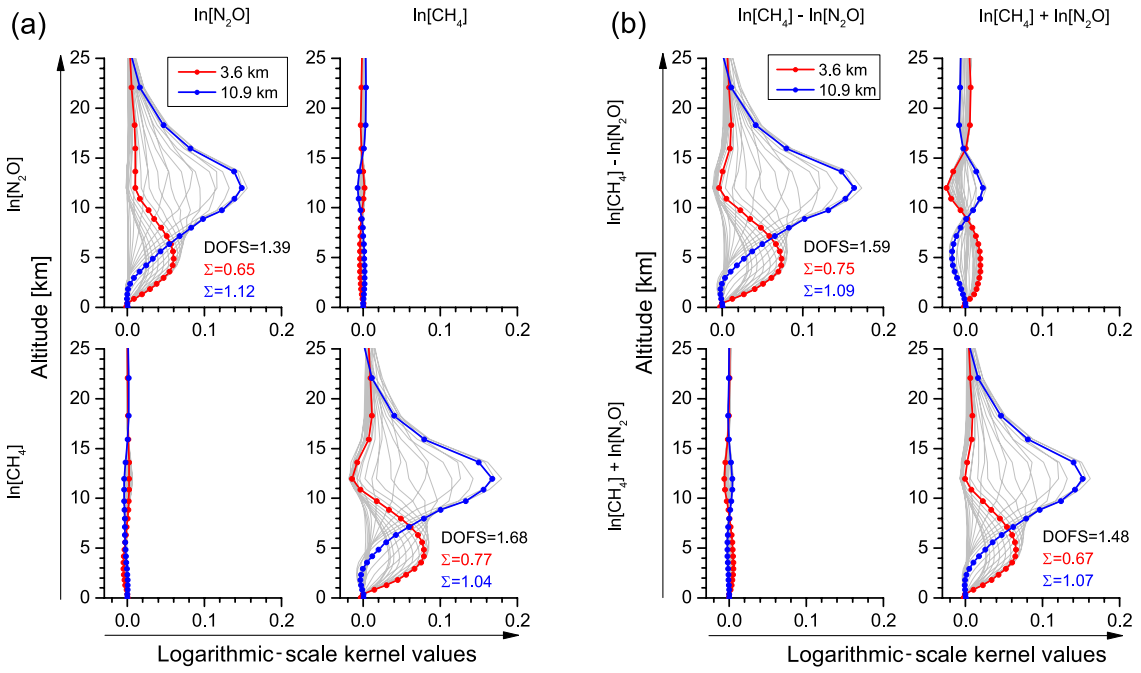

Figure 2. Example of an averaging kernel for an observation over the mid-latitude site of Lindenberg (52° N) on 30 August 2008 (satellite nadir angle: 43.7°; surface skin temperature: 292.3 K; precipitable water vapour: 31.8 mm): **(a)** for the state vector {ln[N_2O], ln[CH_4]} and **(b)** for the state vector $\left\{\ln[CH_4] - \ln[N_2O], \frac{\ln[CH_4]+\ln[N_2O]}{2}\right\}$.

Table 2. Overview on the different N_2O and CH_4 remote sensing products discussed in this work.

Name	Label	Proxy used for characterization	Description
N_2O retrieval product	N_2O	ln[N_2O]	The MUSICA IASI optimal estimation retrieval output for N_2O.
CH_4 retrieval product	CH_4	ln[CH_4]	The MUSICA IASI optimal estimation retrieval output for CH_4. Please note that the MUSICA IASI processor simultaneously retrieves N_2O and CH_4 in a single retrieval step.
Difference between N_2O and CH_4	–	$\ln[CH_4] - \ln[N_2O]$	A posteriori difference (on logarithmic scale) between the CH_4 and N_2O retrieval products according to Eq. (11).
Product corrected on all scales	CH_4^*	$\ln[CH_4] - \ln[N_2O]$	A posteriori correction consisting in removing all the CH_4 variations that are correlated to N_2O variations (see Sect. 2.4.3). For a full reconstruction of CH_4 from CH_4^*, accurate N_2O full model simulations are required.
Product corrected on scales where errors dominate	CH_4'	$\ln[CH_4] - \ln[N_2O]$	A posteriori correction consisting in removing the CH_4 variations that are correlated to N_2O variations taking place on the scales where the variations are dominated by errors (see Sect. 7). For a full reconstruction of CH_4 from CH_4', an accurate global N_2O model climatology is required.

cording to Eq. (13). Here we are mainly interested in the $\ln[CH_4] - \ln[N_2O]$ product (see discussion in Sect. 2.4). The DOFS value and the Σ values for 3.6 and 10.9 km indicate reasonable sensitivity in the free troposphere and the UTLS region.

The example of Fig. 2 indicates that the MUSICA IASI retrieval product can capture atmospheric variations of CH_4 and N_2O between about 2 km above ground and about 16 km altitude with a vertical resolution of about 5–8 km (full width at half maximum, FWHM, of the averaging kernels). The kernels as shown in Fig. 2 suggest that the MUSICA IASI product can make invaluable contributions for investigating atmospheric variations having a vertical dimension of at least 5 km. The limited vertical resolution and sensitivity is an in-

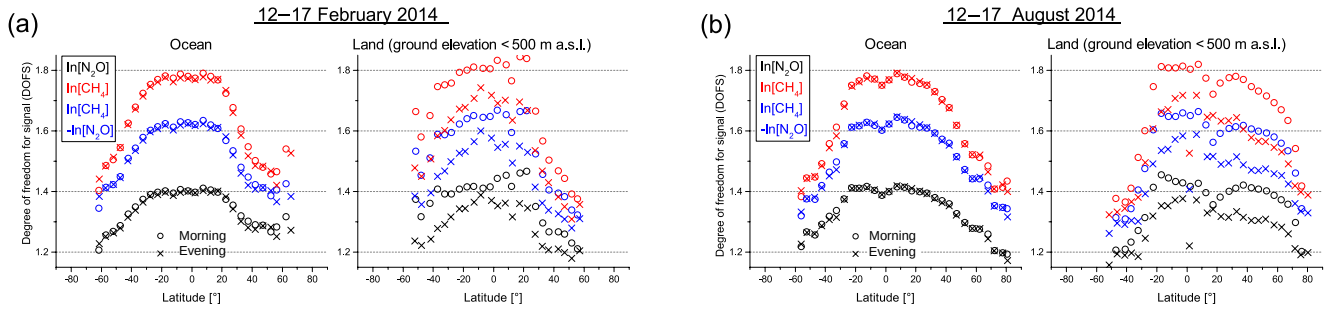

Figure 3. Latitudinal cut of the DOFS values of the $\ln[N_2O]$ (black dots), $\ln[CH_4]$ (red dots) and $\ln[CH_4] - \ln[N_2O]$ (blue dots) products for the IASI morning and evening overpasses ($\approx$ 09:30 and 21:30 Local Solar Time, respectively): **(a)** for mid-February 2014 and **(b)** for mid-August 2014. The latitudinal cuts are shown separately for observations over ocean and land (only if ground altitude < 500 m a.s.l.).

trinsic characteristic of the remote sensing data product and, consequently, the product is not suited for addressing scientific questions that need vertically finer resolved data. For such purposes vertically highly resolved in situ profile data would be the best choice.

3.2 Latitudinal and vertical dependency of the representativeness

Figure 2 shows the kernels for an example observation. However, the altitude ranges that are represented by the remote sensing products vary with season and latitude. The variation of the representativeness is revealed by Fig. 3. It shows a high variability of the DOFS values. The values depend on latitude, season, the observation scenario (land or ocean) and the time of satellite overpass (morning or evening), attributed mainly to the variation of the thermal contrast between surface and the lowermost atmosphere layers. For $\ln[N_2O]$ the DOFS values vary between 1.2 and 1.4 (black dots) and for $\ln[CH_4]$ between 1.4 and 1.8 (red dots), respectively. For the combined product $\ln[CH_4] - \ln[N_2O]$ the DOFS values vary between 1.3 and 1.6. Note that only for Fig. 3 the IASI data have been split into morning and evening observations.

We suggest using a simple metric according to Rodgers (2000) to identify the altitude regions where an individual data product is representative of atmospheric variations having a vertical dimension of at least 5 km. We analyse the uncertainty (due to limited sensitivity and vertical resolution) for detecting a Gaussian function like vertical structure with $2\sigma = 5$ km. For this purpose we set up an atmospheric covariance matrix $\mathbf{C}$, with unity on the diagonal and the outer diagonal entries calculated assuming a correlation length of $1\sigma = 2.5$ km, and calculate

$$\mathbf{C}_{\text{sen}} = (\mathbf{A} - \mathbb{I})\mathbf{C}(\mathbf{A} - \mathbb{I})^T. \quad (18)$$

$\mathbf{A}$ is the averaging kernel and $\mathbb{I}$ the identity matrix. We investigate the diagonal elements of $\mathbf{C}_{\text{sen}}$. Because the diagonal of $\mathbf{C}$ is unity, the diagonal elements of $\mathbf{C}_{\text{sen}}$ (c_{sen}) give the portion of the actual variance that is not detectable by the MUSICA IASI data product. For documenting the sensitivity of $\ln[CH_4] - \ln[N_2O]$ we use $\mathbf{A}^{\mathbf{P}}_{\mathbf{11}}$ from Eq. (13).

Figure 4 depicts latitudinal cuts of the diagonal elements c_{sen} for altitudes between ground and 20 km. This figure is in good agreement with Figs. 2 and 3. We find that the sensitivity is generally limited to the altitudes between 2 and 16 km. The $\ln[CH_4]$ product has the best sensitivity (lowest c_{sen} values). At low latitudes the altitude regions with good representativeness have the largest vertical extension. Concerning middle and high latitudes and the product $\ln[CH_4]$, $c_{\text{sen}} < 0.5$ is limited to altitudes between 2 and 12 km, whereas at latitudes between 30° S and 30° N such low c_{sen} values are generally found between 2 and 15 km. Since at these low latitudes the DOFS values for the $\ln[CH_4]$ product are close to 2.0, it can be concluded that between 30° S and 30° N the MUSICA IASI processor can detect CH_4 profiles, i.e. CH_4 amounts in the free troposphere around 4 km independently from CH_4 amounts in the UTLS region around 12 km. For the products $\ln[N_2O]$ and $\ln[CH_4] - \ln[N_2O]$ we observe a similar dependency, but the lower c_{sen} and DOFS values indicate a weaker profiling capability.

In the following we will work with retrieval products for a certain altitude only if the respective diagonal element (c_{sen}) is smaller than 0.5, i.e. if the vertical resolution and the sensitivity of the remote sensing data are sufficient to detect at least 50 % of 5 km broad variances that take place around these altitudes in the actual atmosphere.

3.3 Error assessment

The theoretical error estimations consist in calculating the error profiles $\mathbf{\Delta}\hat{\boldsymbol{x}}$ and the error covariance matrices $\mathbf{S}_{\hat{\mathbf{x}},\mathbf{b}}$ and $\mathbf{S}_{\hat{\mathbf{x}},\text{noise}}$. For the $\ln[N_2O]$ and $\ln[CH_4]$ product the calculations are done according to Sect. 2.2. For $\ln[CH_4] - \ln[N_2O]$ we calculate $\mathbf{\Delta}\hat{\boldsymbol{x}}^{\mathbf{P}}_{\mathbf{1}}$, $\mathbf{S}^{\mathbf{P}}_{\hat{\mathbf{x}},\mathbf{b},\mathbf{11}}$ and $\mathbf{S}^{\mathbf{P}}_{\hat{\mathbf{x}},\text{noise},\mathbf{11}}$ according to Sect. 2.4.2, which ensures that the error correlations between N_2O and CH_4 are fully considered.

A description of the assumed uncertainty sources (matrix $\mathbf{S}_{\mathbf{b}}$ used in Eqs. 8 and 15) is given in Table 3. For surface emissivity we assume an uncertainty of 1 % and a corre-

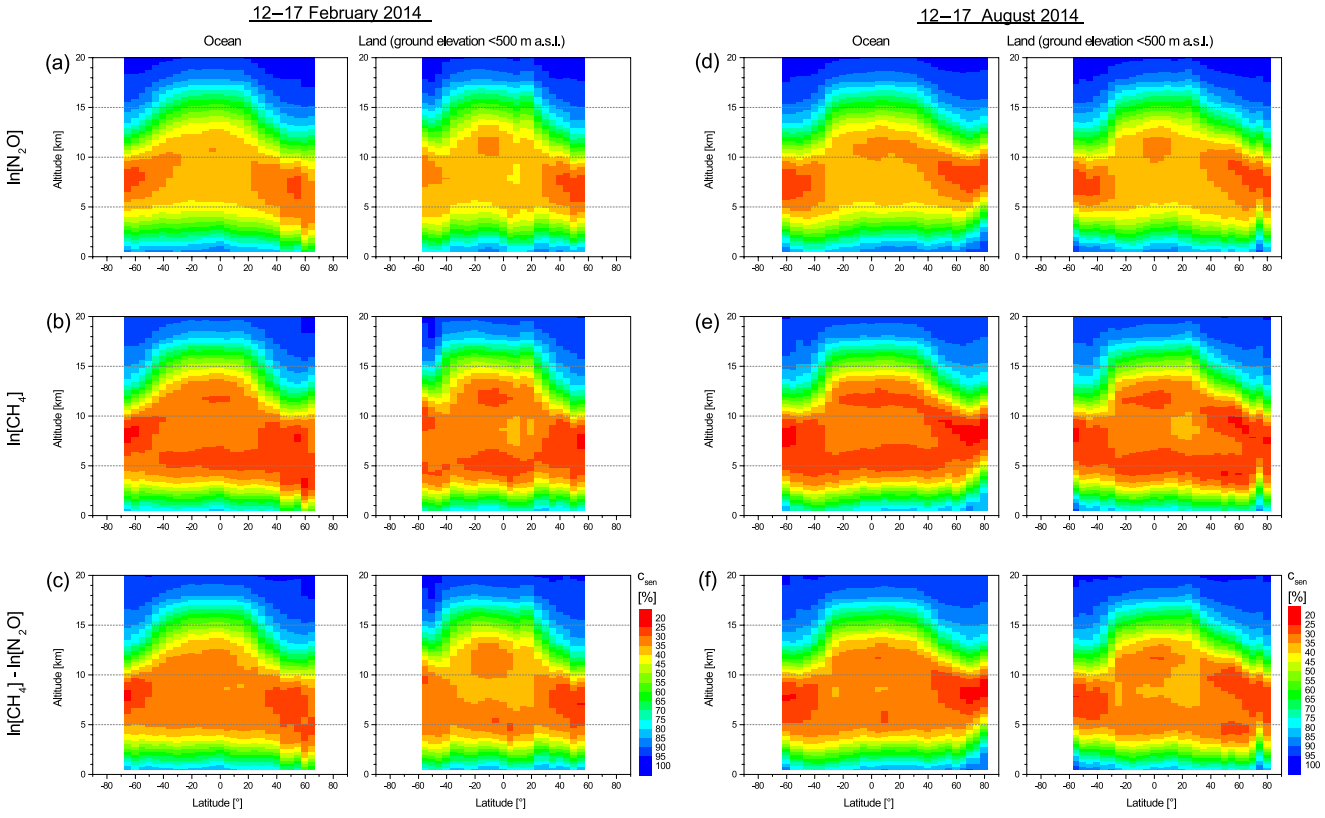

Figure 4. Latitudinal cuts of the vertical dependency of the sensitivity (defined as c_{sen} values according Eq. 18): **(a–c)** for mid-February and the products $\ln[N_2O]$, $\ln[CH_4]$ and $\ln[CH_4] - \ln[N_2O]$, respectively; and **(d–f)** for the same products, but for mid-August. The latitudinal cuts are shown separately for observations over ocean and land (only if ground altitude < 500 m a.s.l.).

Table 3. List of uncertainty assumptions used for the error estimation.

Uncertainty source	Uncertainty value
Measurement noise	according to Pequignot et al. (2008)
Surface emissivity	1 %, with a spectral frequency correlation length of 100 cm^{-1}
Temperature in lower troposphere (0–2 km)	2 K
Temperature in middle troposphere (2–5 km)	1 K
Temperature in upper troposphere (5–10 km)	1 K
Temperature in upper atmosphere (above 10 km)	1 K
$\{H_2O,\delta D\}$ variations	{100 %,100‰}, with 2.5 km vertical correlation length
Water vapour continuum	10 % underestimation of model MT_CKD v2.5.2
Line intensity N_2O	+2 %
Pressure-broadening N_2O	+2 %
Line intensity CH_4	−2 %
Pressure-broadening CH_4	−2 %
Opaque cumulus cloud	10 % fractional cover with cloud top at 1.3, 3.0 and 4.9 km
Cirrus cloud	particle properties according to OPAC "Cirrus 3"; 1 km thickness; 50 % fractional cover with cloud top at 6, 8, 11 and 14 km
Mineral dust cloud	particle properties according to OPAC "Desert"; homogeneous coverage for layers: ground–2, 2–4 and 4–6 km

lation of the uncertainty between different frequencies decaying Gaussian-like with a σ-value (correlation length) of 100 cm^{-1}. Regarding atmospheric temperatures we assume an uncertainty of 2 K between ground and 2 km a.s.l. and 1 K for higher altitudes, whereby we work with independent uncertainties in four different layers: ground–2, 2–5, 5–10 km

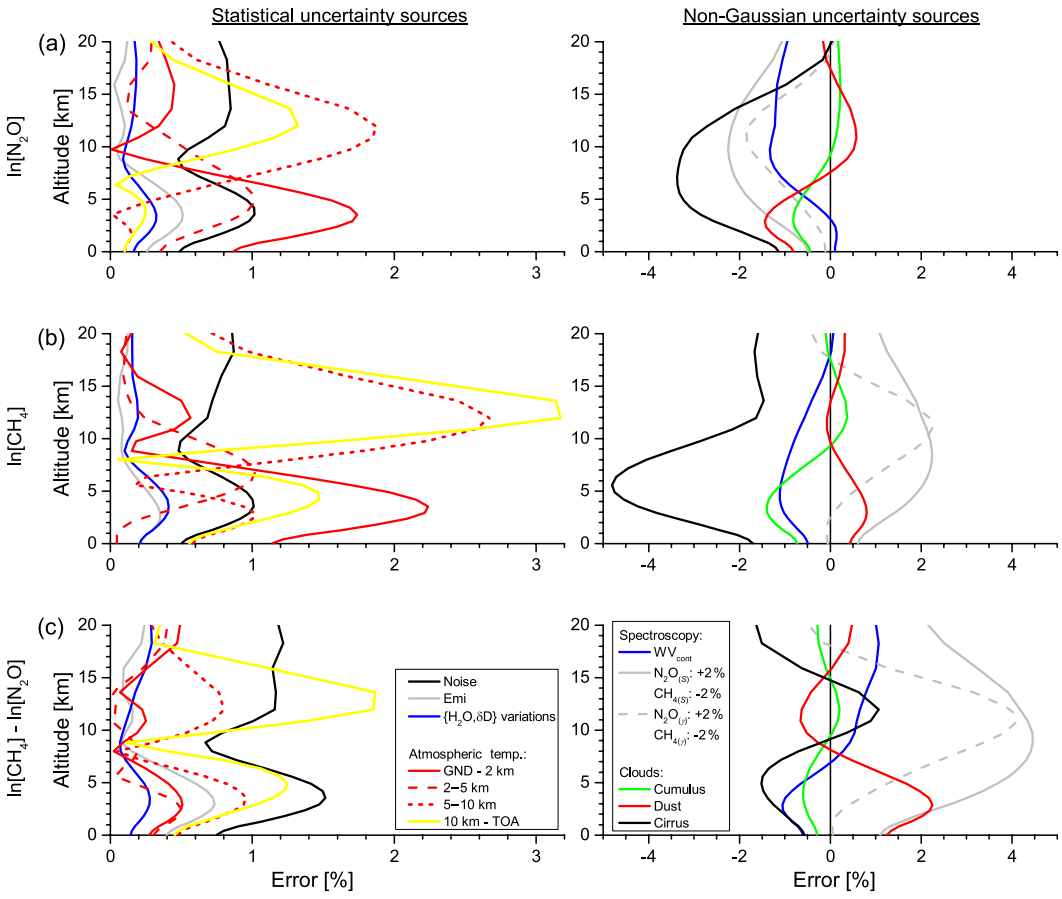

Figure 5. Example of estimated errors for an observation over the mid-latitude site of Lindenberg (52° N) on 30 August 2008 (same as Fig. 2): **(a)** for the state vector ln[N_2O], **(b)** for the state vector ln[CH_4] and **(c)** for the state vector ln[CH_4] − ln[N_2O]. The left panels show errors due to statistical uncertainty sources and the right panels errors due to uncertainty sources that are not Gaussian (unrecognized clouds or systematic uncertainty sources like spectroscopic parameters/parameterizations).

and above 10 km. This atmospheric temperature uncertainties are in agreement with August et al. (2012). Different water vapour isotopologues dominate the spectral signatures in the fitted spectral region and we have to consider cross-dependency on the water vapour isotopologue variations. We assume a variation of 100 % of humidity and of 100 ‰ of δD (the strongest varying water vapour isotopologue ratio) and a vertical correlation length of these variations of 2.5 km. As measurement noise we use the noise covariances of Pequignot et al. (2008).

All the aforementioned uncertainty sources are assumed to have a Gaussian distribution. We refer to them as statistical uncertainty sources and they can be reduced by calculating the mean of many data points. In the following we discuss uncertainty sources that are systematic (like spectroscopic parameters/parameterizations) or are far away from being Gaussian distributed (like clouds). We hypothetically assume that calculations based on the model MT_CKD v2.5.2 (Mlawer et al., 2012; Delamere et al., 2010; Payne et al., 2011) only partly capture the full water vapour continuum effect (we consider an underestimation of 10 % of the effect). For the spectroscopic parameters (line intensity and pressure-broadening parameter) of N_2O and CH_4, we assume an uncertainty of 2 %. These error values are in concordance with those reported in the HITRAN database (Rothman et al., 2009): for N_2O a positive uncertainty and for CH_4 a negative uncertainty (actually the uncertainties are uncorrelated; i.e. they can all be positive, all negative or all different). Uncertainties in the spectroscopic parameters of the water vapour isotopologues of about 1 % have no significant effect on the retrieval of N_2O and CH_4. Finally, we consider the effect of unrecognized clouds on the retrieval products. We assume 10 % coverage with opaque cumulus clouds, 50 % coverage with cirrus clouds and mineral dust at different altitudes. For more details on the cloud assumptions please refer to Borger et al. (2017).

The left part of Fig. 5 shows the square root values of the diagonal elements of $\mathbf{S}_{\hat{\mathbf{x}},\mathbf{b}}$ and $\mathbf{S}_{\hat{\mathbf{x}},\mathrm{noise}}$ (according to Sect. 2.2) and $\mathbf{S}^{\mathbf{P}}_{\hat{\mathbf{x}},\mathbf{b},\mathbf{11}}$ and $\mathbf{S}^{\mathbf{P}}_{\hat{\mathbf{x}},\mathrm{noise},\mathbf{11}}$ (according to Sect. 2.4.2) for the errors caused by statistical uncertainty sources. For

the ln[N_2O] and in particular for the ln[CH_4] product atmospheric temperatures are the dominating uncertainty source (see yellow and red lines Fig. 5a and b). For the ln[CH_4] − ln[N_2O] product (Fig. 5c) the error due to atmospheric temperature uncertainties is significantly smaller than in the ln[CH_4] product, because the atmospheric temperature errors in ln[N_2O] and ln[CH_4] are significantly correlated. Measurement noise errors in ln[N_2O] and ln[CH_4] are almost completely uncorrelated and thus particularly large in the ln[CH_4] − ln[N_2O] product. Errors due to emissivity or interferences from varying {H_2O,δD} distributions are of minor importance. However, please note that the effect of varying {H_2O,δD} distributions might become significantly large when using a different retrieval setup (recall that the MUSICA processor has been especially designed for correctly capturing the atmospheric {H_2O,δD} variations).

The right part of Fig. 5 depicts the error profiles $\mathbf{\Delta}\hat{\boldsymbol{x}}$ (according to Eq. 7) and $\mathbf{\Delta}\hat{\boldsymbol{x}}_1^P$ (according to Eq. 14) for the errors caused by non-Gaussian uncertainty sources (spectroscopic parameters/parameterizations and unrecognized clouds). An unrecognized cirrus cloud has the most pronounced effect. It causes significant negative errors in the tropospheric ln[N_2O] and ln[CH_4] products. The error is especially large for the ln[CH_4] product (see black line Fig. 5b). Because this error is correlated in ln[N_2O] and ln[CH_4], it is much smaller in the ln[CH_4]−ln[N_2O] product. However, for the ln[CH_4] − ln[N_2O] product the uncertainty in the spectroscopic parameters can cause especially large systematic errors (see grey lines in Fig. 5c).

Similar to the sensitivity the errors depend on latitude and season. This is demonstrated in Fig. 6 showing the latitudinal cuts of the root square sum of the leading statistical errors, which are the errors due to atmospheric temperature uncertainty and measurement noise. The error sum is larger in the ln[CH_4] product than in the ln[N_2O] product (in agreement with Fig. 5). The error sum is in particular small for the ln[CH_4] − ln[N_2O] product (see Fig. 6c and f). This is a theoretical demonstration that the a posteriori correction of CH_4 with co-retrieved N_2O can significantly reduce the uncertainty of the data product.

4 Comparison to in situ profile references

In order to experimentally validate the MUSICA IASI CH_4 and N_2O products we use in situ profile measurements made during the project HIPPO (http://hippo.ucar.edu/, last access: 11 July 2018). HIPPO investigated carbon cycle and greenhouse gases by sampling the atmosphere from approximately 67° S to 80° N mostly over the Pacific Ocean, from the surface up to a maximum altitude of 14 km (∼ 150–300 hPa) and spanning all the seasons between 2009 and 2011 (Wofsy et al., 2011). In total five measurement missions were conducted aboard HIAPER, a modified Gulfstream-V (G-V) aircraft: January 2009 (HIPPO1), November 2009 (HIPPO2), March–April 2010 (HIPPO3), June 2011 (HIPPO4) and August–September 2011 (HIPPO5). During these missions, CH_4 and N_2O in situ measurements were performed using a QCLS (quantum-cascade laser spectrometer) instrument at 1 Hz frequency with a precision of 0.5 and 0.09 ppbv for CH_4 and N_2O, respectively, and an accuracy of 1.0 ppbv for both trace gases (Santoni et al., 2014), i.e. a relative precision and accuracy of about 0.25 and 0.5 ‰ for CH_4 and of about 0.25 and 3 ‰ for N_2O, respectively.

Here we define as an individual HIPPO profile any measurement sequence with continuous measurements between at least 2 and 8 km a.s.l. Consecutive ascents and descents are considered as two individual profiles. In total we identified 441 of such individual profiles with available CH_4 and N_2O data. The grey stars in Fig. 7 indicate the areas of all these profile measurements.

4.1 Collocation

IASI and HIPPO observations are sensing areas of different size with different acquisition times; therefore, appropriate spatial and temporal collocation criteria have to be defined to ensure a feasible inter-comparison. Similarly to previous studies using HIPPO aircraft observations (Wecht et al., 2012; Xiong et al., 2013), each HIPPO vertical profile (covering typically $2° \times 2°$ and 20 min) is characterized by a mean location (latitude and longitude) and a mean time. Firstly, we require that the IASI observations have to be made ±12 h with respect to the HIPPO mean time. Secondly, we only consider the IASI observations that fall within a $2° \times 2°$ latitude × longitude box around the mean location of the HIPPO profile measurement. Typically there are about 5–15 individual cloud-free IASI observations for one individual HIPPO profile measurement that fulfill these coincidence criteria.

We want to compare the IASI products and the HIPPO data for two different altitude regions: the free troposphere (using the 4.2 km retrieval level) and the upper troposphere–lower stratosphere (using the 9.8 km retrieval level). For the comparison to the 4.2 km retrieval we require that HIPPO data are available up to at least 8 km altitude and for the comparison to the 9.8 km retrieval we require data up to at least 12.5 km (which drastically reduces the number of available profiles). Furthermore, we want to compare to MUSICA IASI data that are significantly sensitive to the actual atmospheric state. For this purpose, we only make a comparison to an MUSICA IASI product if the c_{sen} value (according to Eq. 18) at the respective level is smaller than 50 %, i.e. if the MUSICA IASI data are able to detect at least 50 % of the actual atmospheric variances (actual atmospheric variances are assumed to have a Gaussian-like shape with $2\sigma = 5$km).

These requirements leave us with comparison to 165 individual HIPPO profiles for the 4.2 km retrievals. The locations of these profile measurements are indicated by the green crosses in Fig. 7. For the comparisons to 9.8 km retrievals we can work with 23 individual HIPPO profiles, which are

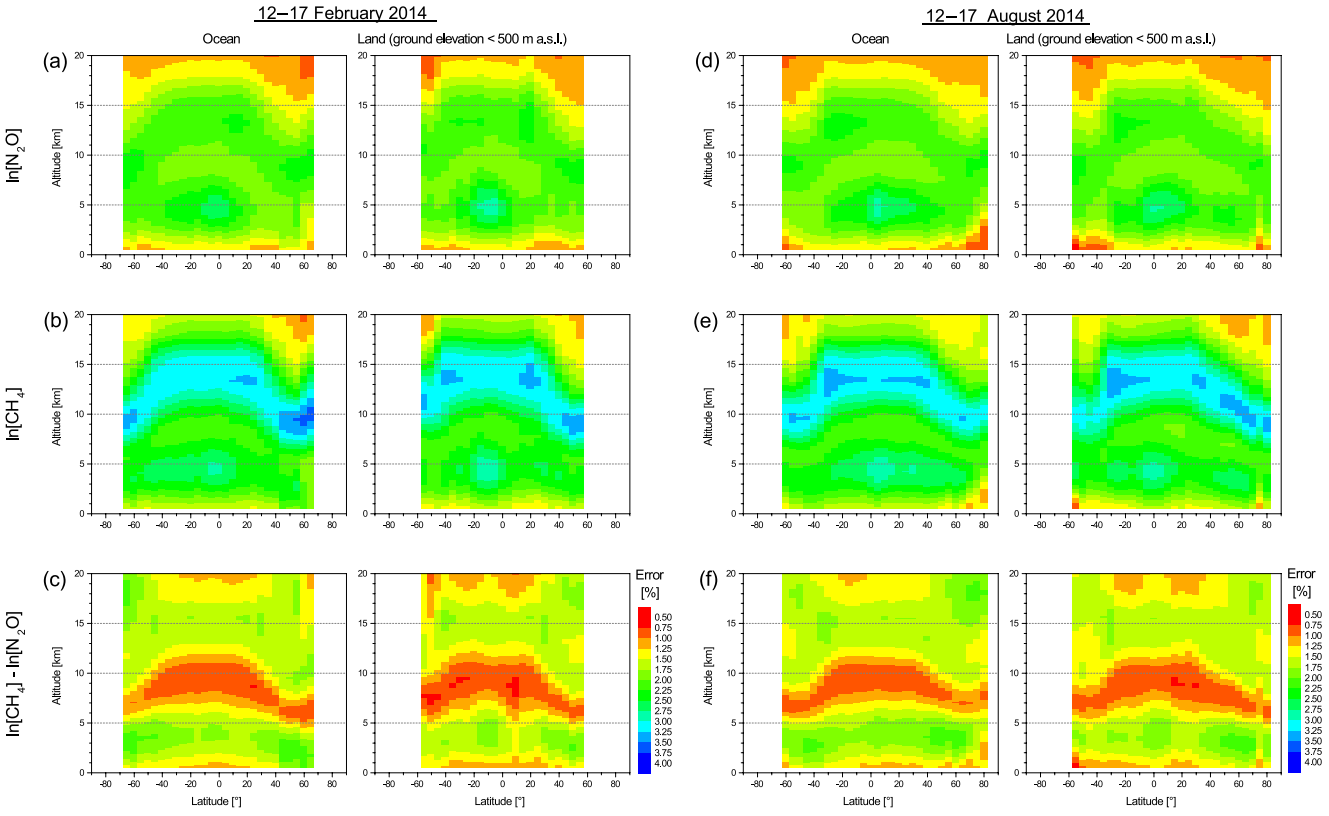

Figure 6. Latitudinal cuts as in Fig. 4, but for the leading statistical errors (atmospheric temperature and measurement noise).

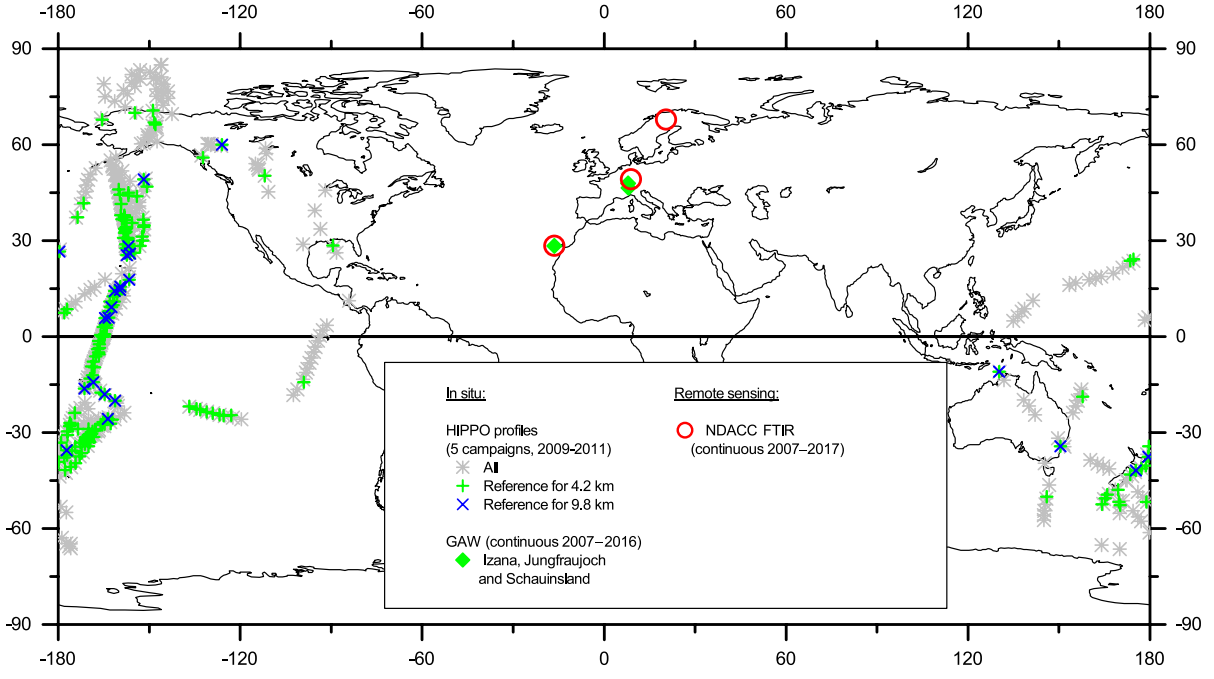

Figure 7. Overview on the locations and time periods with reference measurements used for validating the MUSICA IASI N_2O and CH_4 products.

indicated as blue crosses in Fig. 7. For N_2O the number of valid profile comparisons is smaller than for CH_4, because the sensitivity criterium ($c_{sen} < 0.5$) is more frequently fulfilled for CH_4 than for N_2O.

4.2 HIPPO data treatment

HIPPO provides vertically highly resolved CH_4 and N_2O profile data. From those, the CH_4^* HIPPO profiles are calculated in analogy to Eq. (17):

$$\boldsymbol{h}^*_{CH_4} = (\boldsymbol{h}_{CH_4} - \boldsymbol{h}_{N_2O}) + \boldsymbol{h}_{a,N_2O}, \quad (19)$$

where $\boldsymbol{h}$ is the state vectors containing the HIPPO data and $\boldsymbol{h}_{a,N_2O}$ is the same as $\boldsymbol{x}_{a,N_2O}$, but interpolated to the vertical grid that corresponds to the HIPPO measurements. Note that the calculations are done on a logarithmic scale.

The HIPPO aircraft profiles are limited to a certain ceiling height. Similarly, the profile measurements typically start a few hundred metres above the surface. This is a difference compared to the IASI remote sensing data, which are obtained from radiance measurements that are affected by the whole atmosphere. For all the altitudes where there are no HIPPO data (i.e. first levels above the surface and above the ceiling altitude), we extend the HIPPO data using the a priori data used by the MUSICA IASI processor.

For the comparison we have to consider that the remote sensing products have a much lower sensitivity and vertical resolution than the in situ profiles. For this purpose, the vertically highly resolved HIPPO profiles are degraded by applying the averaging kernels as obtained from the IASI retrievals:

$$\hat{\boldsymbol{h}} = \mathbf{A}(\boldsymbol{h} - \boldsymbol{x}_a) + \boldsymbol{x}_a. \quad (20)$$

These calculations are done for the three products and N_2O, CH_4 and CH_4^* by considering the respective averaging kernels (for CH_4^* this is the kernel $\mathbf{A}^{\mathbf{P}}_{\mathbf{11}}$ from Eq. 13). The usage of a priori data for altitudes without HIPPO data guarantees that these altitudes do not affect $\hat{\boldsymbol{h}}$, which are the data that can be compared to the IASI data.

4.3 Correlation of data

Figure 8 shows the comparison for the two altitude levels (a–c for the 4.2 km and d–f for the 9.8 km altitude level, respectively). Each dot represents one HIPPO profile and the averages of all the MUSICA IASI data that fulfill the coincidence criteria and passed the sensitivity filter. Each panel shows the number of the individual HIPPO profiles used and the R^2 values obtained by a linear least squares regression fit between HIPPO and MUSICA IASI data. The latitude regions that are represented by the different data points are indicated by a colour code (red for high southern latitudes, green for tropical latitudes and blue for high northern latitudes).

Concerning N_2O (Fig. 8a and d) the MUSICA IASI data vary around the unique a priori value used (represented as yellow star). A similar variation is not seen in the HIPPO data at 4.2 km and only weakly seen in the HIPPO data at 9.8 km, leading to very low values of the correlation coefficient R^2. At 9.8 km there are much fewer coincidences, because there are only a few HIPPO profiles that provide data above 12.5 km.

For CH_4 (Fig. 8b and e) the MUSICA IASI and HIPPO data have a similar variation. For 4.2 km we find a correlation coefficient R^2 of 48 %. In both data sets the highest CH_4 concentrations are found at high northern latitudes (blue dots) and the lowest CH_4 concentrations are encountered at middle southern latitudes (red and yellow dots). There is a higher number of coincidences if compared to N_2O, because at 4.2 km more CH_4 than N_2O data pass the sensitivity filter. For 9.8 km we find an R^2 value of 29 % and no clear clustering with respect to the latitude.

Figures 8c and f show the comparison for the CH_4^* product. For both altitudes the R^2 values are higher than for the CH_4 comparisons. At 4.2 km the data point clustering with respect to latitude is further improved (if compared to the clustering of the CH_4 plot). At 9.8 km the MUSICA IASI data indicate the lowest concentrations in the tropics and highest concentration at higher latitudes. This is similarly observed in the HIPPO data; however, the concentration increase at high southern latitudes seems to be weaker in the HIPPO data than in the MUSICA IASI data.

4.4 Bias and scatter

In order to experimentally evaluate the accuracy and precision of the MUSICA IASI data we analyse the difference with respect to the HIPPO data. For each product (N_2O, CH_4 and CH_4^*) we calculate the median of the difference as an estimator of the bias, and the IP68 value of the difference as an estimator of the scatter. The IP68 value is the semi-distance between the percentiles 84.1 and 15.9. We work with median and IP68, because they are less sensitive to the presence of outliers and extreme values than mean and standard deviation, allowing for more robust conclusions on the bias and scatter.

Table 4 resumes the statistical analyses made for the 4.2 and 9.8 km retrieval level. Interestingly, at 4.2 km the percentage scatter values found for N_2O are even slightly smaller than those found for CH_4 (1.7 % for N_2O and 2.0 % for CH_4, respectively), despite the fact that we find a significant correlation for CH_4 but no correlation for N_2O (see Fig. 8). This indicates that the MUSICA IASI N_2O and CH_4 products have a similar precision. However, while this precision is sufficient to detect free-tropospheric latitudinal CH_4 variations, the latitudinal variations of free-tropospheric N_2O are so small that their detection would need a precision of better than a few per mill. At 9.8 km we obtain similar scatter values for N_2O and CH_4 (2.5 and 2.0 %, respectively). At the same time Fig. 8 reveals a weak correlation for N_2O and a stronger correlation for CH_4. In this UTLS altitude re-

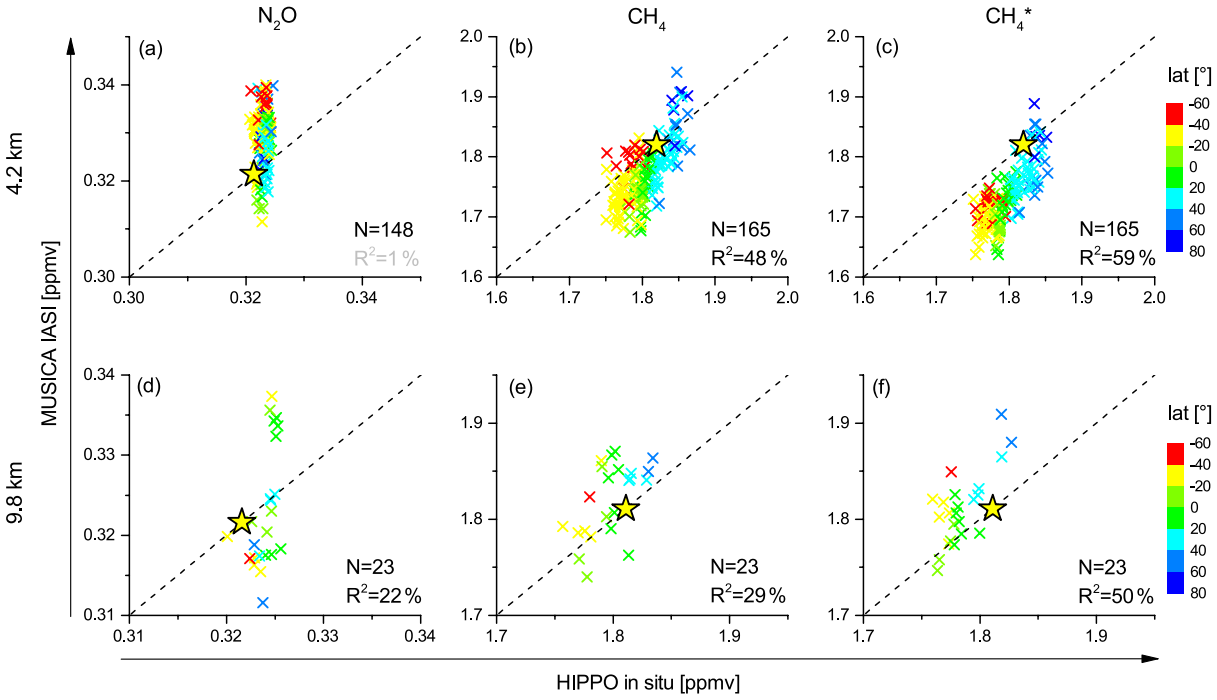

Figure 8. Correlation plots between MUSICA IASI products and HIPPO data: **(a–c)** for the altitude of 4.2 km a.s.l.; **(d–f)** for the altitude of 9.8 km a.s.l.; **(a)** and **(d)** for N_2O; **(b)** and **(e)** for CH_4; and **(c)** and **(f)** for CH_4^*. The colour code indicates the latitudinal region, the yellow star represents the a priori data used for the retrievals and the black dashed line is the one-to-one diagonal. Number of considered HIPPO profiles (N) and R^2 values are given in each panel, black colour indicates significant positive correlations (95 % confidence level) and grey indicates no significance.

Table 4. Statistics on the difference with respect to HIPPO data (MUSICA IASI−HIPPO). The bias is the median and the scatter is the IP68 value (i.e. the semi-distance between the percentiles 84.1 and 15.9). The statistical estimators are shown for comparisons at 4.2 and 9.8 km.

Altitude		N_2O	CH_4	CH_4^*
4.2 km	Profiles	148	165	165
	Bias	+2.0 %	−2.0 %	−3.7 %
	Scatter	1.7 %	2.0 %	1.7 %
9.8 km	Profiles	23	23	23
	Bias	−0.5 %	+1.5 %	+1.5 %
	Scatter	2.5 %	2.0 %	1.6 %

gion the variations in the HIPPO N_2O data are higher than at 4.2 km, but still below the precision level of the MUSICA IASI data and thus hardly observable in the MUSICA IASI data. Concerning upper-tropospheric CH_4 the MUSICA IASI data precision seems to be just a bit better than the typical magnitude of variation; i.e. the real atmospheric variations are partly observable in the MUSICA IASI data. These experimentally found scatter values are in good agreement with the theoretical error estimation of Sect. 3.3.

We found indication of a negative bias of MUSICA IASI CH_4 at 4.2 km, of positive biases of MUSICA IASI N_2O at 4.2 km and of MUSICA IASI CH_4 at 9.8 km. According to our error estimation of Sect. 3.3, this bias can be explained by the spectroscopic parameters used in the MUSICA IASI retrievals (HITRAN 2016 database).

The comparison of Fig. 8b and e with Fig. 8c and f reveals that by an a posteriori combination of the simultaneously retrieved CH_4 and N_2O values one can reconstruct a product (CH_4^*) whose latitudinal variation can be better observed in the MUSICA IASI data than the latitudinal variation in CH_4. This is in agreement with the lower scatter we observe between HIPPO and MUSICA IASI CH_4^* if compared to the scatter for CH_4. Table 4 documents CH_4^* scatter values of 1.7 and 1.6 % for 4.2 and 9.8 km altitude, respectively. However, at the same time the bias in CH_4^* at 4.2 km is much larger than the respective bias in CH_4. The improvement of the precision and the possibility of an increased bias have been predicted by the error estimation of Sect. 3.3.

Figure 9 shows how the difference between MUSICA IASI and HIPPO reference depends on the latitude; i.e. it investigates the latitudinal dependency of the MUSICA IASI data in more detail. For the 4.2 km retrieval altitude we observe that the difference between MUSICA IASI and HIPPO N_2O and CH_4 concentrations increases from low latitudes to

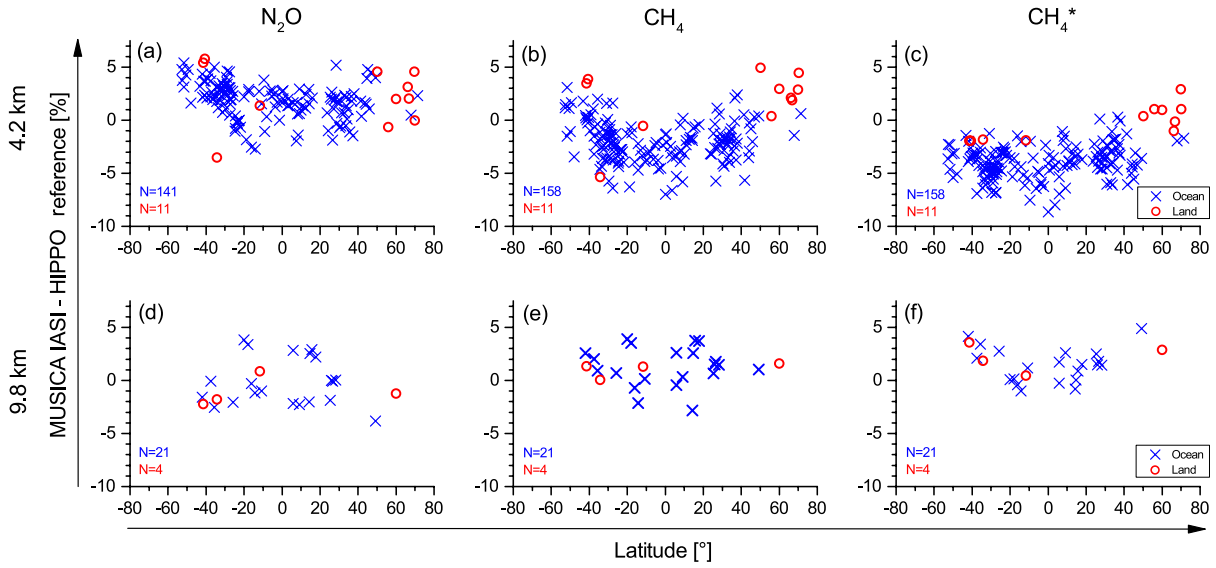

Figure 9. Latitudinal dependence of the difference between MUSICA IASI products and HIPPO data: **(a–c)** for the altitude of 4.2 km a.s.l.; **(d–f)** for the altitude of 9.8 km a.s.l.; **(a)** and **(d)** for N_2O; **(b)** and **(e)** for CH_4; and **(c)** and **(f)** for CH_4^*. Blue crosses and red circles are for IASI observations over ocean and land, respectively.

high latitudes. For N_2O the mean difference is about +1 % in the 30° S–30° N latitudinal belt, but about +3.5 % south of 40° S and north of 40° N. For CH_4 the mean difference is about −3 % in the 30° S–30° N latitudinal belt and about +2 % at high latitudes (inconsistency of 5 %). In the CH_4^* product this latitudinal inconsistency is effectively reduced and the mean difference between 60° S and 50° N is consistently at about −3.5 %. North of 50° N the mean difference in CH_4^* is about 0 %, whereby the respective measurements are done over land surface. Actually it seems that the MUSICA IASI CH_4^* data obtained from spectra measured over land surface have a different bias than the MUSICA IASI CH_4^* data corresponding to measurements over the ocean.

For comparison at the 9.8 km retrieval altitude the limited number of HIPPO profile data available make it difficult to draw robust conclusions on the latitudinal dependencies. We find no clear indication that the difference between the 9 km MUSICA IASI and HIPPO CH_4 data depends on the latitude. However, it seems that there is some latitudinal dependency in the N_2O and CH_4^* data.

4.5 Discussion

There already have been comparisons between aircraft in situ and IASI CH_4 products obtained by other research groups. For example, Xiong et al. (2013) found a low bias compared to HIPPO aircraft profiles of −1.69 % (approximately 30 ppbv) with a residual scatter of 1.13 % (approximately 23 ppbv) in the integrated 300–374 hPa layer (which typically corresponds to about 8–10 km altitude) for a collocation window with a distance of 200 km. In a study limited to the tropics Crevoisier et al. (2013) compared IASI and CARIBIC aircraft measurements of CH_4 at 11 km for 4° × 4° averages and found a high bias of 7 ppbv (approximately 0.5 %) with a scatter of 13 ppbv (approximately 0.8 %).

Similar to our study Siddans et al. (2017) compared the HIPPO profile data to IASI retrieval results for different altitude regions. They worked with averaged mixing ratios for two layers: from the surface to 6 km a.s.l. and from 6 km to 12 km a.s.l.. For the near-surface layer they report a scatter of about 40 ppbv (corresponding to about 2.1 %) and for the upper layer of about 30 ppbv (corresponding to about 1.7 %), respectively. These scatter values are close to what we found for the retrieval altitudes of 4.2 and 9.8 km (see Table 4). Close to the surface their bias (IASI–HIPPO) is negative and in the upper layer it is positive. This behaviour is in agreement with our findings; however, their bias values are smaller than our values as listed in Table 4.

Concerning N_2O, Masiello et al. (2016) has recently shown that N_2O global distributions could be obtained for each single IASI IFOV with a theoretical precision of better than 1–2 %. To our knowledge our study is the first where an extensive IASI N_2O data set is experimentally validated, and it is interesting to see that our validation results are close to the theoretical estimations of Masiello et al. (2016).

With the comparison to the HIPPO data we can document to what extent the MUSICA IASI products are able to detect the latitudinal gradients of N_2O and CH_4 in the free troposphere and in the UTLS region (at 9.8 km). We can prove that the MUSICA IASI CH_4 data do reasonably capture the latitudinal gradients well as present in the real atmosphere. On the other hand the MUSICA IASI N_2O product is apparently not precise enough to reflect the very small latitudi-

nal variations in the real atmosphere well. Nevertheless, the MUSICA strategy of retrieving N_2O concentrations simultaneously with CH_4 concentrations is very helpful, since by combining the N_2O product with the CH_4 product it is possible to create an a posteriori-corrected CH_4^* product, whose latitudinal gradient agrees even better with the HIPPO reference than the latitudinal gradient of CH_4. In Appendix B we present example maps of the global distribution of the MUSICA IASI CH_4 and CH_4^* products.

5 Comparison to references covering long time periods

In this section we analyse continuous time series and investigate the capability of the MUSICA IASI products for detecting the variations with time. We analyse 10 years of MUSICA IASI data (between the end of 2007 and the end of 2017) at three different locations that are representative for low, middle and high latitudes. Appendix C shows the time series of daily mean data obtained for our low-latitude reference site situated in the subtropical northeastern Atlantic. As reference data we use WMO–GAW in situ data and NDACC ground-based remote sensing data. Figure 7 indicates the geographical locations of the GAW in situ instruments (green diamonds) and the three NDACC sites (red circles).

The comparisons are shown for the N_2O, CH_4 and CH_4^* products. In addition, the following figures contain comparisons of the CH_4' product. This is an a posteriori-corrected product that is presented and discussed in Sect. 7.

5.1 Free-tropospheric in situ data

In the framework of the WMO–GAW programme, ground-level in situ atmospheric measurements of the main greenhouse gases have been routinely carried out at different globally distributed sites since 1980s. In particular, CH_4 and N_2O amounts have been mainly measured by the gas chromatography technique with flame ionization detection (GC-FID) for CH_4 and with electron capture detection (GC-ECD) for N_2O. In recent years, optical techniques like cavity ring-down spectroscopy (CRDS) and off-axis integrated cavity output spectroscopy (OA-ICOS) have been introduced, showing similar or even better precision than the traditional GC systems (Sepúlveda et al., 2014, and references therein). As a reference of the required data quality of the WMO–GAW records, the GAW network compatibility among laboratories and central facilities is defined as ± 2 ppbv for CH_4 and ± 0.1 ppbv for N_2O (for global background troposphere, WMO, 2016).

The WMO–GAW stations selected for this study are the Izaña Atmospheric Observatory (28.3° N), representative of the subtropical region; and the Jungfraujoch (46.5° N) and Schauinsland (47.9° N) sites, representative of middle latitudes. Izaña is a high-mountain observatory on Tenerife Island, above a well-established thermal inversion layer and affected by the quasi-permanent subsidence regime typical of the subtropical regions. This makes the in situ and remote sensing observations taken at Izaña representative of the North Atlantic free troposphere (particularly at nighttime, Cuevas et al., 2015). Jungfraujoch is also a high-mountain observatory, located in the centre of Europe and surrounded by highly industrialized regions at much lower altitudes. This special location offers the opportunity to investigate the atmospheric background conditions over central Europe and the mixing of air masses between the planetary boundary layer and the free troposphere (Bader et al., 2017, and references therein). The European regional signal is also monitored at Schauinsland, which is located in the southern part of the Black Forest mountain range near the top of mount Schauinsland, surrounded by forests and meadows (Nieneröwski, 2004) and about 170 km north of Jungfraujoch.

5.1.1 Collocation and data filtering

The remote sensing IASI data represent large-scale signals well, so the GAW in situ data have to be conveniently filtered to ensure a feasible intercomparison. At Izaña GAW CH_4 and N_2O nighttime data (from 20:00 to 08:00 UTC) are reasonably representative of background regional signal and well suited for their comparison to remote sensing observations (e.g. Sepúlveda et al., 2012). We pair these data with all IASI observations made between 15.8 and 17.2° W and between 27.2 and 28.4° N during the coinciding evening at about 22:30 UTC and the next morning at about 10:30 UTC. The filtering for the Jungfraujoch GAW data is done by comparing it to the nearby GAW station Schauinsland. We identify the regional-scale signals as the signals that are common in the Schauinsland and Jungfraujoch data (filtering of correlated variations, Sepúlveda et al., 2014). In addition, we only work with nighttime data (from 19:00 to 07:00 UTC). Similar to Izaña we then pair the GAW data with IASI observations made between 7.4 and 9.5° E and between 47.9 and 49.4° N during the coinciding evening at about 21:00 UTC and the next morning at about 09:00 UTC.

Since we want to evaluate the MUSICA IASI data in the free troposphere, we only work with MUSICA IASI data that have sufficient sensitivity at these altitudes (i.e. retrieval products that are mainly affected by the measured IASI spectra and not the a priori information). We analyse the MUSICA IASI sensitivities according to Eq. (18) and filter out data if the c_{sen} value at 4.2 km is smaller than 50 %. For all valid coincidences we calculate the daily night means.

5.1.2 Correlation, bias and scatter

Figure 10 shows the correlation between the MUSICA IASI and GAW data. The yellow star represents the unique a priori data used for all MUSICA IASI retrievals. For N_2O and for Tenerife we observe very weak correlations (R^2 values of about 5 %). In particularly the 3 years 2012–2014 (indi-

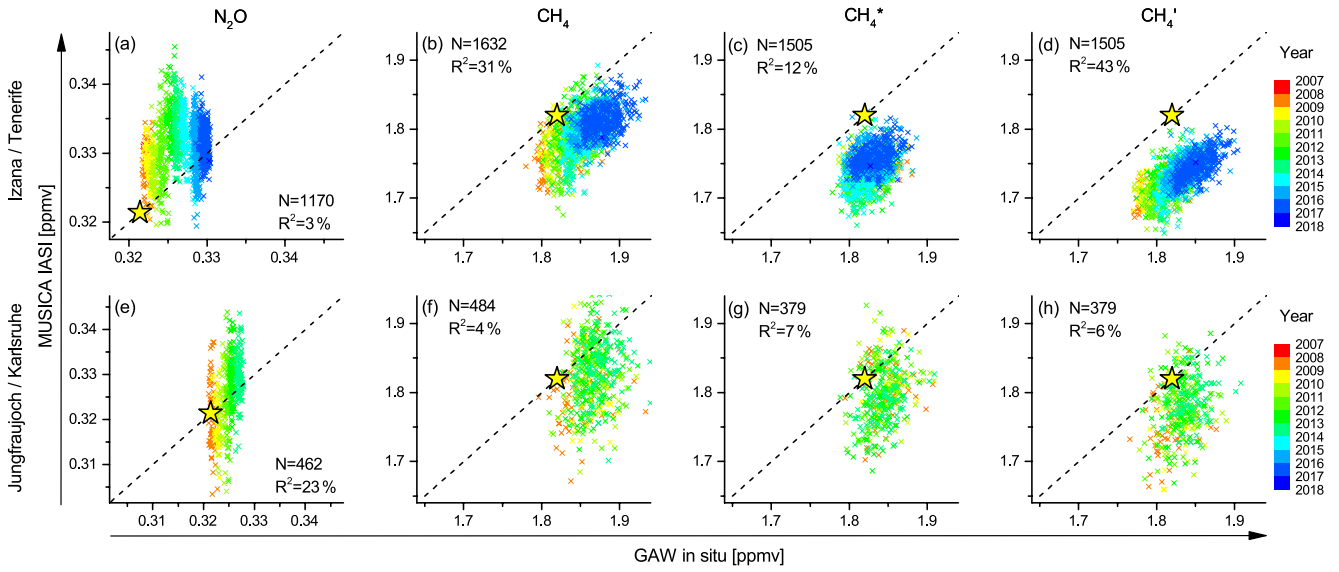

Figure 10. Correlation plots between daily night mean MUSICA IASI 4.2 km retrieval products and GAW in situ data from high-mountain observatories: **(a–d)** for the surroundings of Tenerife Island; **(e–h)** for the surroundings of Karlsruhe; **(a)** and **(e)** for N_2O; **(b)** and **(f)** for CH_4; **(c)** and **(g)** for CH_4^*; and **(d)** and **(h)** for CH_4'. A description of the CH_4^* and CH_4' products is given in Table 2. The colour code indicates the year of observation, the yellow star represents the a priori data used for the retrievals and the black dashed line is the one-to-one diagonal. Number of considered days (N) and R^2 values are given in each panel (all correlations are positive and significant on the 95 % confidence level).

Table 5. Similar to Table 4, but for the difference with respect to GAW data (MUSICA IASI−GAW), for all daily mean data in the 2007–2016 time period and for MUSICA IASI retrievals at 4.2 km.

Site		N_2O	CH_4	CH_4^*	CH_4'
Izaña	Days	1170	1632	1505	1505
(2007–2016)	Bias	−0.4 %	−4.9 %	−4.5 %	−5.5 %
	Scatter	1.3 %	1.4 %	1.4 %	1.1 %
Jungfraujoch	Days	462	484	379	379
(2007–2013)	Bias	+6.9 %	−2.9 %	−5.6 %	−5.5 %
	Scatter	2.1 %	2.7 %	2.3 %	2.4 %

cated by dark green and bright blue colours) deviate from the one-to-one diagonal (indicated by black dashed line). There seems to be an inconsistency in the MUSICA IASI data from different years. For a brief documentation and discussion of possible long-term inconsistencies or discontinuities please refer to Appendix C. Table 5 collects the bias and scatter value obtained from the daily mean differences. Similarly to Table 4 we estimate the bias by calculating the median of all differences and the scatter by calculating the IP68 values of all differences. We get a scatter for N_2O of 1.3 %, i.e. even smaller than the scatter observed for the difference with respect to HIPPO data. The fact that a scatter of only about 1 % is still not sufficient for achieving a good correlation is partly due to the weakness of the temporal variations of lower-tropospheric N_2O.

For CH_4 and at Tenerife a linear correlation between GAW and MUSICA IASI is clearly visible (see Fig. 10b). The R^2 value is 31 %. Data corresponding to the beginning of the time series (before 2009, red, orange and yellow colours) form clusters corresponding to low CH_4 concentrations and vice versa, and data corresponding to the end of the time series (after 2015, blue colours) cluster at high CH_4 concentrations. Apparently, an important part of the CH_4 variations is due to the continuous free-tropospheric CH_4 increase and it is similarly observed in the GAW and the MUSICA IASI data. For CH_4^* (Fig. 10c) the R^2 value is only 12 %, i.e. significantly smaller than for CH_4. All data points cluster in the form of a single data point cloud. It seems that removing the variations as present in the retrieved N_2O data from the retrieved CH_4 data (see Eq. 11) does not only reduces the errors, but instead also removes most of the long-term CH_4 signals.

The comparison at Karlsruhe is limited to the 2007–2013 time period. In this time period we observe a reasonable correlation for N_2O (R^2 value of 23 %), which is similar to Tenerife, where the correlation is also reasonable if we limit to the 2007–2013 time period. For CH_4 and CH_4^* there are positive correlations that are clearly significant at the 95 % confidence level; however, the correlation coefficients R^2 are only 4 and 7 %, respectively.

As aforementioned the Izaña nighttime GAW measurements represent the free troposphere well; however, a strict quantitative interpretation of the bias and scatter of the dif-

ference between a GAW measurement at an altitude of about 2.4 km and a remote sensing measurement, which is typically representative for the altitudes between 2 and 8 km, is not possible. Nevertheless, the bias and scatter values as collected in Table 5 are a helpful confirmation of the results obtained by the comparison to the HIPPO profiles. For the comparison with the GAW data we find a scatter of 1.4 % for CH_4 and CH_4^*, which is even smaller than the respective scatter as observed when comparing to the HIPPO profiles (see Table 4). And in agreement with the comparison to HIPPO we find clear indications of a negative bias in the free-tropospheric MUSICA IASI CH_4 and CH_4^* products.

The scatter between Jungfraujoch GAW and MUSICA IASI data is 2.1, 2.7 and 2.3 % for N_2O, CH_4 and CH_4^*, respectively. These high values indicate important differences between the two data sets and a more detailed analysis is needed to be able to draw conclusions from this comparison.

5.2 Ground-based remote sensing network data

Since the late 1990s changes in the atmospheric composition have been routinely monitored by FTIR experiments distributed worldwide in the framework of the NDACC Infrared Working Group (IRWG, De Mazière et al., 2018). From the global ground-based FTIR stations we have selected three sites covering very different atmospheric conditions in the Northern Hemisphere: Izaña (28.3° N), Karlsruhe (49.1° N) and Kiruna (67.8° N) at subtropical, middle and polar latitudes, respectively. Their location is marked in Fig. 7 by the red circles. The Kiruna FTIR instrument is located at the Swedish Institute of Space Physics (IRF) in the boreal forest region of northern Sweden, which is not significantly affected by regional anthropogenic pollution. This site is well suited for the study of the Arctic polar atmosphere since the stratospheric polar vortex frequently covers Kiruna during the winter and early spring (Blumenstock et al., 2006; Bader et al., 2017). The Karlsruhe site is located in a flat terrain inside the Karlsruhe Institute of Technology (KIT, Campus North, Germany) and, thus, is representative of the European continental background. The Izaña FTIR instrument is placed at the Izaña Atmospheric Observatory, already described in Sect. 5.1. Izaña and Kiruna are recording middle infrared spectra within NDACC since 1999 and 1996, respectively (Blumenstock et al., 2006; Schneider et al., 2006). Although Karlsruhe is not a NDACC site, it has been an official TCCON station since 2010 and also measures down to the middle infrared ($\approx 2000\,cm^{-1}$), a region that is traditionally covered by NDACC spectrometers (Sepúlveda et al., 2014, and references therein).

The evaluation of the FTIR high-resolution infrared solar absorption spectra gives information about the vertical distribution of many different atmospheric trace gases, including CH_4 and N_2O. In contrast to the MUSICA IASI processing the NDACC FTIR CH_4 and N_2O products are generated by two independent retrieval procedures and, for the selected FTIR sites, the retrieval code PROFFIT (PROFile FIT, Hase et al., 2004) is used. The NDACC FTIR retrievals analyse the 2481–2541 cm^{-1} and the 2611–2943 cm^{-1} spectral regions for N_2O and CH_4, respectively, and account for the different interfering absorption signatures of H_2O, CO_2, O_3 and CH_4 for the N_2O retrieval and H_2O, HDO, CO_2, O_3, N_2O, NO_2, HCl and OCS for the CH_4 retrieval. As a priori profiles of the target gases, the climatological entries from WACCM (https://www2.acom.ucar.edu/, last access: 11 July 2018) provided by NCAR (National Centre for Atmospheric Research) are used. This a priori information varies from site to site but for an individual site it is kept constant through the whole considered period; i.e. it does not vary depending on season. All the FTIR stations apply the 12:00 UTC temperature and pressure profiles from the NCEP (National Centers for Environmental Prediction) database. The spectroscopic line parameters have been taken from HITRAN 2008 database (Rothman et al., 2009). The good quality of the long-term NDACC FTIR N_2O and CH_4 data has been documented by theoretical and experimental validation studies (e.g. Schneider et al., 2005; Angelbratt et al., 2011; Sepúlveda et al., 2012, 2014). Because NDACC FTIR provides information on the vertical distribution of N_2O and CH_4 with a precision estimated to be better than 1 % (Sepúlveda et al., 2014; García et al., 2016), it is an indispensable reference for validating IASI N_2O and CH_4 profile retrievals. However, the NDACC FTIR N_2O and CH_4 data can have systematic errors of about 2 % (Sepúlveda et al., 2014) due to uncertainties in the used spectroscopic parameters.

5.2.1 Collocation and data treatment

The spatial collocation of IASI and NDACC FTIR observations is done according to Wiegele et al. (2014); i.e. we work with all IASI observations that fall within a box of approximately 110 km × 110 km south of the FTIR stations (for the surroundings of Tenerife and Karlsruhe it is the same box as that used in Sect. 5.1). Then we pair the MUSICA IASI observations with all the NDACC FTIR observations made between 8 h before and after the IASI observation.

We adjust the NDACC FTIR data to the unique a priori data used by the MUSICA IASI retrieval and properly account for the different vertical resolution and sensitivity of the two remote sensing products. Details on this NDACC FTIR data treatment are given in Appendix D.

In a second step we filter out all the pairs with MUSICA IASI data having reduced sensitivity by requiring $c_{sen} < 0.5$ (according to Sect. 3.2). This is done individually for the three products N_2O, CH_4 and CH_4^*; the altitude of 4.2 km; and the altitudes representing the UTLS region (12.0, 10.9 and 9.8 km for Tenerife, Karlsruhe and Kiruna, respectively). For the remaining data pairs we calculate daily averages. This leaves us with about 750, 600 and 200 data pairs for Tenerife, Karlsruhe and Kiruna (please note that the sensitivity filter

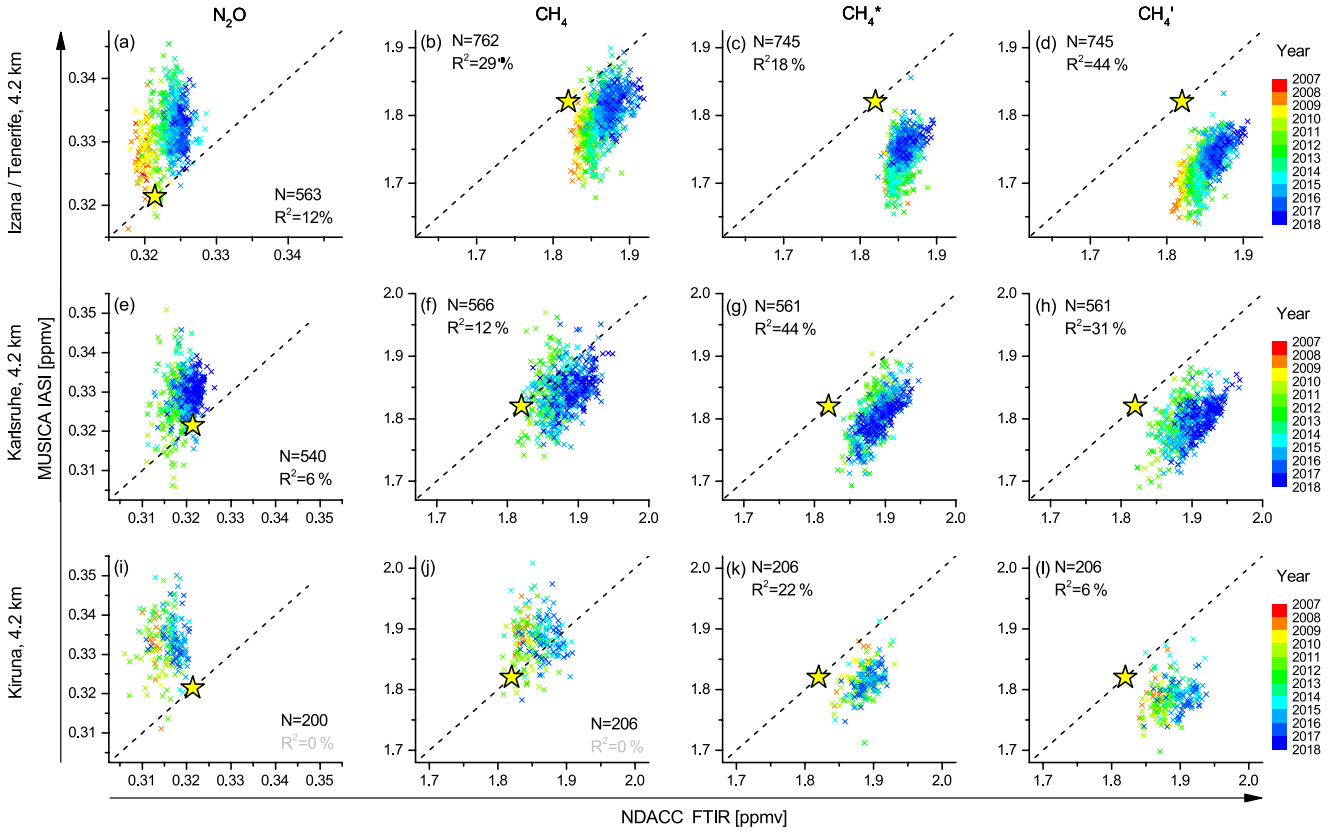

Figure 11. Same as Fig. 10, but for correlation between the daily mean MUSICA IASI products (4.2 km retrievals) and NDACC FTIR products (4.2 km retrievals): **(a–d)** for the surroundings of Tenerife Island; **(e–h)** for the surroundings of Karlsruhe; **(i–k)** for the surroundings of Kiruna; **(a)**, **(e)** and **(i)** for N_2O; **(b)**, **(f)** and **(j)** for CH_4; **(c)**, **(g)** and **(k)** for CH_4^*; and **(d)**, **(h)** and **(l)** for CH_4'. R^2 values in black indicate significant positive correlations (95 % confidence level) and grey indicate no significance.

generally removes more data for the altitude of 4.2 km than for the UTLS region and more data for the N_2O product than for the CH_4 product).

5.2.2 Correlation, bias and scatter

Figures 11 and 12 show the correlation between the NDACC FTIR and the MUSICA IASI data for 4.2 km altitude and for altitudes representing the UTLS region, respectively.

For 4.2 km altitude (Fig. 11) we find best correlations for the CH_4 product at Tenerife and the CH_4^* product at Karlsruhe and Kiruna, with R^2 values between 20 and 45 %. The colour code represents the years of the measurements and indicates that the MUSICA IASI and the NDACC FTIR CH_4 and CH_4^* concentrations are generally lower at the beginning of the analysed period (red-yellow, i.e. 2007–2009) than at its end (blue, i.e. 2016–2017). A similar clustering is also seen in the N_2O data; however, there the correlation coefficients are significantly weaker. We get a significant positive correlation (significance at the 95 % confidence level) for CH_4^* at all three sites and for N_2O and CH_4 at Tenerife and Karlsruhe. Table 6 collects the bias (median of the difference between MUSICA IASI and NDACC FTIR) and the scatter (IP68 of the difference). We find a scatter for CH_4^* of about 1.3 %, which is generally smaller than the scatter of 1.3–1.9 % we find for CH_4 or N_2O. This is in agreement with Table 4 (altitude 4.2 km) and Table 5. Concerning the bias, at all three sites MUSICA IASI N_2O concentrations are systematically higher than NDACC FTIR concentrations. The bias in CH_4 is significantly negative at the low-latitude site (Izaña), not significant at the mid-latitude site (Karlsruhe) and significantly positive at the high-latitude site (Kiruna). The latitudinal inconsistency of the CH_4 bias confirms the results obtained from the comparison to HIPPO data (see Table 4 and Fig. 9a–c). For CH_4^* this inconsistency is strongly reduced (bias is negative at all sites), which is also in agreement with the HIPPO comparison results.

For the UTLS altitude region (Fig. 12) at all sites and for all products the correlations are positive and significant at the 95 % confidence level. The correlations are stronger for CH_4 than for N_2O, with R^2 values being situated between 37 and 55 % and between 16 and 26 %, respectively. For CH_4^* the correlations are rather weak. As briefly discussed in Sect. 5.1 the calculations according to Eq. (11) seem to

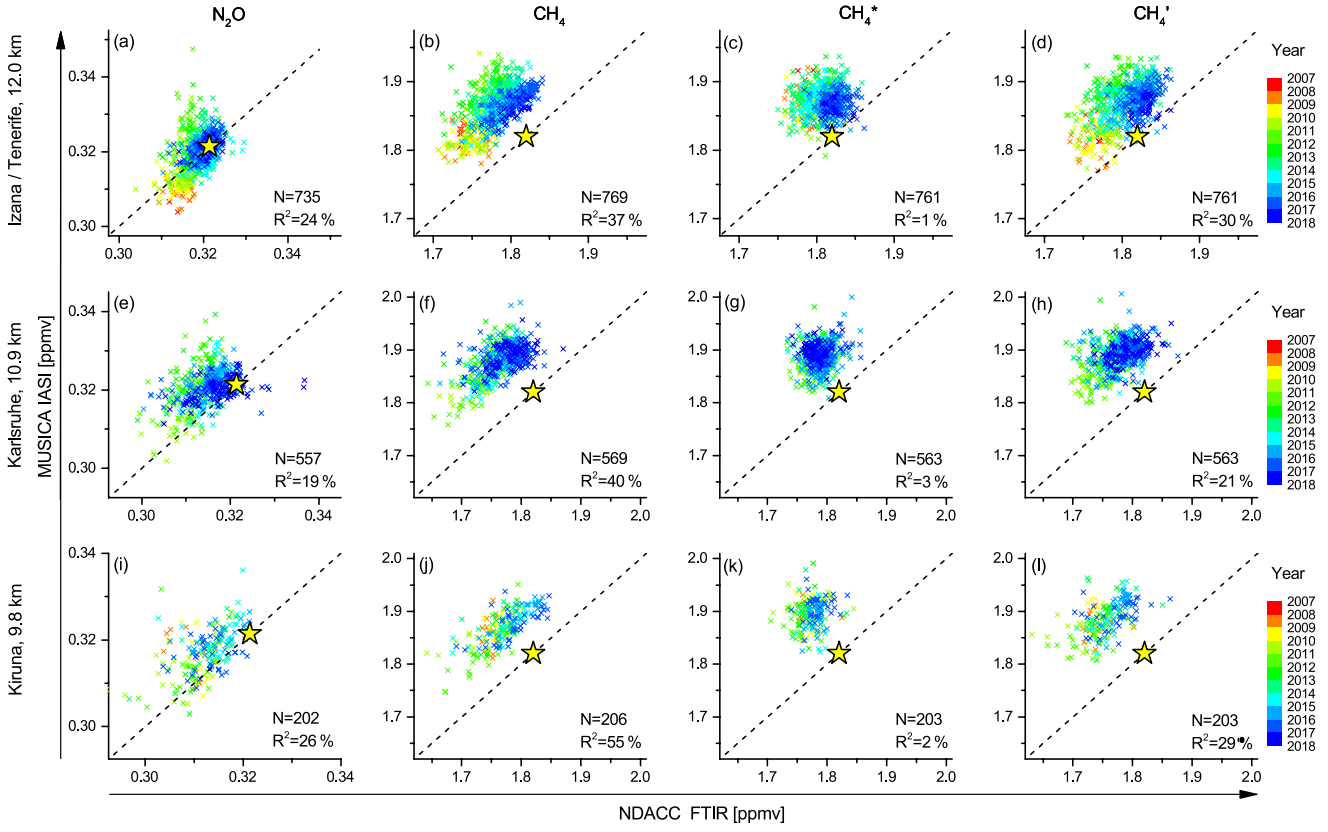

Figure 12. Same as Fig. 11, but for correlations at altitudes representing the UTLS regions.

Table 6. As Table 5, but for the difference with respect to NDACC FTIR data (MUSICA IASI−NDACC FTIR) at the three sites of Tenerife, Karlsruhe and Kiruna and for retrievals at 4.2 km.

Site		N_2O	CH_4	CH_4^*	CH_4'
Izaña	Days	563	762	745	745
(2007–2017)	Bias	+2.9 %	−5.8 %	−6.2 %	−7.7 %
	Scatter	1.3 %	1.6 %	1.3 %	1.2 %
Karlsruhe	Days	540	566	561	561
(2010–2017)	Bias	+5.1 %	+0.1 %	−4.4 %	−4.7 %
	Scatter	1.5 %	1.9 %	1.3 %	1.5 %
Kiruna	Days	200	206	206	206
(2007–2016)	Bias	+7.3 %	+2.7 %	−4.1 %	−4.6 %
	Scatter	1.9 %	2.3 %	1.4 %	1.6 %

Table 7. As Table 6, but for retrievals in the UTLS region (Tenerife: 12 km; Karlsruhe: 10.9 km; Kiruna: 9.8 km).

Site		N_2O	CH_4	CH_4^*	CH_4'
Izaña	Days	735	769	761	761
(2007–2017)	Bias	−0.5 %	+2.8 %	+3.2 %	+2.6 %
	Scatter	1.3 %	1.3 %	1.4 %	1.4 %
Karlsruhe	Days	557	569	563	563
(2010–2017)	Bias	+1.5 %	+5.1 %	+5.2 %	+4.6 %
	Scatter	1.5 %	1.5 %	1.5 %	1.5 %
Kiruna	Days	202	206	203	203
(2007–2016)	Bias	+1.8 %	+2.3 %	+3.9 %	+4.3 %
	Scatter	1.5 %	1.4 %	1.5 %	1.5 %

reduce not only the errors, but instead they also remove a lot of real atmospheric CH_4 signals. Table 7 gives the bias and scatter obtained for the different MUSICA IASI products by comparison to the NDACC FTIR data for the UTLS altitude region. We observe that the scatter in CH_4^* is not reduced if compared to the scatter in CH_4 and that MUSICA IASI CH_4 and CH_4^* values are systematically higher than the respective NDACC FTIR values. Such positive bias is also observed when comparing to the HIPPO data at 9.8 km (see Table 4). For N_2O we found indications of a weak negative bias, which is also in agreement with the HIPPO comparison (see Table 4).

6 Timescale analyses of detectable signals

In this section the N_2O and CH_4 variations on different timescales are analysed. The objective is to use the long time period comparisons as presented in the previous section for

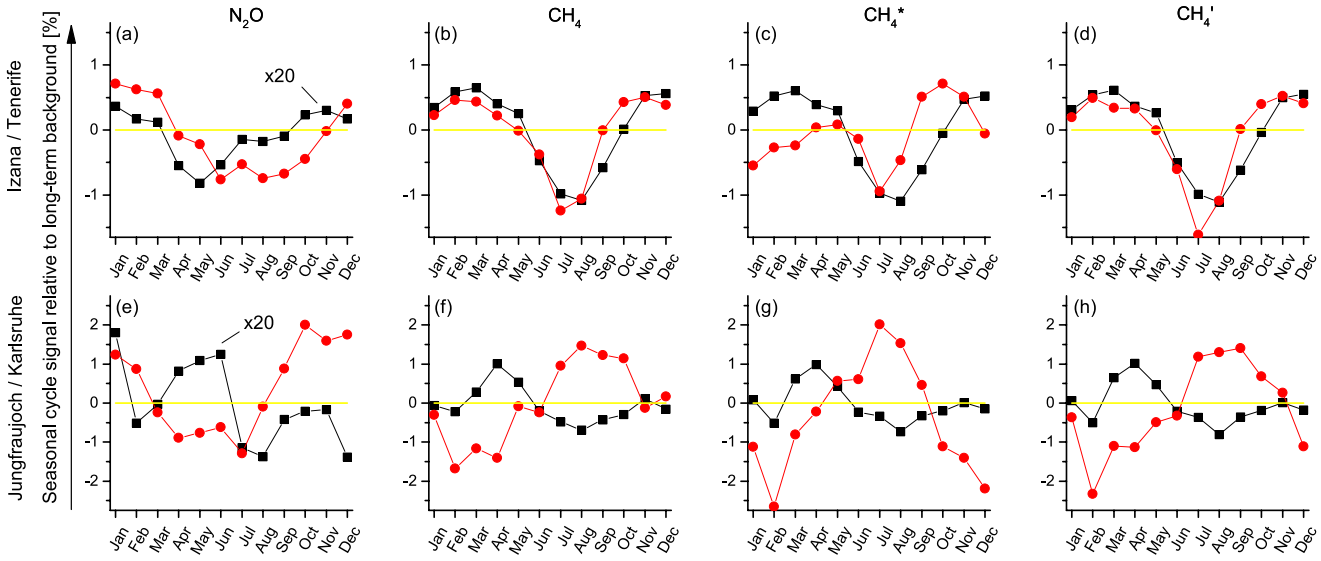

Figure 13. Seasonal cycle as obtained from the daily night mean MUSICA IASI products (4.2 km retrieval, red) and coinciding GAW high-mountain observatory in situ data (black): **(a–d)** for the surroundings of Tenerife Island; **(e–h)** for the surroundings of Karlsruhe; **(a)** and **(e)** for N_2O; **(b)** and **(f)** for CH_4; **(c)** and **(g)** for CH_4^*; and **(d)** and **(h)** for CH_4'. A description of the CH_4^* and CH_4' products is given in Table 2. The yellow line indicates the a priori data (fixed a priori value, i.e. no seasonal cycle signal). The N_2O GAW signals (**a** and **e**) are multiplied by a factor of 20.

documenting the kind of signals that can be observed in the MUSICA IASI data. For this purpose we break down the time series signal $x(t)$ step by step into signals belonging to different timescales.

$$\begin{aligned} x(t) &= \overline{x_m([t_1,t_2])} + [x(t) - \overline{x_m([t_1,t_2])}] \\ &= \overline{x_m([t_1,t_2])} + s(t) + [x(t) - \overline{x_m([t_1,t_2])} - s(t)] \\ &= \overline{x_m([t_1,t_2])} + s(t) + l(t) + [x(t) - \overline{x_m([t_1,t_2])} \\ &\quad -s(t) - l(t)] \\ &= \overline{x_m([t_1,t_2])} + s(t) + l(t) + d(t) \end{aligned} \quad (21)$$

Firstly, we calculate the mean value $\overline{x_m([t_1,t_2])}$ for a reference period $[t_1,t_2]$. In order to ensure that the mean value of the reference period is not affected by irregularly sampled data (e.g. there might be more days with measurements in summer than in winter) we use a time series model, which is similar to the one used in Gardiner et al. (2008) and Sepúlveda et al. (2014). The time series model considers a mean value and variations on different timescales: a linear trend, intra-annual variations and inter-annual variations (details on the model are given in Appendix C). The model is fitted to the time series, and with the fit results we can calculate a regularly sampled time series and thus an $\overline{x_m([t_1,t_2])}$ value being best representative for the reference period $[t_1,t_2]$. Resting the mean reference value from the time series we get a residual signal (in square brackets in Eq. 21, first line) that represents all the variations with respect to the reference period. These variations are dominated by two signals: the long-term increase and the seasonal cycle. The fit results of the aforementioned time series model are now used for a first-guess separation of the seasonal cycle and long-term signals. By removing the modelled variations that take place on timescales longer than the seasonal cycle (mean value, the linear trend and the inter-annual variations) from the time series data we get a signal that is mainly due to the seasonal cycle. From this signal we calculate the mean for each month (independently from the year). This gives us the mean seasonal cycle $s(t)$. In the next step we calculate a new residual $[x(t) - \overline{x_m([t_1,t_2])} - s(t)]$, i.e. the residual signal after removing the seasonal cycle (the deseasonalized time series). Then we calculate monthly mean values from the deseasonalized data, which gives us the deseasonalized long-term signal $l(t)$. The residual signal after removing the seasonal cycle and long-term signal represents the variations on a daily timescale $d(t) = [x(t) - \overline{x_m([t_1,t_2])} - s(t) - l(t)]$. This time series separation is done identically for all products and all the data pairs, i.e. for the MUSICA IASI and GAW pairs, and for the different MUSICA IASI and NDACC FTIR pairs.

Please note that we use the time series model only for calculating a representative value for the reference period and to ensure that the seasonal cycle calculated from an irregularly sampled data does not significantly interfere with changes that take place on long timescales. The seasonal cycle $s(t)$, the deseasonalized long-term signals $l(t)$ and the day-to-day variations $d(t)$ are exclusively obtained from the data and are not subject to constraints introduced by the time series model. This approach avoids the fact that the MUSICA IASI and the reference data show correlations on different

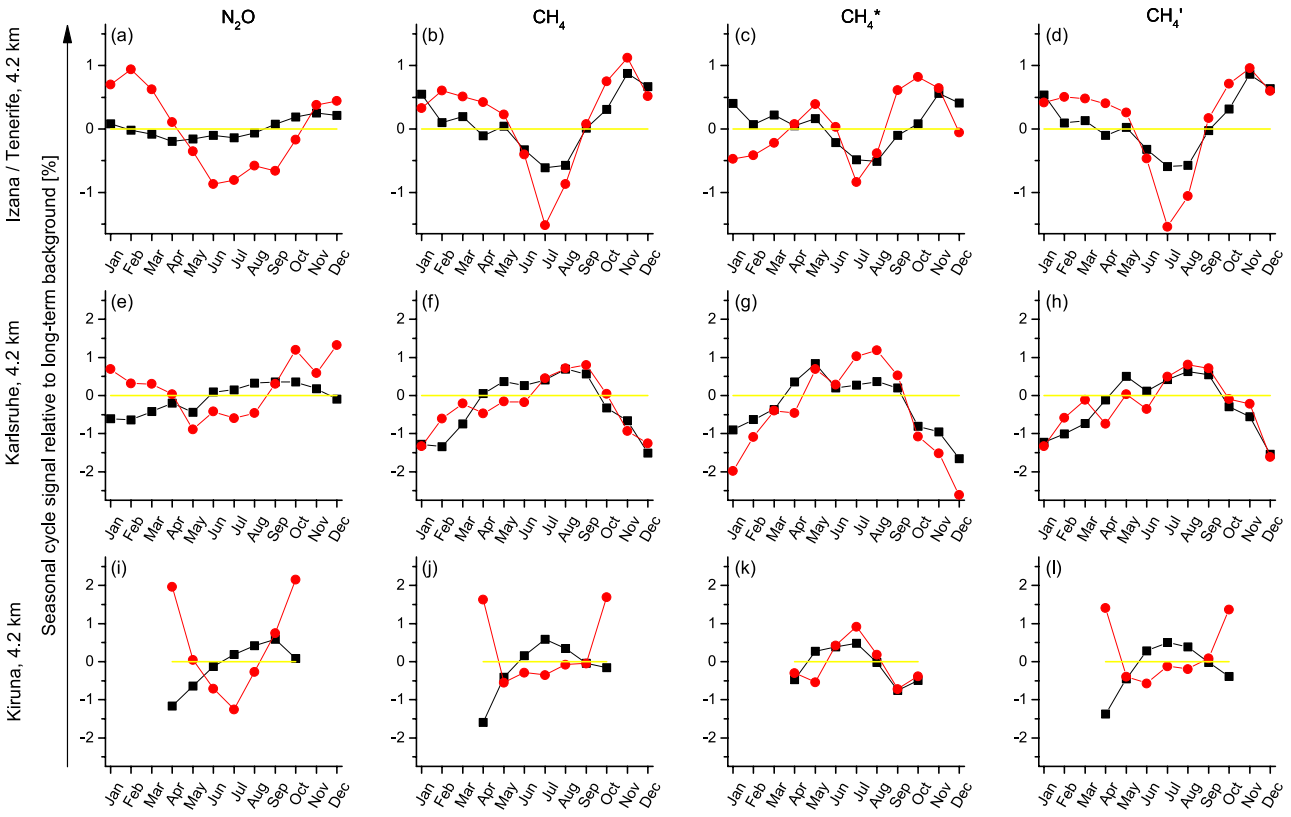

Figure 14. Same as Fig. 13, but for the daily mean MUSICA IASI products (4.2 km retrieval, red) and coinciding NDACC FTIR product (4.2 km retrieval, black): **(a–d)** for the surroundings of Tenerife Island; **(e–h)** for the surroundings of Karlsruhe; **(i–k)** for the surroundings of Kiruna; **(a)**, **(e)** and **(i)** for N_2O; **(b)**, **(f)** and **(j)** for CH_4; **(c)**, **(g)** and **(k)** for CH_4^*; and **(d)**, **(h)** and **(l)** for CH_4'.

timescales that are artificially introduced by the constraints of the time series model used.

6.1 Seasonal cycles

Figure 13 shows the seasonal cycle signals $s(t)$ as obtained for Tenerife and Karlsruhe from the paired MUSICA IASI and GAW data (red for MUSICA IASI and black for GAW). For the comparisons in the surroundings of Tenerife Island we observe a very good agreement for CH_4 in phase as well as amplitude. However, for N_2O the agreement is very poor. Both the phase and the amplitudes are different (please note that in the figure the GAW values have been multiplied by a factor of 20). For CH_4^* there is some agreement (minimum in July–August and high values in October–November); however, the agreement is clearly poorer than for CH_4. It seems that the calculations according to Eq. (11) introduce inconsistencies between MUSICA IASI and GAW data on the seasonal cycle timescale. For the comparisons in the surroundings of Karlsruhe we get no agreement. For N_2O both phase and amplitude are strongly different (please note that in the figure the GAW values have been multiplied by a factor of 20). For CH_4 and CH_4^* the GAW and MUSICA IASI amplitudes only differ by a factor of 2. However, the phases are very different. While the GAW data show a minimum in summer and a maximum in spring, for MUSICA IASI it is almost the other way round: they show a minimum between November and April and a maximum in summer.

Figure 14 shows the seasonal cycle signals as obtained from the paired MUSICA IASI and NDACC FTIR data for the three locations at Tenerife, Karlsruhe and Kiruna (red for MUSICA IASI and black for NDACC FTIR) for the 4.2 km altitude. At all three locations the agreement for N_2O is rather weak – in particular at Kiruna, where the maxima and minima of MUSICA IASI and NDACC FTIR are almost anti-correlated. At Tenerife and Karlsruhe there is a good agreement for CH_4. At Tenerife the CH_4 minimum is in both data sets in July and the maximum in November. This cycle is also observed in the paired MUSICA IASI and GAW data (recall Fig. 13b). In the NDACC FTIR data the July minimum is less pronounced than in the MUSICA IASI (and GAW) data, which we think is due to the fact that the upward-looking FTIR instrument on Tenerife is situated at about 2400 m a.s.l., thus missing the variations that take place at lower altitudes. At Karlsruhe the CH_4 maximum of MUSICA IASI and NDACC FTIR is in August–September and the minimum in winter, i.e. almost anti-correlated to

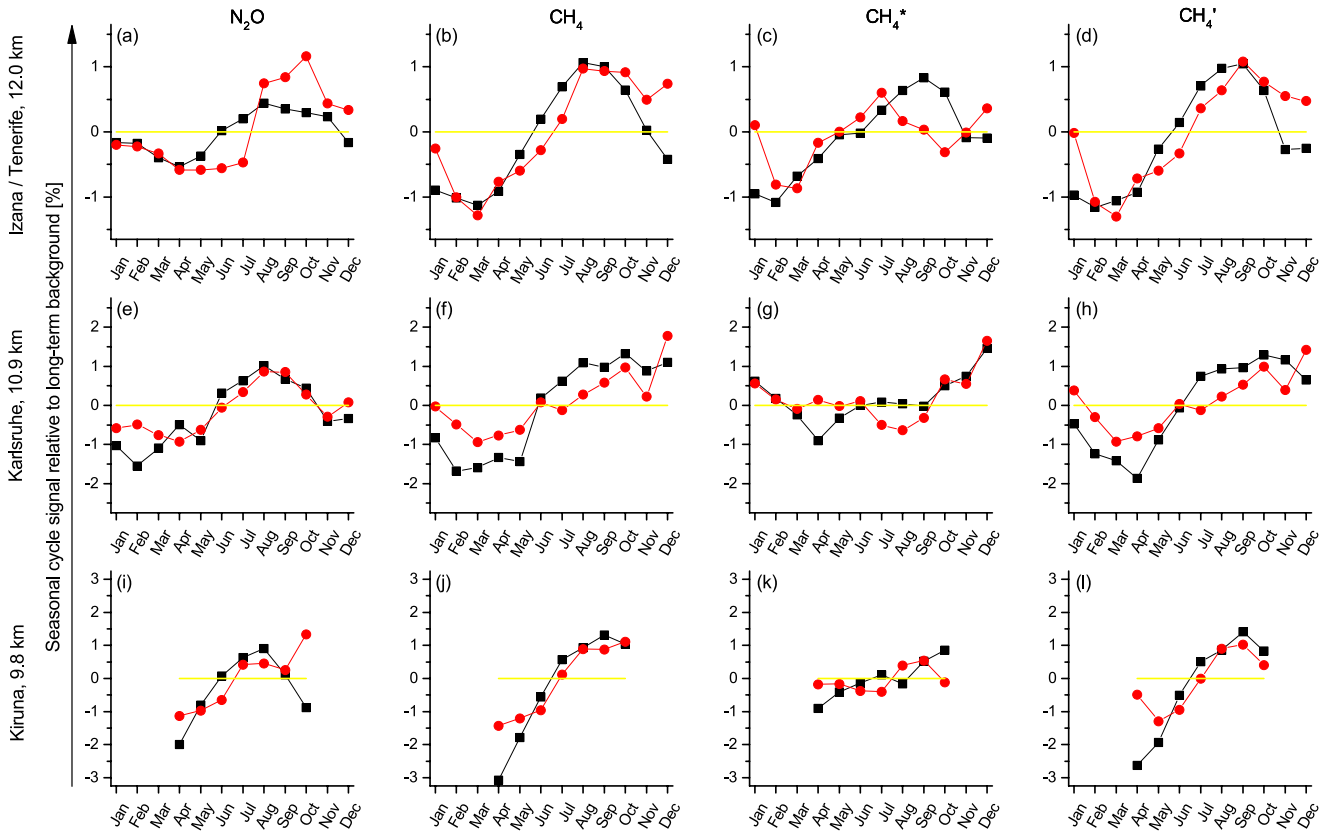

Figure 15. Same as Fig. 14, but for the seasonal cycles at altitudes representing the UTLS region.

the Jungfraujoch GAW data (recall Fig. 13f). The MUSICA IASI and the NDACC FTIR data offer similar vertical resolution and sensitivity and their good agreement demonstrates the reliability of the Karlsruhe MUSICA IASI data. However, at this site the vertical resolution and the sensitivity is not sufficient to correctly detect the seasonal cycle in the lower free troposphere, where the Jungfraujoch GAW data are the best reference. At Kiruna the agreement for CH_4 is rather weak, whereby the differences are especially strong in April and October (first and last measurements after and before winter). For CH_4^* and at Tenerife and Karlsruhe we observe a poorer agreement of the seasonal cycles than for CH_4; i.e. there the calculations according to Eq. (11) introduce seasonal timescale inconsistencies between MUSICA IASI and NDACC FTIR data. This is in contrast to Kiruna, where the agreement for CH_4^* is significantly better than for CH_4. At Kiruna we can use the combined product according to Eq. (11) for investigating seasonal cycle signals. The seasonal cycles as detected by the individual N_2O and CH_4 products seem unreliable.

Figure 15 depicts the seasonal cycle signals from paired MUSICA IASI and NDACC FTIR data for altitudes that are representative for the UTLS region. We find a reasonable agreement and similar seasonal cycles for N_2O and CH_4 at all three sites: the concentrations are typically low in late winter and spring, then almost continuously increase until the maximum concentrations at the end of summer. This seasonal variation is due to the seasonal cycle of the tropopause altitude. It is lowest after winter when N_2O and CH_4 at the considered altitudes are affected by the stratosphere, where the concentrations of both trace gases significantly decrease with increasing altitude. From spring until the end of summer the tropopause altitude increases and more and more tropospheric N_2O and CH_4 concentrations are detected. The agreement is particularly good for CH_4 and at Tenerife, where we observe a peak-to-peak increase in both MUSICA IASI and NDACC FTIR data between March and August of about 2 %. At higher altitudes the peak-to-peak amplitudes increase, which is however only partly captured by the MUSICA IASI data (at Karlsruhe and Kiruna the MUSICA IASI data show lower peak-to-peak amplitudes than the NDACC FTIR data). In the CH_4^* data we see generally weaker seasonal cycle signals than in the CH_4 data. Because both the N_2O and CH_4 seasonal cycles are mainly a consequence of the seasonal cycle in the tropopause altitude the calculation according to Eq. (11) partly cancels out these signals.

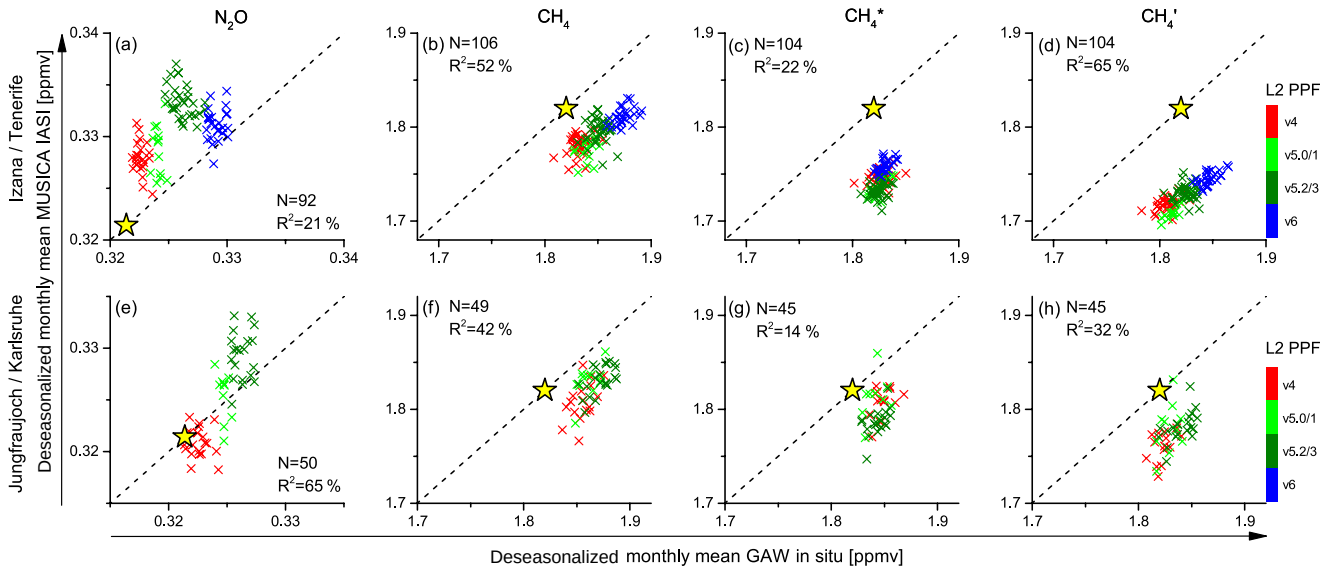

Figure 16. Correlation plots for deseasonalized monthly mean data (MUSICA IASI 4.2 km retrieval products versus GAW high-mountain observatory in situ data): **(a–d)** for the surroundings of Tenerife Island; **(e–h)** for the surroundings of Karlsruhe; **(a)** and **(e)** for N_2O; **(b)** and **(f)** for CH_4; **(c)** and **(g)** for CH_4^*; and **(d)** and **(h)** for CH_4'. A description of the CH_4^* and CH_4' products is given in Table 2. The colour code indicates periods with the different EUMETSAT L2 PPF software versions according to Table 1, the yellow star represents the a priori data used for the retrievals and the black dashed line is the one-to-one diagonal. Number of considered months (N) and R^2 values are given in each panel (all correlations are positive and significant on the 95 % confidence level).

6.2 Long-term variations

After removing the seasonal cycle signal from the time series we calculate monthly mean data and get a deseasonalized monthly mean time series $(\overline{x_m([t_1,t_2])} + l(t)$, according to Eq. 21). These data reflect long-term signals and we compare respective MUSICA IASI and reference signals in order to document the reliability of the MUSICA IASI data for detecting the long-term variation of N_2O and CH_4 concentrations.

Figure 16 correlates deseasonalized MUSICA IASI monthly mean data with respective data from the two GAW high-mountain observatories. The colour of the data points identifies data belonging to four different EUMETSAT L2 Product Processing Facility software versions, which might have an effect on the MUSICA IASI retrieval products (for a discussion refer to Appendix C). At Tenerife the comparison period is more than 9 years (between October 2007 and December 2016). This period covers data belonging to the L2 PPF software v4, v5.0–5.1, v5.2–5.3 and v6. At Karlsruhe the comparison is limited to the period between 2007 and 2013, which does not consider data belonging to the L2 PPF software v6. At the two sites we find significant positive correlations for all products (at the 95 % confidence level). At Tenerife we find an R^2 value for N_2O of 21 %, whereby the respective correlation is clearly affected by an inconsistency between data belonging to L2 PPF software v5.2–5.3 and v6. In the CH_4 comparison the inconsistency between the L2 PPF software versions is not discernible, leading to an R^2 value being larger than 50 %. At Karlsruhe the aforementioned inconsistency cannot be observed, because the comparison period does not cover v6. In consequence we get a very high R^2 value for CH_4 and N_2O of 42 and 65 %, respectively. While the previous section has demonstrated the limits of the Karlsruhe MUSICA IASI data for detecting lower-tropospheric N_2O and CH_4 seasonal cycles, here we find that the Karlsruhe MUSICA IASI data are sensitive to the lower-tropospheric long-term N_2O and CH_4 increase. This good agreement between MUSICA IASI and GAW data for a low- and middle-latitude site clearly demonstrates the reliability of the MUSICA IASI data for detecting long-term changes in free-tropospheric N_2O and CH_4 concentrations. Concerning CH_4^*, the long-term signals are strongly reduced if compared to N_2O and CH_4, because the calculations according to Eq. (11) cancel out a significant part of these signals. In consequence R^2 values for CH_4^* are weaker than for CH_4.

Figure 17 shows the correlation with NDACC FTIR data for 4.2 km. For Tenerife the comparison covers almost 10 years (between October 2007 and July 2017) and confirms the results obtained from the comparison with GAW in situ data: the correlation is positive and very significant for all products; the N_2O correlation is affected by an inconsistency between L2 PPF software v5.2–5.3 and v6; the CH_4 correlation is not affected by this inconsistency, leading to an R^2 value above 50 %; and the long-term signal in the CH_4^* data is much smaller than in the CH_4 data. For Karlsruhe the comparison covers the 2010 to 2017 time period

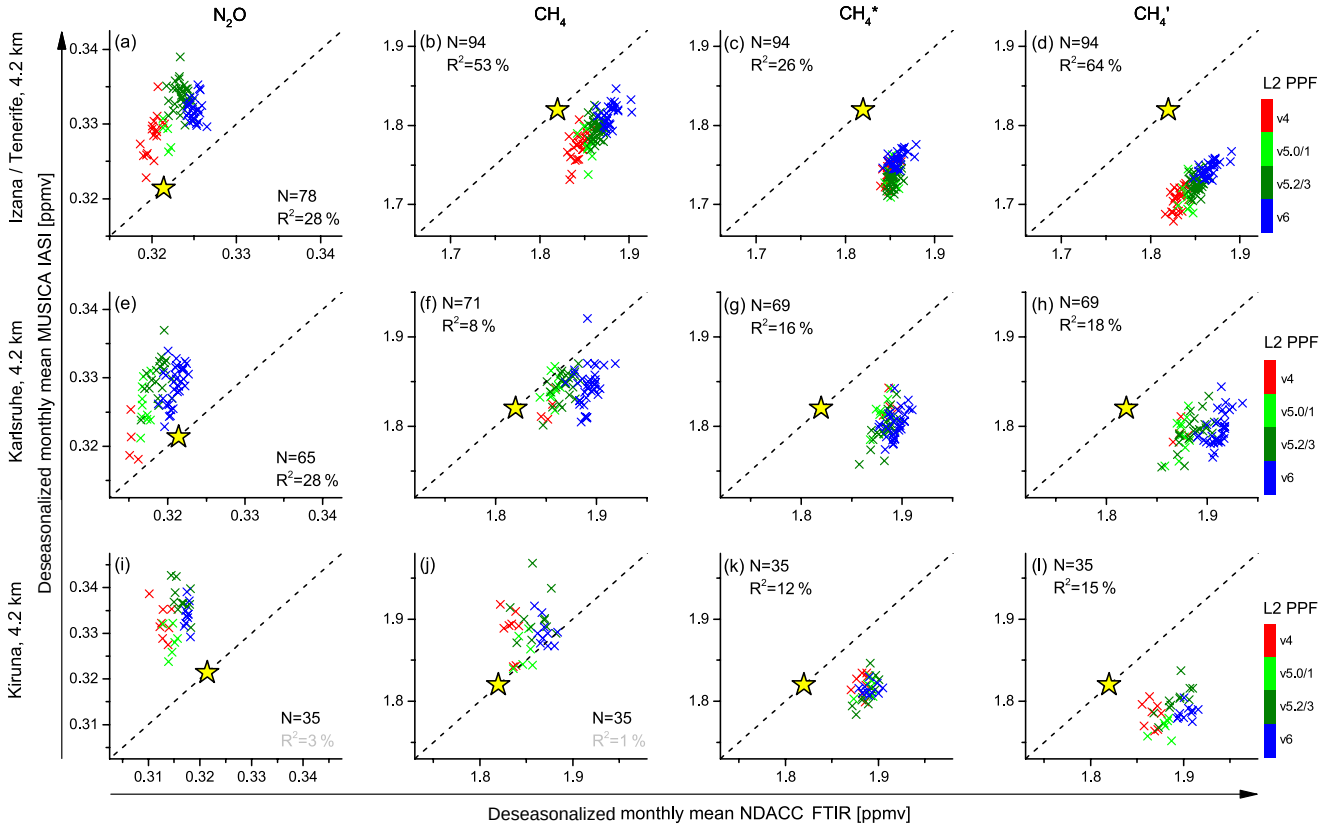

Figure 17. Same as Fig. 16, but for MUSICA IASI products (4.2 km retrieval) and coinciding NDACC FTIR product (4.2 km retrieval): **(a–d)** for the surroundings of Tenerife Island; **(e–h)** for the surroundings of Karlsruhe; **(i–k)** for the surroundings of Kiruna; **(a)**, **(e)** and **(i)** for N_2O; **(b)**, **(f)** and **(j)** for CH_4; **(c)**, **(g)** and **(k)** for CH_4^*; and **(d)**, **(h)** and **(l)** for CH_4'. R^2 values in black indicate significant positive correlations (95 % confidence level) and grey indicate no significance.

(more than 7 years between April 2010 and December 2017). In the N_2O correlation the inconsistency between L2 PPF software v5.2–5.3 and v6 becomes weakly visible. The Karlsruhe R^2 value for CH_4 is 8 %, which is significantly lower than the respective R^2 value for Tenerife. Between 2011–2014 (L2 PPF v5.2–5.3) and 2015–2017 (L2 PPF v6) the deseasonalized Karlsruhe MUSICA IASI CH_4 concentrations keep constant or even slightly decrease, while in the respective NDACC FTIR data they show a clear increase. It seems that the inconsistency between v5.2–5.3 and v6 is observable at Karlsruhe at 4.2 km altitude in the N_2O as well as the CH_4 data. When performing the calculations according to Eq. (11) part of these inconsistencies are cancelled out, which explains why at Karlsruhe we get higher R^2 values for CH_4^* than for CH_4. In Kiruna there is no significant correlation for N_2O and CH_4 and a weak significant correlation for CH_4^*. A similar observation has been made for the seasonal cycle analyses at Kiruna. It seems that we need to calculate a combined product according to Eq. (11), because the uncertainties in the individual N_2O and CH_4 products are too high.

The correlations for the UTLS region are depicted in Fig. 18. At three sites we find significant positive correlations for N_2O and CH_4 and no significance for CH_4^*. The latter means that the variations in the deseasonalized N_2O and CH_4 data are largely in phase, because they are mainly due to the shifts in the tropopause altitudes. As a consequence the calculations according to Eq. (11) cancel out a significant part of the respective signals. For N_2O and CH_4, the correlations would be stronger without the inconsistency between the L2 PPF software v5.2–5.3 and v6. This inconsistency is very clearly observed in the Tenerife and Karlsruhe data and weakly indicated in the Kiruna data.

6.3 Day-to-day signals

In this section we examine the reliability of the MUSICA IASI day-to-day signals ($d(t)$ of Eq. 21). Figure 19 depicts the R^2 values obtained for correlating the MUSICA IASI $d(t)$ data with the $d(t)$ data obtained from the GAW and NDACC FTIR reference data. The R^2 values document to what extend the MUSICA IASI data can capture the same signals as present in the reference data. The higher the R^2

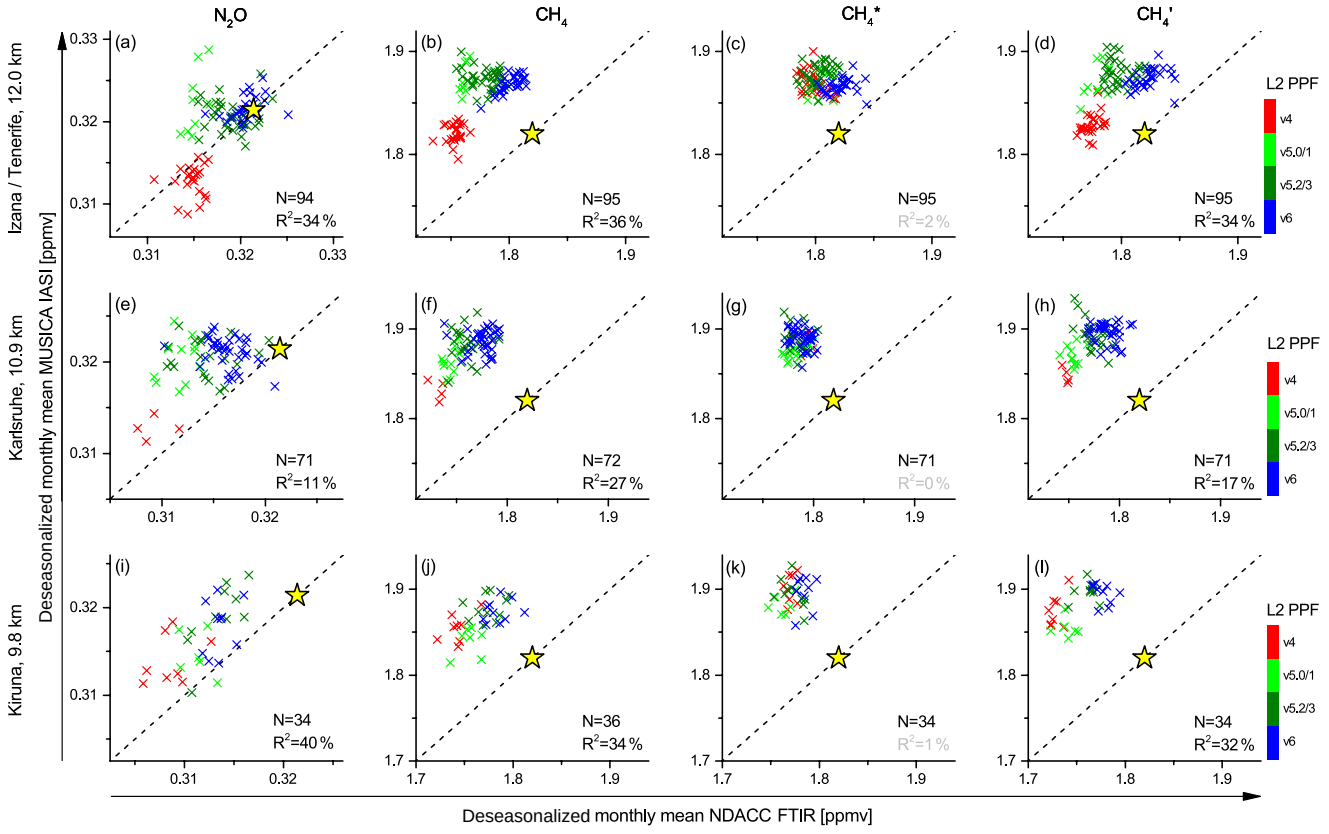

Figure 18. Same as Fig. 17, but for correlations at altitudes representing the UTLS regions.

value the better the MUSICA IASI data can detect the respective signal. The crosses represent the R^2 coefficients for the correlation between MUSICA IASI and GAW data (red for Tenerife and green for Karlsruhe). The circles represent the coefficients for the correlation between MUSICA IASI and NDACC FTIR (red, green and blue for Tenerife, Karlsruhe and Kiruna, respectively). Large symbols indicate significant positive correlations (significance at the 95 % confidence level) and small symbols indicate no significance. For 4.2 km altitude the day-to-day N_2O signals show no significant correlation. For CH_4 there is no significant correlation at Kiruna and weak significant correlations at Tenerife and Karlsruhe (R^2 values between 5 and 8 %). For CH_4^* the R^2 value increases to about 15 % at Tenerife, almost up to 50 % at Karlsruhe (for correlation with NDACC FTIR) and to about 25 % at Kiruna. At 4.2 km we cannot detect N_2O and CH_4 day-to-day signals, but we can detect part of the CH_4^* day-to-day signals. For the UTLS region the situation is the other way round. We find significant correlation with R^2 values above 15 % only for CH_4, while for CH_4^* the correlation is very weak or even not significant. For the UTLS region we also observe significant correlations for N_2O; however, the respective R^2 values are below 12 %.

Highest R^2 values for day-to-day variations at 4.2 km are found for CH_4^* and we investigate the respective correlations in more detail. Figure 20 shows the correlations between the MUSICA IASI and GAW data separately for four different seasons: northern hemispheric winter (December, January and February), northern hemispheric spring (March, April and May), northern hemispheric summer (June, July and August) and northern hemispheric autumn (September, October and November). The day-to-day variations are relatively small. At Tenerife the 1σ scatter in the GAW data is only slightly above 0.7 %. In spring the GAW day-to-day signal is slightly stronger than during the other seasons as indicated by the colour of the data points (the colour indicates the 1σ scatter in the GAW data during the considered season). Spring is also the season when the best agreement between the GAW and MUSICA IASI signals is found (we get an R^2 value of 20 %). At Karlsruhe the day-to-day signal in the GAW data is about 0.85 %, i.e. only weakly stronger than at Tenerife. For Karlsruhe the GAW and MUSICA IASI signals show the best agreement in winter and spring, although the 1σ scatter in the GAW data is similar during all four seasons. An explanation of the better agreement in winter and spring might be that in those seasons the atmosphere is relatively stable and the day-to-day signals as seen in the GAW high-mountain observatory in situ data represent the large-scale variations that take place in the free troposphere well.

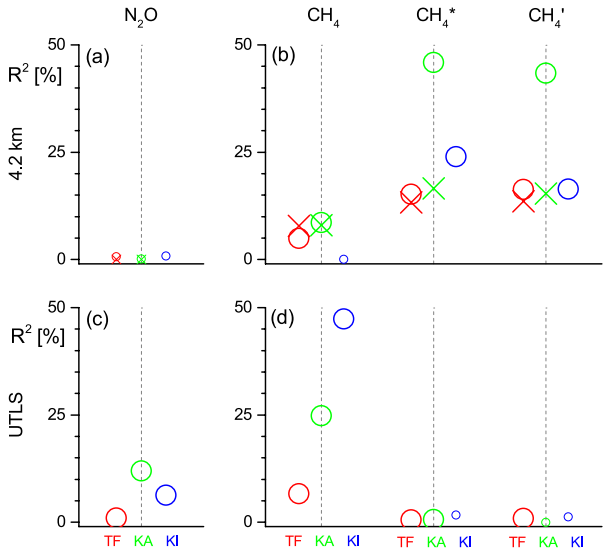

Figure 19. Correlation coefficients R^2 between the MUSICA IASI and reference intra-month day-to-day variations ($d(t)$ of Eq. 21): **(a)** and **(b)** for 4.2 km retrieval altitudes; **(c)** and **(d)** for altitudes representing the UTLS region; **(a)** and **(c)** for N_2O; and **(b)** and **(d)** for CH_4, CH_4^* and CH_4'. A description of the CH_4^* and CH_4' products is given in Table 2. The crosses are for correlations with GAW high-mountain observatory in situ references and the circles for correlations with NDACC FTIR references. Large symbols indicate significant positive correlations (95 % confidence level) and small symbols indicate no significance. Red, green and blue colour for analyses in the surroundings of Tenerife Island (TF), Karlsruhe (KA) and Kiruna (KI), respectively.

Figure 21 presents the correlations of the 4.2 km day-to-day signals between MUSICA IASI and NDACC FTIR. At Tenerife the NDACC FTIR day-to-day 1σ scatter is only 0.3–0.5 %, which is even smaller than the 1σ scatter as observed in the GAW data (the colour of the symbols indicates the 1σ scatter in the NDACC FTIR data during the considered season using the same colour code as in Fig. 20). This reduced signal might be due to the fact that the upward-looking Tenerife FTIR instrument is sensitive to variations that take place in a broad layer above 2400 m a.s.l. The strongest day-to-day signal in the NDACC FTIR data is observed in spring, when the 1σ scatter value is about 0.5 %. Similar to the comparison to GAW data it is the in spring season when the best agreement with the MUSICA IASI is achieved (R^2 value of 21 %). In Karlsruhe the FTIR instrument is located at 110 m a.s.l. It is able to detect a larger part of the free-tropospheric day-to-day signals than the Tenerife instrument. For Karlsruhe the 1σ scatter in the NDACC FTIR day-to-day signals is about 0.5 % in winter, more than 0.8 % in spring and summer and about 0.7 % in autumn. These day-to-day signals are significantly stronger as compared to Tenerife (indicated also by the colours of the respective data points). We find the best agreement between the MUSICA IASI and NDACC FTIR day-to-day signals in spring and summer and the poorest agreement in winter, which is in line with the strengths of the NDACC FTIR day-to-day signals. An explanation of this result can be that in spring and summer the atmosphere is better vertically mixed and large-scale signals have a larger vertical extension than in winter. Because the remote sensing systems are in particular sensitive to signals that occur in broad vertical layers, the spring and summer signals can be better detected than the winter signals. For Kiruna the 1σ scatter in the NDACC FTIR day-to-day signals is stronger in autumn than in spring or summer. And it is late summer and autumn when the best agreement between NDACC FTIR and MUSICA IASI is achieved (presumably due to an atmosphere being vertically better mixed in summer and autumn than in spring). We can conclude that the MUSICA IASI CH_4^* data can capture day-to-day signals corresponding to the 4.2 km retrieval altitude whenever the signals are larger than about 0.6 %.

The correlations between the MUSICA IASI and NDACC FTIR CH_4 day-to-day signal in the UTLS region are shown in Fig. 22. At Tenerife the 1σ scatter in the NDACC FTIR day-to-day signals is below 0.5 %. Only a small part of these weak signals can be detected by the MUSICA IASI data (R^2 values are below 15 %). At Karlsruhe (in winter and spring) and at Kiruna (during all investigated seasons) the 1σ scatter is larger than 1 %. Such day-to-day signals are reasonably detectable in the MUSICA IASI data and we get R^2 values between 23 and almost 60 %. In the UTLS region the CH_4 day-to-day signals are mainly due to variations in the tropopause altitude and important at Kiruna and Karlsruhe (during winter and spring), where the stratosphere is close to the considered altitudes of 9.8 and 10.9 km, respectively. At Tenerife the CH_4 variation is smaller, which might be due to the stratosphere being significantly above the considered altitude of 12 km, a tropopause altitude that is only weakly varying or a relatively weak vertical CH_4 gradient in the lower stratosphere above Tenerife. We can conclude that the MUSICA IASI CH_4 data can capture UTLS day-to-day signals that are larger than 0.8 %.

6.4 Discussion

Because the seasonal cycles in the free troposphere and in the UTLS region are different, their analyses are very useful for investigating the profile characteristics of the MUSICA IASI data. Concerning CH_4 and low latitudes, where we use Tenerife as an example location, the free-tropospheric seasonal cycles of MUSICA IASI, GAW and NDACC FTIR reference data agree well and are different than the seasonal cycles as consistently observed in the UTLS region by the MUSICA IASI and the NDACC FTIR references, demonstrating the profiling capability for CH_4 well. At middle latitudes, where Karlsruhe serves as an example, the MUSICA IASI CH_4 data are sensitive to the seasonal cycle in the UTLS region (good agreement with NDACC FTIR data). However,

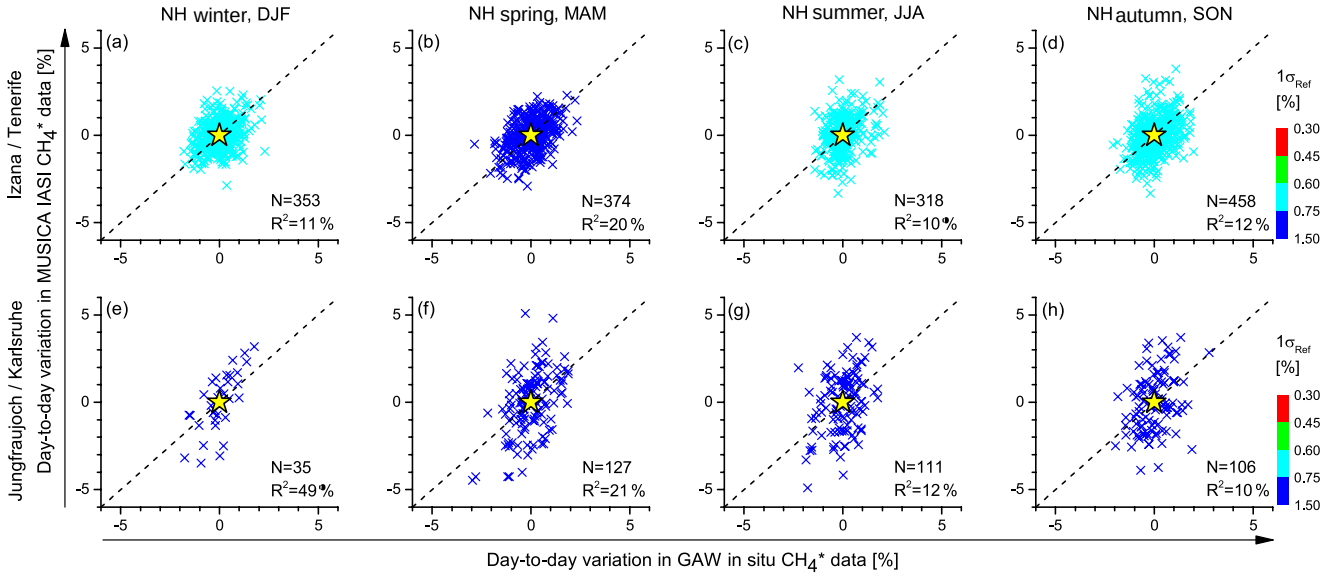

Figure 20. Correlation plots for intra-month day-to-day variations in CH_4^* (MUSICA IASI 4.2 km retrieval products versus GAW high-mountain observatory in situ data): **(a–d)** for the surroundings of Tenerife Island; **(e–h)** for the surroundings of Karlsruhe; **(a)** and **(e)** for northern hemispheric winter; **(b)** and **(f)** for spring; **(c)** and **(g)** for summer; and **(d)** and **(h)** for autumn. The colour code indicates the 1σ scatter in the GAW references ($1\sigma_{Ref}$) during the considered season, the yellow star represents the a priori data used for the retrievals and the black dashed line is the one-to-one diagonal. Number of considered days (N) and R^2 values are given in each panel (all correlations are positive and significant on the 95 % confidence level).

the free-tropospheric seasonal variations cannot be fully resolved, as revealed by the comparison to GAW and NDACC FTIR data. At our high-latitude reference site Kiruna we find good agreement of MUSICA IASI and NDACC FTIR seasonal cycles of CH_4 in the UTLS region, but no agreement in the free troposphere. Concerning N_2O, the MUSICA IASI data do not reproduce the free-tropospheric seasonal variations well as observed in the GAW and NDACC FTIR data. However, the MUSICA IASI product can monitor N_2O in the UTLS region as demonstrated by the reasonable agreement of the respective MUSICA IASI and NDACC FTIR seasonal cycles. In summary, the MUSICA IASI processor provides N_2O and CH_4 data that can detect variations in the UTLS region on a global scale. In addition, it provides useful free-tropospheric CH_4 data for low latitudes and some information on free-tropospheric CH_4 variations in the middle latitudes.

The evaluation of deseasonalized monthly mean data between 2007 and 2017 shows that MUSICA IASI N_2O and CH_4 data are sensitive to long-term changes. However, we find that this capability is strongly affected by changes in EUMETSAT L2 PPF software versions, which affect the EUMETSAT L2 temperatures used as the a priori data for the MUSICA IASI temperature retrievals. We find that the period of L2 PPF software version 5 has a particularly strong impact on the MUSICA IASI N_2O and CH_4 time series, whereby for CH_4 the impact seems to be stronger in the UTLS region than in the free troposphere.

The a posteriori calculation of CH_4^* does remove a lot of seasonal cycle and long-term signals. For the remaining weak seasonal cycles we find generally a poorer agreement between MUSICA IASI, GAW and NDACC FTIR than for CH_4. An exception is the comparison in the free troposphere at the high-latitude site of Kiruna where the MUSICA IASI and NDACC FTIR seasonal cycles differ strongly for CH_4 but agree reasonably well for CH_4^*. Concerning the long-term deseasonalized signals, CH_4^* is less affected than CH_4 data by the L2 PPF software changes. However, CH_4^* contains much less information on real atmospheric long-term changes than CH_4.

When day-to-day variations in the free troposphere are of interest, the CH_4^* product is better than the CH_4 product. The comparison between MUSICA IASI and NDACC FTIR CH_4^* data suggests that the free-tropospheric day-to-day signals are stronger in summer than in winter and might thus be explained by vertical mixing of lower-tropospheric air into the free troposphere. The MUSICA IASI data cannot detect the extremely weak free-tropospheric day-to-day variations of N_2O. In the UTLS region the day-to-day variations of N_2O and CH_4 concentrations are mainly due to vertical shifts in the tropopause altitude and particularly important for higher latitudes and the winter and spring seasons. Upward and downward shifts of the tropopause altitude cause concentration increases and decreases, respectively. The a posteriori calculation of CH_4^* removes a lot of this signal, so day-to-day variations in the UTLS can be detected in the MUSICA IASI

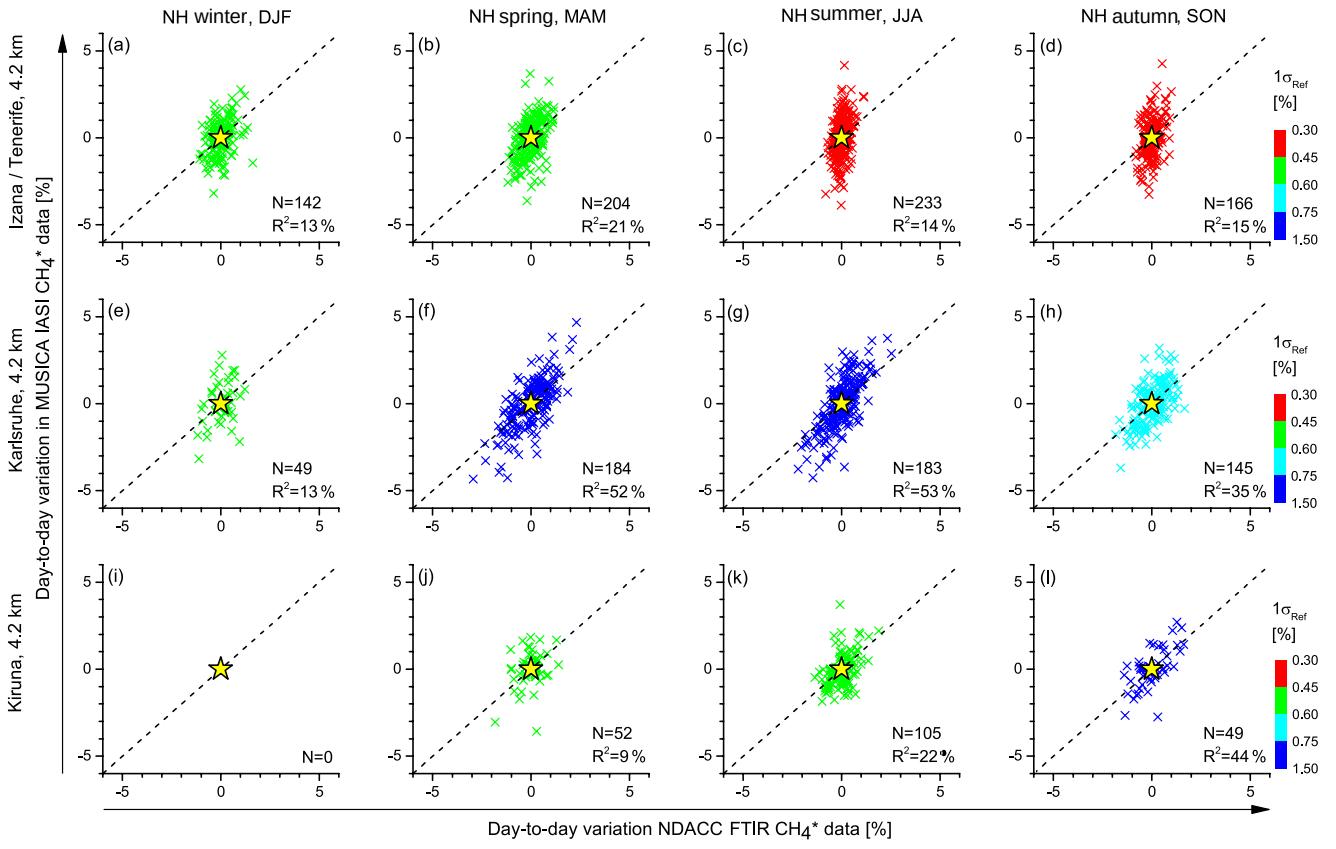

Figure 21. Same as Fig. 20, but for MUSICA IASI products (4.2 km retrieval) and coinciding NDACC FTIR product (4.2 km retrieval): **(a–d)** for the surroundings of Tenerife Island; **(e–h)** for the surroundings of Karlsruhe; **(i–k)** for the surroundings of Kiruna; **(a)**, **(e)** and **(i)** for northern hemispheric winter; **(b)**, **(f)** and **(j)** for spring; **(c)**, **(g)** and **(k)** for summer; and **(d)**, **(h)** and **(l)** for autumn.

N_2O and CH_4 data but not in the CH_4^* data. In this context CH_4^* can be of interest for studies that involve atmospheric models, because it reduces the impact of the uncertainty in the modelled tropopause altitude.

7 CH_4 correction on scales where errors are dominating

In Sect. 2.4 we propose an a posteriori correction of CH_4 that addresses all timescales and all spatial scales. However, the previous section showed that the MUSICA IASI CH_4 seasonal cycles and long-term variations are generally of good agreement (especially when inconsistencies due to changes in EUMETSAT L2 PPF software versions can be avoided). So it is reasonable to exclude these timescales $(s(t)+l(t)$ from Eq. 21) for the CH_4 correction procedure and we propose subtracting only the N_2O logarithmic-scale signal of $\overline{x_m([t_1,t_2])}+d(t)$ from the CH_4 logarithmic-scale data. Because the N_2O day-to-day variations are very weak and can be neglected (apart from variations caused by the day-to-day tropopause shift), the reconstruction of CH_4 needs then no full N_2O model data instead only a reliable N_2O climatology for the $[t_1,t_2]$ reference period. Correcting the $\overline{x_m([t_1,t_2])}$ signals of the MUSICA IASI data using a reliable climatology ensures that the latitudinal inconsistency is corrected (such correction is documented by the comparison between MUSICA IASI and HIPPO data, see Figs. 8 and 9, and by the comparison between MUSICA IASI and NDACC FTIR at three sites representing different latitudinal regions, see Tables 6 and 7). Similar to Eq. (16) we can calculate this corrected product using

$$\hat{\boldsymbol{x}}^{c}_{CH_4}(t) = \hat{\boldsymbol{x}}_{CH_4}(t) - \left(\overline{\hat{\boldsymbol{x}}_{m,N_2O}[t_1,t_2]} + \hat{\boldsymbol{x}}_{d,N_2O}(t)\right) + \mathbf{A}_{N_2O}\left(\overline{\boldsymbol{m}_{N_2O}[t_1,t_2]} - \boldsymbol{x}_{a,N_2O}\right) + \boldsymbol{x}_{a,N_2O}. \quad (22)$$

Here $\overline{\hat{\boldsymbol{x}}_{m,N_2O}[t_1,t_2]}$ is the N_2O distribution obtained for the reference period from the N_2O retrieval product, $\hat{\boldsymbol{x}}_{d,N_2O}(t)$ the day-to-day signal in the N_2O retrieval product and $\overline{\boldsymbol{m}_{N_2O}[t_1,t_2]}$ the modelled N_2O climatology for the reference period $[t_1,t_2]$. In practice we determine the day-to-day signal in the N_2O retrieval product from the time series model as described in Appendix C ($\hat{\boldsymbol{x}}_{d,N_2O}(t) = \hat{\boldsymbol{x}}_{N_2O}(t) - \hat{\boldsymbol{x}}_{m,N_2O}(t)$, where $\hat{\boldsymbol{x}}_{N_2O}(t)$ and $\hat{\boldsymbol{x}}_{m,N_2O}(t)$ is the time series of the retrieval product and the time series obtained by fitting to the

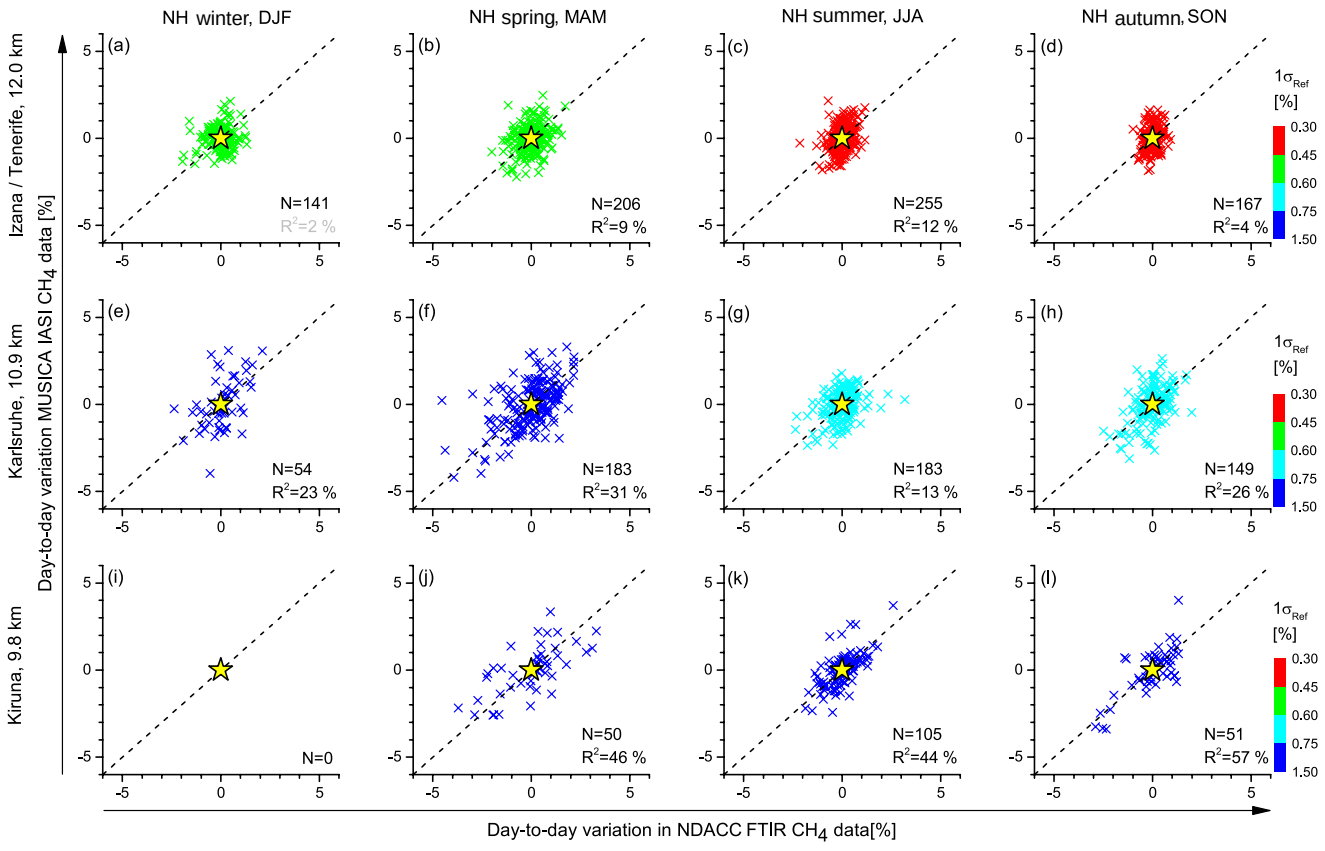

Figure 22. Same as Fig. 21, but for correlations of CH_4 and at altitudes representing the UTLS regions. R^2 values in black indicate significant positive correlations (95 % confidence level) and grey indicate no significance.

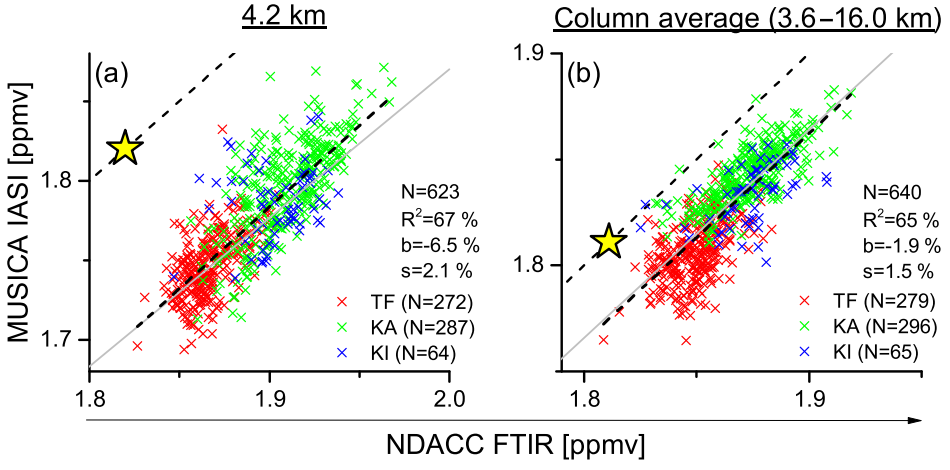

Figure 23. Correlation between daily mean MUSICA IASI and NDACC FTIR CH_4' data for the L2 PPF software v6 period. Shown are the data that are of particular interest for CH_4 cycle research: **(a)** free-tropospheric volume mixing ratios; **(b)** column averages between 3.6 and 16 km. Red, green and blue crosses are for comparisons at Izaña and Tenerife, Karlsruhe and Kiruna, respectively. Each plot gives the number of data (N), the correlation coefficients (R^2), the bias (b), and the scatter (s) of the differences. The thin dashed dark line is the one-to-one diagonal, the grey line the diagonal shifted by the bias value and the thick black dashed line the regression curve obtained from a linear least squares fit on all data points.

time series model, respectively). This proceeding avoids the more sophisticated calculations as described in the context of Eq. (21).

Because we are interested in evaluating the errors in the corrected product that are linked to IASI measurements (and not to uncertainties of N_2O climatologies), we assume $\overline{\boldsymbol{m}_{N_2O}[t_1,t_2]} = \boldsymbol{x}_{a,N_2O}$ and from Eq. (22) we get

$$\hat{\boldsymbol{x}}'_{CH_4}(t) = \hat{\boldsymbol{x}}_{CH_4}(t) - \left(\overline{\hat{\boldsymbol{x}}_{m,N_2O}[t_1,t_2]} + \hat{\boldsymbol{x}}_{d,N_2O}(t)\right) + \boldsymbol{x}_{a,N_2O}. \quad (23)$$

In this paper we use the label CH'_4 for the product that has undergone the a posteriori processing according to Eq. (23) and has subsequently been transferred to the linear scale. In Table 2 it is briefly described in the context of the other CH_4 products used in this paper.

The variation in the CH'_4 product is driven by IASI measurements and not affected by external data (e.g. model simulations), and the evaluation of CH'_4 will reveal the errors in the corrected data that are linked to the IASI measurements. The analytical characterization of the CH'_4 data is done in analogy to the characterization of CH^*_4 (using $\mathbf{A}^{\mathbf{P}}_{\mathbf{11}}$, $\mathbf{\Delta}\hat{\boldsymbol{x}}^{\mathbf{P}}_{\mathbf{1}}$, $\mathbf{S}^{\mathbf{P}}_{\hat{\mathbf{x}},\mathbf{b},\mathbf{11}}$ and $\mathbf{S}^{\mathbf{P}}_{\hat{\mathbf{x}},\mathrm{noise},\mathbf{11}}$ according to Sect. 2.4.2). The comparison of CH'_4 data to references is done in consistency with the evaluation of CH_4 and CH^*_4 as presented in Sects. 5 and 6.

At Tenerife and for the free troposphere the CH'_4 product performs better than the CH_4 and CH^*_4 products: it delivers the highest R^2 values (see Figs. 10 and 11) and the lowest scatter (see Tables 5 and 6). At Karlsruhe and Kiruna we find a better performance for CH^*_4 than for CH'_4, which we think is due to the inconsistencies in the EUMETSAT L2 PPF software versions, which are partly corrected in CH^*_4 but not corrected in CH'_4. The MUSICA IASI versus NDACC FTIR comparisons of CH_4 at the different sites result in different biases. This latitudinal variation of the bias is significantly reduced in the CH'_4 data (see Table 6). This improvement is similar to the CH^*_4 data. For the UTLS CH_4 has higher R^2 values than CH'_4 (see Fig. 12), because in CH'_4 (like in CH^*_4) the day-to-day signals due to varying tropopause altitudes are not considered.

Concerning seasonal cycles, the CH'_4 product shows a similar good agreement with the references as the CH_4 product (see Figs. 13–15), i.e. a better agreement than CH^*_4 (except for the free troposphere above Kiruna).

For the free-tropospheric long-term signals the R^2 values are higher for CH'_4 than for CH_4 (see Figs. 16 and 17). This is an advantage with respect to CH^*_4, where the long-term signals are strongly damped, leading to lower R^2 values. In the UTLS the R^2 values are slightly lower for CH'_4 than for CH_4 (see Fig. 18). The reason is that the signals due to anomalies in the tropopause altitude are partly removed in CH'_4 but fully considered in CH_4. Please note that in the CH^*_4 UTLS data no significant long-term signals are observable, because the respective correction removes all long-term signals, not only signals due to anomalies in the tropopause altitude.

Concerning day-to-day signals, the CH'_4 data have a similar performance compared to the CH^*_4 data (see Fig. 19): free-tropospheric day-to-day signals can be detected reasonably well and the UTLS day-to-day signals are not affected by short-term variations in the tropopause altitude.

The here-presented alternative a posteriori correction method relies on the seasonal cycles and long-term evolution as given in the MUSICA IASI CH_4 retrieval data (which have a demonstrated good quality) and only addresses the spatial and temporal scales that are not reliably represented in the MUSICA IASI CH_4 retrieval data: (1) the latitudinal gradient and (2) the day-to-day timescale signal, which are presumably strongly affected by uncertainties in the EUMETSAT L2 temperatures. Furthermore, the correction reduces the impact of short-timescale atmospheric dynamics (like the short-timescale variability of the tropopause altitude), which is an advantage for model comparison studies (short-timescale and small-spatial-scale dynamics are difficult to capture using global models). With the calculation of the CH'_4 product the simultaneously retrieved CH_4 and N_2O data are optimally exploited and we strongly recommend the usage of CH'_4 instead of CH^*_4.

8 Prospective usage of the CH'_4 product in combination with inverse modelling

The potential of the MUSICA IASI CH'_4 product for investigating the CH_4 cycle on a global scale is revealed by Fig. 23. It displays correlations between NDACC FTIR and MUSICA IASI of free-tropospheric CH'_4 mixing ratios and mixing ratios averaged for the layer between 3.6 and 16 km altitude. The latter are calculated by dividing the layer's amount of CH'_4 by the layer's amount of dry air. Shown are only data for the EUMETSAT L2 PPF software v6 period (the latest software version and presumably the period providing the most reliable atmospheric temperature data). We find a very good agreement between NDACC FTIR and MUSICA IASI data and in particular a good consistency between data from the different sites (Tenerife: low latitudes; Karlsruhe: mid-latitudes; Kiruna: high latitudes). The variations as observed in the CH'_4 data are driven by IASI measurements and independent of external data like model data (all retrievals are done with the same a priori assumption, indicated as a yellow star). This highlights the invaluable contributions that the MUSICA IASI CH'_4 retrieval products can make to inverse modelling in the framework of data assimilation approaches (Bergamaschi et al., 2009, 2013). The assimilation of free-tropospheric data (CH'_4 data shown in the left panel of Fig. 23) will mainly help for constraining CH_4 fluxes between the lower atmosphere and surface at low latitudes (at high latitudes the signal in the 4.2 km retrieval data is dominated by variations that take place in the UTLS, see

Sect. 6). The assimilation of the mixing ratios averaged over the layer between 3.6 and 16 km altitude (CH'_4 data shown in the right panel of Fig. 23) will be in particular useful in combination with total column averaged mixing ratios (Massart et al., 2014, demonstrated that the combined assimilation of GOSAT and IASI data very well constrains the atmospheric CH_4 state).

For a MUSICA IASI CH'_4 data assimilation in practice we recommend the following procedure in each assimilation step:

- Adjust the N_2O and CH_4 retrieval products to the background state of the current assimilation step by adding $\hat{\boldsymbol{x}}_{e,N_2O}$ and $\hat{\boldsymbol{x}}_{e,CH_4}$ (according to Eqs. A1 and A2 with $\boldsymbol{x}_{e,N_2O}$ and $\boldsymbol{x}_{e,CH_4}$ being the background state of N_2O and CH_4, respectively). This ensures that the measurement information of the retrieval product is correctly used for updating the background state.

- Calculate CH'_4 according to Eq. (23) and then add to the CH'_4 data the vector $\hat{\boldsymbol{x}}'_{e,CH_4}$ (according to Eq. A4, with $\overline{\boldsymbol{m}_{N_2O}[t_1,t_2]}$ being a climatology from the model used within the assimilation system). For these calculations it should be kept in mind that, due to the previous adjustment to the background state, $\boldsymbol{x}_{a,N_2O}$ is the N_2O background state of the current assimilation step. These calculations reduce the impact of short-term atmospheric dynamics and the atmospheric temperature errors and correct the latitudinal inconsistencies in agreement with the model used within the assimilation system.

- Remove the bias in the MUSICA IASI CH'_4 data. Figure 23 reveals that this bias is consistent for different locations and seasons. However, the absolute value of the bias cannot be unambiguously determined from the comparison to NDACC FTIR data, because the NDACC FTIR data have their own systematic errors. For an accurate bias determination, further investigation of the NDACC FTIR systematic errors or further comparison studies to data from more recent aircraft campaigns is needed.

- Consider the errors in $\ln[CH_4] - \ln[N_2O]$ as estimated in Sect. 3.3 as proxy for the CH'_4 errors in order to correctly weight the observations in the assimilation procedure. The MUSICA IASI products are made available in the form of netcdf files containing estimates of the atmospheric temperature and measurement noise errors for each individual observation (please recall that atmospheric temperature and measurement noise are the dominating statistical errors, see Fig. 5).

9 Summary and outlook

In this paper we present the N_2O and CH_4 retrieval products as generated by the MUSICA IASI processor and explore possibilities for an a posteriori correction of the retrieved CH_4 by using the co-retrieved N_2O data. All the here-represented original retrieval and a posteriori products are obtained by using single N_2O and CH_4 a priori data (no variation with respect to time or location), thereby ensuring that the observed variations reliably indicate the information provided by the IASI measurement and are not affected by external data like other measurements or model simulations. We extensively evaluate the different products by analytical characterizations (theoretical error estimation and documentation of vertical representativeness) and by comparisons to different reference measurements (HIPPO, GAW and NDACC FTIR) that are of reasonable global representativeness and/or cover the full time period between 2007 and 2017.

9.1 Analytic characterization

All products have good sensitivity between 4 and 10 km at all latitudes. For CH_4 we get DOFS values of 1.8 at low latitudes, which indicates the possibility for detecting free-tropospheric CH_4 variation independently from the variations that take place in the UTLS region. Such profiling capability is weaker at high latitudes where DOFS values of typically 1.4 are reached. The a posteriori-corrected CH_4 products show a similar behaviour, although slightly reduced DOFS values. For N_2O the DOFS values are 1.2 (at high latitudes) and 1.4 (at low latitudes), indicating very limited profiling capability. The total statistical errors for an individual MUSICA IASI N_2O or CH_4 product are estimated to 1.5–3 %. The error assessment identifies atmospheric temperatures and measurement noise as the most important sources of uncertainty, whereby the former is significantly reduced and the latter increased in the a posteriori-corrected CH_4 products. Furthermore, negative errors in the MUSICA N_2O and CH_4 concentrations of about 4 % can be caused by not-well-recognized cirrus clouds, which are reduced to about 2 % for the a posteriori-corrected CH_4 products. The systematic errors due to spectroscopic parameters are estimated to be in the range of 2 % and can increase to 4 % in the a posteriori-corrected CH_4 product.

9.2 Comparison to reference measurements

Assuming high accuracy for the HIPPO aircraft in situ profiles we can use the data for empirically evaluating the MUSICA IASI products. Respective comparisons show bias and scatter values of about 2 % for N_2O and CH_4, which is in very good agreement with the estimated systematic and statistical errors. The latitudinal variation as observed in the HIPPO N_2O data are very small (less than 0.5 %); i.e. the latitudinal variation is significantly weaker than the estimated N_2O error and such small variation cannot be observed in the MUSICA IASI data. For CH_4 the signals are much stronger: HIPPO data show typical CH_4 concentrations at low southern hemispheric and high northern hemispheric latitudes of

1.75 and 1.85 ppmv, respectively, i.e. a difference of more than 5 %. This difference is larger than the estimated MUSICA IASI CH_4 error and the latitudinal CH_4 gradients can be detected in the MUSICA IASI CH_4 product. However, we also find an inconsistency in the MUSICA IASI free-tropospheric CH_4 data between low and high latitudes. In the a posteriori-corrected CH_4 products this inconsistency is almost completely removed.

The NDACC FTIR N_2O and CH_4 remote sensing profiles are also good references for evaluating the MUSICA IASI products. The scatter values between NDACC FTIR and MUSICA IASI data are similar to the scatter values between HIPPO and MUSICA IASI data and thus also in good agreement with the estimated statistical errors. The observed bias is higher than the bias observed with respect to HIPPO. This is expectable because the NDACC FTIR data have their own systematic errors of about 2 %. In agreement with the HIPPO comparison, the NDACC FTIR comparison reveals a significant inconsistency between free-tropospheric MUSICA IASI CH_4 from low and high latitudes, which is significantly reduced in the a posteriori-corrected CH_4 data.

For the time period 2007–2017 the MUSICA IASI data are compared to GAW and NDACC FTIR data and different timescales are investigated. The comparison to GAW is limited to the free troposphere altitude region and the comparison to NDACC FTIR can be performed for the free troposphere region as well as the UTLS region. The comparisons of seasonal cycles of CH_4 clearly confirm the predicted good profiling capability at low latitudes and a weak profiling capability at middle latitudes. For N_2O the comparison confirms that the sensitivity is mainly limited to the UTLS region. The comparisons of deseasonalized monthly mean data reveal the potential of the MUSICA IASI products for investigating atmospheric long-term changes and large-scale anomalies. However, this potential would be much better explored by using EUMETSAT L2 atmospheric temperatures generated by a unique EUMETSAT L2 processing software. The currently available EUMETSAT L2 atmospheric temperatures used in our study are produced by different processing software versions, which has a significant impact on the long-term consistency of the N_2O, CH_4 and a posteriori-corrected CH_4 products. Moreover, the a posteriori-corrected CH_4 product is best sensitive to the seasonal cycles and the long-term behaviour, if these timescales are excluded from the correction procedure. The comparison of day-to-day timescale signals shows good agreement for CH_4 in the UTLS, where the signals are presumably due to day-to-day variations in the tropopause altitude. The N_2O data show a limited sensitivity with respect to these variations. For the free troposphere we find almost no agreement for day-to-day signals in N_2O and CH_4, but a good agreement for the a posteriori-corrected CH_4 products.

9.3 Conclusion on a posteriori correction and outlook

The a posteriori correction removes the dominating errors (inconsistency between low and high latitudes and errors due to uncertainties in atmospheric temperatures) and reduces the impact of the small- and short-scale atmospheric dynamics, which is difficult to capture using atmospheric models. However, if we perform the correction on all scales (a posteriori-corrected product CH_4^*) a significant part of the measurable signals is also removed. For this reason we suggest an alternative correction (a posteriori-corrected product CH_4') that only performs the correction on the spatial and temporal scales where the variations are dominated by errors. This ensures that the errors are reduced without removing the measurable signals (seasonal cycles and long-term behaviour). With the a posteriori calculation of the product CH_4' the simultaneously retrieved CH_4 and N_2O data are optimally exploited and we strongly recommend the usage of CH_4' instead of CH_4^*.

Due to the good global consistency of the MUSICA IASI CH_4' data, their usage in combination with global inverse modelling seems promising. Although, it might be useful to more accurately determine the bias in the MUSICA IASI CH_4' data. Moreover, a current obstacle for a global data assimilation of MUSICA IASI CH_4' data is the limited availability of retrieved data (currently global MUSICA IASI retrievals have only been made for 2 months in 2014). In this context, we plan the following activities. (1) We plan to compare MUSICA IASI CH_4' data to aircraft profile data from ATom (Atmospheric Tomography Mission, https://espo.nasa.gov/atom/, last access: 11 July 2018). Because the ATom measurements have been made between summer 2016 and spring 2018, they exclusively cover the EUMETSAT L2 PPF software v6 period, thus offering the possibility to more accurately determine the bias in the CH_4' data retrieved by using EUMETSAT L2 PPF software v6 atmospheric temperature data as a priori temperatures (v6 is the latest software version and presumably provides the most reliable atmospheric temperature data). (2) We plan to perform a large number of MUSICA IASI retrievals on a global scale. The focus of these retrieval activities will be on the time period where EUMETSAT L2 PPF software v6 atmospheric temperature data are available (October 2014 onward).

Data availability. The MUSICA IASI data are available at http://www.imk-asf.kit.edu/english/2746.php (Schneider, 2018) and by request to the corresponding authors. The HIPPO data are available at http://hippo.ucar.edu/ (last access: 11 July 2018) and the GAW data at http://ds.data.jma.go.jp/ (last access: 11 July 2018). The NDACC FTIR data are available at ftp://ftp.cpc.ncep.noaa.gov/ (last access: 11 July 2018) and by request to the corresponding authors.

Appendix A: A posteriori insertion of external data

An optimal estimation remote sensing retrieval updates the a priori knowledge by using the information as given in the measurement (e.g. the measured IASI spectra). The retrieval product depends on the measurement and the used a priori (or background) data. The MUSICA IASI processor uses single a priori profiles for all retrievals (the a priori data are the same for different seasons and locations). This ensures that the variation as seen in the retrieval product is an exclusive consequence of the measurements made by the remote sensing instrument. Often retrievals are done with varying a priori information; however, then the variation given by the retrieval product is not an exclusive consequence of the measurement, but instead it depends on the measurement as well as the a priori data.

Our retrieval product can be adjusted a posteriori for varying a priori data. According to Rodgers and Connor (2003) we can calculate a posteriori the remote sensing retrieval product that would have resulted by using the varying a priori data $\boldsymbol{x}_\mathrm{e}$ (externally generated data like model output or other measurements) instead of our single a priori $\boldsymbol{x}_\mathrm{a}$ by adding $\hat{\boldsymbol{x}}_\mathrm{e}$ to the original retrieval product, whereby the vector $\hat{\boldsymbol{x}}_\mathrm{e}$ (for N_2O and CH_4, respectively) is calculated by

$$\hat{\boldsymbol{x}}_{\mathrm{e,N_2O}} = (\mathbf{A}_{\mathrm{N_2O}} - \mathbb{I})(\boldsymbol{x}_{\mathrm{a,N_2O}} - \boldsymbol{x}_{\mathrm{e,N_2O}}), \tag{A1}$$

and

$$\hat{\boldsymbol{x}}_{\mathrm{e,CH_4}} = (\mathbf{A}_{\mathrm{CH_4}} - \mathbb{I})(\boldsymbol{x}_{\mathrm{a,CH_4}} - \boldsymbol{x}_{\mathrm{e,CH_4}}). \tag{A2}$$

Here $\mathbf{A}_{\mathrm{N_2O}}$, $\mathbf{A}_{\mathrm{CH_4}}$ and $\mathbb{I}$ are the averaging kernel matrices of N_2O, CH_4 and the identity matrix, respectively.

In Sects. 2.4.3 and 7 we discuss methods for correcting CH_4 by means of co-retrieved N_2O data and N_2O model simulations. For evaluating the measurement-related uncertainties in the corrected CH_4 data we define the modelled N_2O profile as $\boldsymbol{m}_{\mathrm{N_2O}} = \boldsymbol{x}_{\mathrm{a,N_2O}}$ and work with the products $\mathrm{CH_4^*}$ and $\mathrm{CH_4'}$. The variability as seen in the products $\mathrm{CH_4^*}$ and $\mathrm{CH_4'}$ is an exclusive consequence of the measurements made by the remote sensing instrument (it is not affected by the model). Similarly to Eqs. (A1) and (A2) we can insert model data a posteriori, thereby adjusting the products to realistic assumption for $\boldsymbol{m}_{\mathrm{N_2O}}$. We define

$$\hat{\boldsymbol{x}}^*_{\mathrm{e,CH_4}} = -\mathbf{A}_{\mathrm{N_2O}}(\boldsymbol{x}_{\mathrm{a,N_2O}} - \boldsymbol{m}_{\mathrm{N_2O}}), \tag{A3}$$

and

$$\hat{\boldsymbol{x}}'_{\mathrm{e,CH_4}} = -\mathbf{A}_{\mathrm{N_2O}}(\boldsymbol{x}_{\mathrm{a,N_2O}} - \overline{\boldsymbol{m}_{\mathrm{N_2O}}[t_1, t_2]}). \tag{A4}$$

Adding $\hat{\boldsymbol{x}}^*_{\mathrm{e,CH_4}}$ to $\hat{\boldsymbol{x}}^*_{\mathrm{CH_4}}$ from Eq. (17) gives the corrected CH_4 product according to Eq. (16) and adding $\hat{\boldsymbol{x}}'_{\mathrm{e,CH_4}}$ to $\hat{\boldsymbol{x}}'_{\mathrm{CH_4}}$ from Eq. (23) gives the corrected CH_4 product according to Eq. (22).

Appendix B: Geographical coverage

Section 4 demonstrates that the MUSICA IASI CH_4 and CH_4^* products capture geographical variations well. Here we show examples of the global geographical distribution as seen in the MUSICA IASI data. We present the situation for two different altitudes and seasons. For each altitude we require that the MUSICA IASI data pass the sensitivity filter (c_{sen} calculated according to Eq. 18 must be smaller than 50 %) and then make $2° \times 2°$ averages for all the data points measured during six days in the northern hemispheric winter (12–17 February 2014) and northern hemispheric summer (12–17 August 2014).

Figure B1 shows the geographical distributions for the retrieval altitude of 4.2 km. These products are representative for the atmosphere between 2 and 8 km (see typical averaging kernels of Fig. 2). Concerning CH_4 we observe the highest concentrations north of 45° N. In August the northern hemispheric atmosphere between 2 and 8 km generally forms part of the well-mixed troposphere; i.e. Fig. B1b documents the latitudinal gradient of tropospheric CH_4 between the tropics and high northern latitudes. In February (Fig. B1a) there is also a gradient in the Northern Hemisphere; however, it is less pronounced if compared to August. The reason is that in February the atmosphere between 2 and 8 km of the middle and high northern latitudes can be affected by the stratosphere, where CH_4 starts to decrease. The varying stratospheric contribution also explains why the lower-tropospheric seasonal cycle of CH_4; i.e. the minimum of CH_4 concentration in July–August and maximum in December–January, is not observable in the middle and high latitudes. However, this cycle is observable at lower latitudes as clearly demonstrated in Sect. 6.

Section 3.3 theoretically predicts smaller errors for free-tropospheric CH_4^* than for CH_4. This is confirmed by the comparison to the different references, revealing smaller scatter values for CH_4^* than for CH_4 (see Tables 4, 5 and 6). Furthermore, in the free troposphere the bias in CH_4^* has a much weaker latitudinal dependency than the bias in CH_4 (see Fig. 9 and Table 6), and day-to-day variations can be detected in the CH_4^* data, but not in the CH_4 data. In summary, in the free troposphere the CH_4^* product is more reliable than the CH_4 product. Figure B1c and d show the free-tropospheric CH_4^* distribution for February and August, respectively. Generally we observe smoother signals. For instance, extremes as seen in the CH_4 maps – such as the very local high concentrations in South America (in February and August), the spot with high concentrations in the ocean south of Africa (in August), the low concentrations in South Africa (in February and August) or the strong west-to-east gradients in the area between the USA and Mexico – almost disappear in the CH_4^* maps. In August and over Asia at around 60° E we observe different latitudinal gradients in CH_4 and CH_4^*. While CH_4 concentrations are almost continuously increasing from south to north, CH_4^* is higher over Iran, Pakistan and Kazakhstan than further north over Russia.

Figure B2 shows the geographical distributions for the retrieval altitude of 10.9 km, which is representative for the atmosphere between 7 and 13 km. In this UTLS region the CH_4 signals mainly depend on the location of the tropopause altitude. If it is high, high tropospheric CH_4 concentrations are measured. If it is low, low stratospheric CH_4 concentrations are detected. The good sensitivity of the MUSICA IASI CH_4 data for capturing these signals is demonstrated in Sect. 6. The variations in the tropopause altitude explain the main differences between summer and winter hemispheres as observed in Fig. B2a and b.

For CH_4^* the distribution maps as depicted in Fig. B2c and d are smoother than for CH_4, because in CH_4^* the tropopause altitude signal is strongly reduced (see discussion in the context of Figs. 15 and 19). As a consequence the latitudinal gradient is weaker in CH_4^* than in CH_4. The local spots with high CH_4 concentrations in the tropics are very interesting. These spots disappear in the CH_4^* maps; i.e. they are very likely due to tropopause dynamics and they might point to events where tropospheric air is injected into the stratosphere.

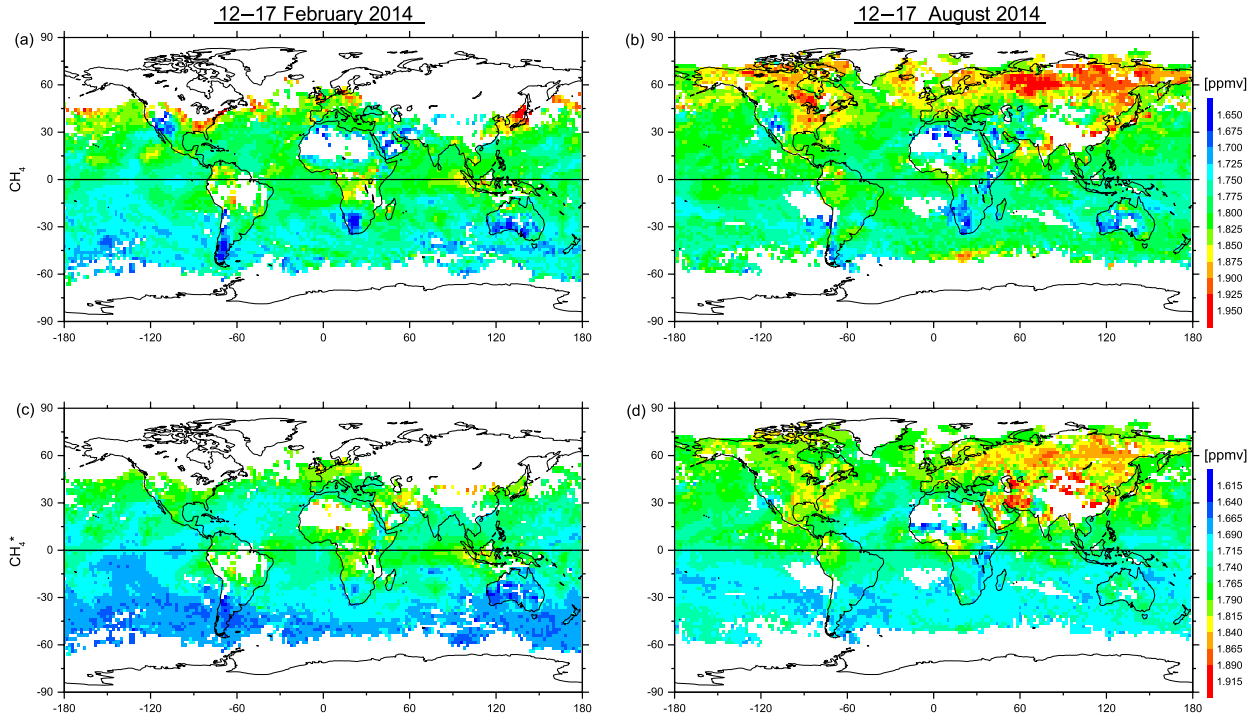

Figure B1. Free-tropospheric MUSICA IASI product retrieved at 4.2 km altitude, filtered for $c_{sen} < 0.5$ (according to Sect. 3.2) and averaged for an latitude × longitude area of 2° × 2°. **(a)** and **(b)** for CH_4; **(c)** and **(d)** for CH_4^*. The maps are shown separately for mid-February 2014 (**a** and **c**) and mid-August 2014 (**b** and **d**).

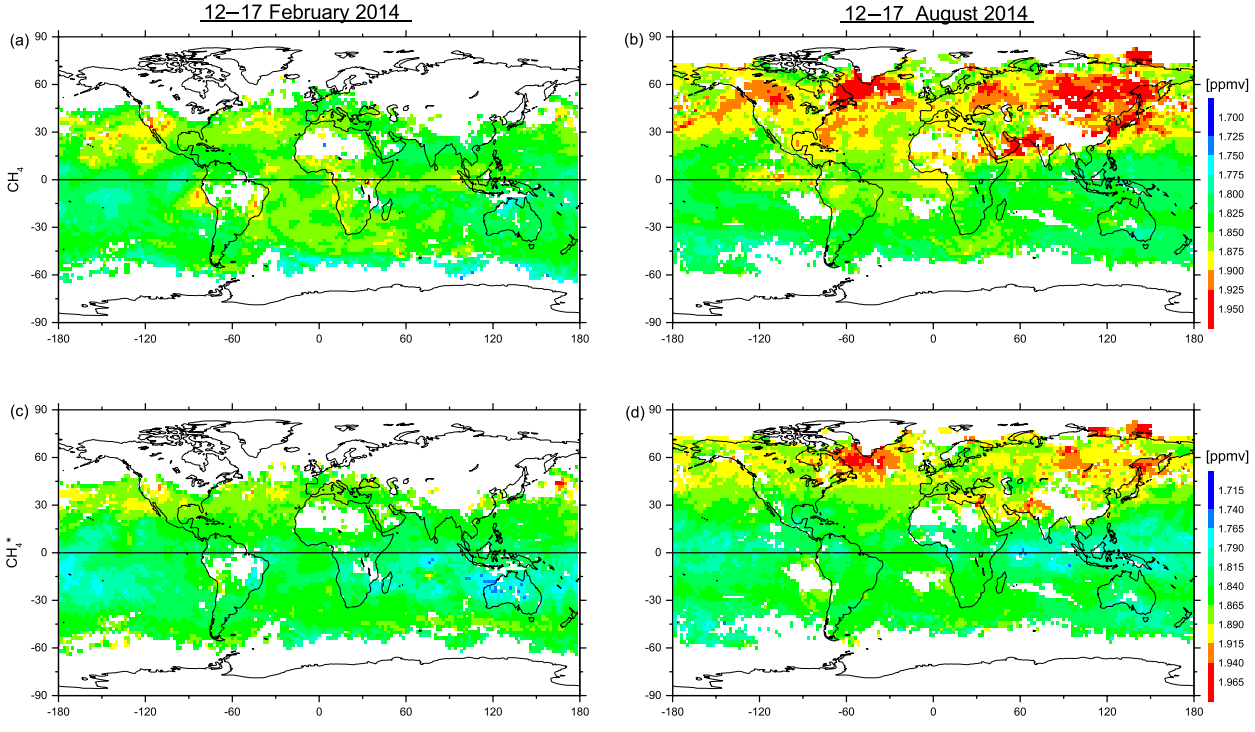

Figure B2. Same as Fig. B1, but for the 10.9 km retrieval altitude.

Appendix C: Continuous data coverage, time series model and long-term data consistency

In Sect. 6 time series of MUSICA IASI and reference data are analysed and respective seasonal cycles, long-term signals and day-to-day variations are compared. Figure C1 shows as an example the MUSICA IASI time series of daily mean data for the surroundings of Tenerife. Figure C1a and b show the time series for the CH_4 and CH_4^* products and the 4.2 km retrieval altitude, and Fig. C1c and d for the 12 km retrieval altitude, respectively. The data represent the area between 15.8 and 17.2° W and 27.2 and 28.4° N and have been generated from spectra measured between 23 November 2007 and 10 December 2017. We only perform retrievals for cloud-free pixels and, after applying the filter with respect to measurement noise and retrieval quality (residual-to-signal ratio in the fitted spectral window must be smaller than 0.004) and the sensitivity filter (c_{sen} calculated according to Eq. 18 must be smaller than 50 %), we have valid MUSICA IASI data on almost 2900 individual days. This example documents the very continuous data coverage that can be achieved by the retrieval of IASI spectra.

In Sect. 6 we use a time series model for estimating the mean values for a reference period and for a first-guess separation of seasonal cycle and long-term signals. The modelled time series is obtained by a multi-regression fit of different coefficients that consider variations on different timescales:

$$x_m(t) = \overline{x_m([t_1,t_2])} + A_0 + A_1 t \quad \text{(C1)}$$
$$+ \sum_{1 \le i \le \frac{\Delta t}{2a}} \left\{ A_{\sin,i} \sin\left(\frac{2\pi i}{\Delta t} t\right) + A_{\cos,i} \cos\left(\frac{2\pi i}{\Delta t} t\right) \right\}$$
$$+ \sum_{1 \le i \le \frac{\Delta j}{a/4}} \left\{ B_{\sin,i} \sin\left(\frac{2\pi i}{\Delta j} j(t)\right) + B_{\cos,i} \cos\left(\frac{2\pi i}{\Delta j} j(t)\right) \right\}.$$

The value $\overline{x_m([t_1,t_2])}$ defines the reference point with respect to which the variations take place. It is the model mean for the reference period $[t_1,t_2]$. By fitting the coefficients A_i, the long-term variations with respect to the reference period $[t_1,t_2]$ are determined. The coefficients A_0 and A_1 capture the linear changes and the coefficients $A_{\sin,i}$ and $A_{\cos,i}$ the amplitude and phases of a Fourier series that considers all frequencies between $1/\Delta t$ and $1/(2a)$. Here a stands for 1 year and $\Delta t = \max\{t\} - \min\{t\}$ is the time period covered by the whole time series. The coefficients $B_{\sin,i}$ and $B_{\cos,i}$ capture the intra-annual variation (season cycle) by fitting amplitude and phases of a Fourier series that considers all frequencies between $1/\Delta j$ and $4/a$. Here $\Delta j = \max\{j(t)\} - \min\{j(t)\}$ is the intra-annual Julian day period covered by the data and $j(t)$ the intra-annual Julian day (intra-annual Julian day means Julian day starting each year with 0; i.e $j(t)$ is between 0 and 366).

The thick black line in Fig. C1 shows the estimated model time series, i.e. the $\hat{\boldsymbol{x}}_m(t)$ data due to the multi-regression fit the coefficients A_i, $A_{\sin,i}$, $A_{\cos,i}$, $B_{\sin,i}$, $B_{\cos,i}$ as described in Eq. (C1). The blue line represents the long-term signals, which are all signals except the seasonal cycle signals; i.e. it is the time series reconstructed according to Eq. (C1), but with the coefficients $B_{\sin,i}$ and $B_{\cos,i}$ set to zero. In the CH_4 data (Fig. C1a and c) the model identifies clear seasonal cycle signals and a long-term increase. The seasonal cycle signals are much weaker in the CH_4^* data (Fig. C1b and d), where in addition no clear long-term increase is observed. The CH_4^* evolution is much smoother than the CH_4 evolution, because the calculation according to Eq. (11) removes a lot of real atmospheric signals, e.g. most of the seasonal cycle signal and the long-term signals (see discussions in Sect. 6).

The MUSICA IASI retrieval processor uses the EUMETSAT level 2 atmospheric temperature as the a priori temperature. Changes in the L2 PPF software that affect the EUMETSAT level 2 atmospheric temperatures can thus also affect the MUSICA IASI data. Dates and details of respective L2 PPF software changes are listed in Table 1. In addition, these dates are marked as magenta lines and arrows at the top of each panel in Fig. C1. Concerning the example time series, the strongest impact of these software changes is observed for CH_4 at 12 km retrieval altitude (Fig. C1c). There is a clear inconsistency between L2 PPF software v4 and v5.0–5.1. These inconsistencies have a strong impact on the long-term signals, which is discussed in Sect. 6. Because the software changes similarly impact N_2O and CH_4, they partly cancel out in the combined product and are thus much more difficult to observe in CH_4^*. Nevertheless, the change from L2 PPF software v5.2–5.3 to v6 can be clearly observed as an inconsistency in CH_4^* time series for 4.2 km retrieval altitude.

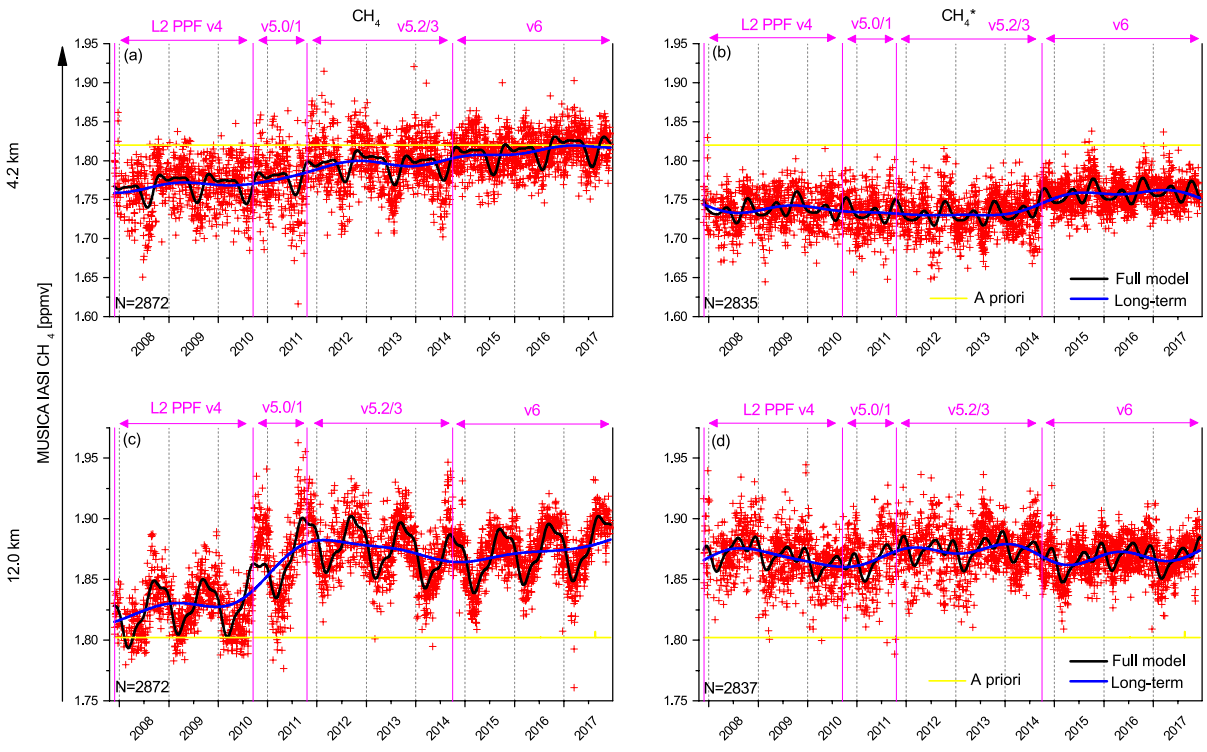

Figure C1. Example of continuous time series of MUSICA IASI daily mean data (red crosses) retrieved in the surroundings of Tenerife Island between 2007 and 2017: **(a)** and **(b)** for 4.2 km altitude; **(c)** and **(d)** for 12 km altitude; **(a)** and **(c)** for CH_4; and **(b)** and **(d)** for CH_4^*. The yellow line is the a priori data used. The results of the multi-regression fit of the time series model are depicted as the black line and the time series model components describing the long-term behaviour are represented by the blue line. The periods with different EUMETSAT L2 PPF software versions that can affect the MUSICA IASI products are indicated by magenta colour.

Appendix D: Comparison of MUSICA IASI and NDACC FTIR remote sensing data

In order to ensure an adequate comparison of the MUSICA IASI and NDACC FTIR remote sensing data we follow the recommendations of Rodgers and Connor (2003). We take care that both data sets use the same a priori information. We use the unique MUSICA IASI a priori data (no variation in space and time) and adjust the NDACC FTIR data to this new a priori profile by adding $(\mathbf{A}_{\mathrm{FTIR}} - \mathbb{I})(\boldsymbol{x}_{\mathrm{a}} - \boldsymbol{x}_{\mathrm{a,FTIR}})$ to the NDACC FTIR retrieval results (with $\mathbf{A}_{\mathrm{FTIR}}$ and $\boldsymbol{x}_{\mathrm{a,FTIR}}$ being the averaging kernels and a priori state corresponding to the NDACC FTIR retrieval, respectively).

We investigate the effect of the different MUSICA IASI and NDACC FTIR averaging kernels. For this purpose we need MUSICA IASI and NDACC FTIR averaging kernels on the same vertical altitude gridding. We chose the vertical griding of the MUSICA IASI retrieval. The transference of the NDACC FTIR averaging kernels on this gridding is achieved via an eigenvector decomposition of $\mathbf{A}_{\mathrm{FTIR}}$:

$$\mathbf{A}_{\mathrm{FTIR}} = \mathbf{V}_{\mathrm{FTIR}} \mathbf{D}_{\mathrm{FTIR}} {\mathbf{V}_{\mathrm{FTIR}}}^{-1}. \quad \text{(D1)}$$

Here the columns of matrix $\mathbf{V}_{\mathrm{FTIR}}$ are the eigenvectors and $\mathbf{D}_{\mathrm{FTIR}}$ is a diagonal matrix with the eigenvalues. We filter out only the eigenvectors with eigenvalues of at least 0.025, interpolate these eigenvectors to the MUSICA IASI gridding and then calculate the regridded NDACC FTIR averaging kernel by $\mathbf{V}'_{\mathrm{FTIR}} \mathbf{D}_{\mathrm{FTIR}} {\mathbf{V}'_{\mathrm{FTIR}}}^{-1}$ (with $\mathbf{V}'_{\mathrm{FTIR}}$ being the interpolated eigenvectors).

The averaging kernel effects when comparing atmospheric signals that are characterized by the covariance matrix $\mathbf{C}$ can be estimated by

$$\mathbf{C}_{\mathrm{cmp}} = (\mathbf{A} - \mathbf{A}_{\mathrm{FTIR}}) \mathbf{C} (\mathbf{A} - \mathbf{A}_{\mathrm{FTIR}})^T. \quad \text{(D2)}$$

Here we use the same covariance matrix as in the context of Eq. (18), because such covariances are theoretically detectable in the MUSICA IASI data, whenever the $c_{\mathrm{sen}} < 0.5$ criterium according to Sect. 3.2 is fulfilled.

The DOFS values of the NDACC FTIR N_2O and CH_4 retrievals are generally between 2.5 and 3.5; i.e. the NDACC FTIR data have a better sensitivity and a better vertical resolution than the MUSICA IASI data. Under this circumstance it might be useful to apply the MUSICA IASI averaging kernels to the NDACC FTIR averaging kernels and then compare the two data products, i.e. treat the NDACC FTIR data with the smoothing function as given by the MUSICA IASI averaging kernel similarly to the data treatment as described for the HIPPO profile data (see Sect. 4 and Eq. 20). Then the averaging kernel effects for the comparison between NDACC FTIR and MUSICA IASI data can be estimated by

$$\mathbf{C}_{\mathrm{cmp,sm}} = (\mathbf{A} - \mathbf{A}\mathbf{A}_{\mathrm{FTIR}}) \mathbf{C} (\mathbf{A} - \mathbf{A}\mathbf{A}_{\mathrm{FTIR}})^T. \quad \text{(D3)}$$

Figure D1 shows correlation plots between c_{cmp} and $c_{\mathrm{cmp,sm}}$ (the diagonal elements of the matrices $\mathbf{C}_{\mathrm{cmp}}$ and $\mathbf{C}_{\mathrm{cmp,sm}}$, respectively) obtained for the retrieval altitude of 4.2 km for the N_2O, CH_4 and CH_4^* product at the three NDACC FTIR stations. Shown are only the coincidences for which the MUSICA IASI data fulfill the $c_{\mathrm{sen}} < 0.5$ criterium according to Sect. 3.2. The c_{cmp} values are mostly larger than the $c_{\mathrm{cmp,sm}}$ values, suggesting that at the 4.2 km retrieval altitude we should compare the MUSICA IASI data with NDACC FTIR data that have been smoothed by the MUSICA IASI averaging kernel.

Figure D2 shows the correlation between c_{cmp} and $c_{\mathrm{cmp,sm}}$ for the retrievals in the UTLS region and for all coincidences where the MUSICA IASI data fulfill the $c_{\mathrm{sen}} < 0.5$ criterium according to Sect. 3.2. For N_2O the c_{cmp} values are still mostly larger than the $c_{\mathrm{cmp,sm}}$ values; however, for CH_4 and CH_4^* it is the other way round. We can conclude that for an optimal comparison of data in the UTLS region we should smooth the NDACC FTIR N_2O data, but there is no need to smooth the CH_4 of CH_4^* data. Such smoothing might even be counterproductive and reduce the comparability of the MUSICA IASI and NDACC FTIR data set.

In line with these findings we compare MUSICA IASI N_2O data with smoothed NDACC FTIR data at all altitudes (free troposphere and UTLS region). The free-tropospheric MUSICA IASI CH_4 and CH_4^* data are also compared to smoothed NDACC FTIR data. However, in the UTLS region the MUSICA IASI and NDACC FTIR CH_4 and CH_4^* data are directly compared (no prior smoothing of the NDACC FTIR data).

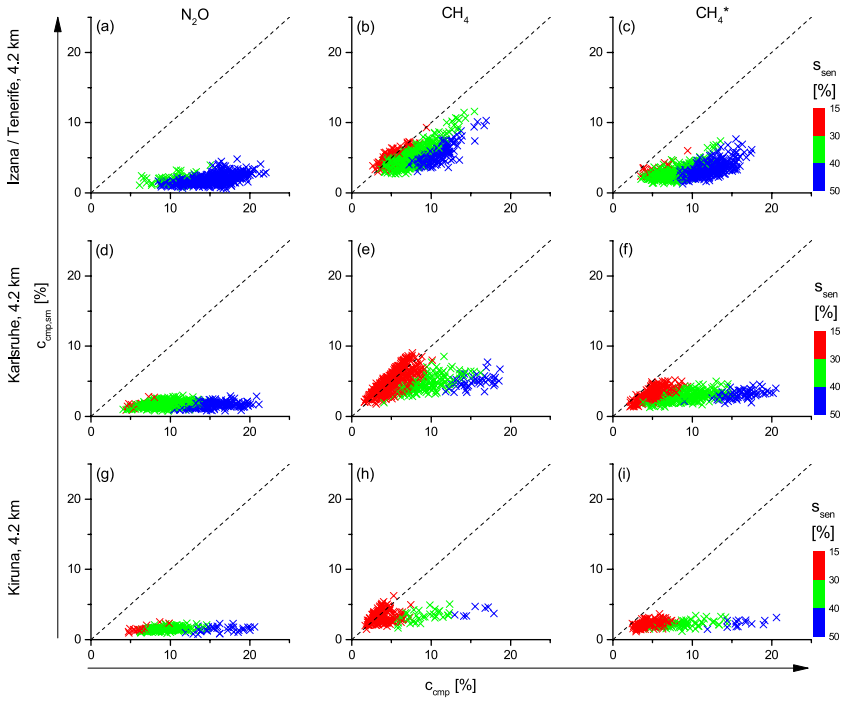

Figure D1. Comparability of MUSICA IASI and NDACC FTIR remote sensing data at 4.2 km. Shown are correlations between the c_{cmp} and $c_{cmp,sm}$ values calculated according to Eqs. (D2) and (D3), respectively: **(a–c)** for the surroundings of Tenerife Island; **(d–f)** for the surroundings of Karlsruhe; **(g–i)** for the surroundings of Kiruna; **(a)**, **(d)** and **(g)** for N_2O; **(b)**, **(e)** and **(h)** for CH_4; and **(c)**, **(f)** and **(i)** for CH_4^*. The colour code shows the MUSICA IASI c_{sen} values according to Sect. 3.2.

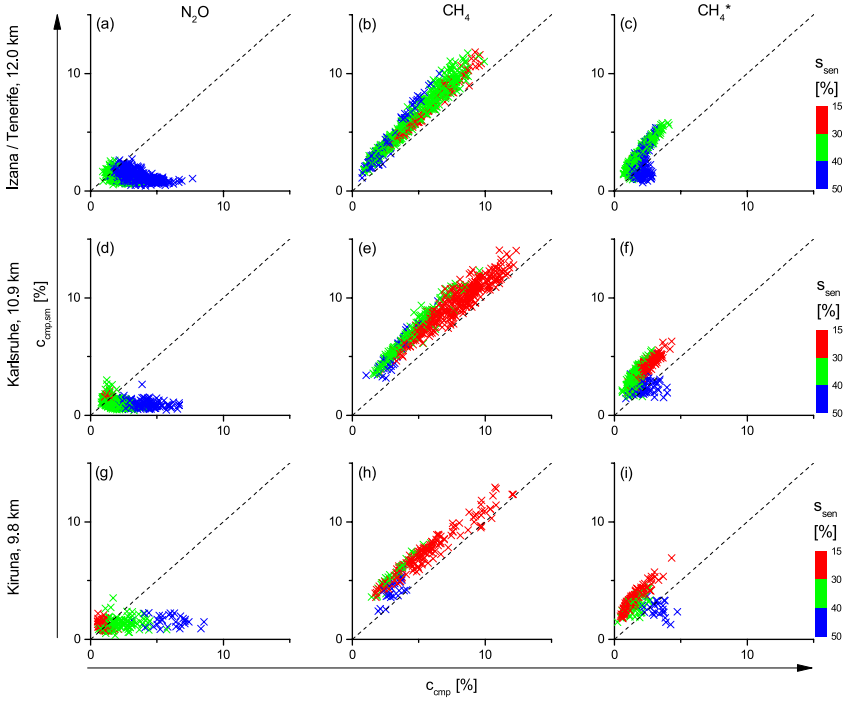

Figure D2. Same as Fig. D1 but for remote sensing data representing UTLS altitude regions.

Author contributions. The manuscript was prepared by OEG and MS with contributions from all co-authors. FH developed the PROFFIT-nadir retrieval code and MS set up the MUSICA IASI retrieval. MS and CB performed the analytic error estimation activities with support from OEG, BE, ES, AW, CB, and FH. OEG, MS and BE performed the MUSICA IASI retrievals for the coincidences with the HIPPO, GAW and NDACC FTIR observations. OEG and MS performed the comparative studies (MUSICA IASI versus HIPPO, WMO–GAW and NDACC FTIR). BE, CD, AW and MS performed the global MUSICA IASI retrievals. OEG, MS, ES, FH, SB, TB and UR supported the NDACC FTIR activities. AGP, MS and LR managed the ground-level in situ experiments and elaborated on the WMO–GAW data.

Competing interests. The authors declare that they have no conflict of interest.

Acknowledgements. This work has strongly benefited from funding by the European Research Council under FP7/(2007–2013)/ERC grant agreement no. 256961 (project MUSICA); by the Deutsche Forschungsgemeinschaft for the project MOTIV (Geschäftszeichen SCHN 1126/2-1); by the Ministerio de Economía y Competitividad from Spain trough the projects CGL2012-37505 (project NOVIA) and CGL2016-80688-P (project INMENSE); by the Ministerio de Educación, Cultura y Deporte (programa "José Castillejo", CAS14/00282); and by EUMETSAT under its Fellowship Programme (project VALIASI). Furthermore, we would like to acknowledge the National Science Foundation (NSF) and the National Oceanic and Atmospheric Administration (NOAA), which supported the collection of the original HIPPO data.

Edited by: Helen Worden
Reviewed by: four anonymous referees

References

Alvarado, M. J., Payne, V. H., Cady-Pereira, K. E., Hegarty, J. D., Kulawik, S. S., Wecht, K. J., Worden, J. R., Pittman, J. V., and Wofsy, S. C.: Impacts of updated spectroscopy on thermal infrared retrievals of methane evaluated with HIPPO data, Atmos. Meas. Tech., 8, 965–985, https://doi.org/10.5194/amt-8-965-2015, 2015.

Angelbratt, J., Mellqvist, J., Blumenstock, T., Borsdorff, T., Brohede, S., Duchatelet, P., Forster, F., Hase, F., Mahieu, E., Murtagh, D., Petersen, A. K., Schneider, M., Sussmann, R., and Urban, J.: A new method to detect long term trends of methane (CH_4) and nitrous oxide (N_2O) total columns measured within the NDACC ground-based high resolution solar FTIR network, Atmos. Chem. Phys., 11, 6167–6183, https://doi.org/10.5194/acp-11-6167-2011, 2011.

August, T., Klaes, D., Schlüssel, P., Hultberg, T., Crapeau, M., Arriaga, A., O'Carroll, A., Coppens, D., Munro, R., and Calbet, X.: IASI on Metop-A: Operational Level 2 retrievals after five years in orbit, J. Quant. Spectrosc. Ra., 113, 1340–1371, https://doi.org/10.1016/j.jqsrt.2012.02.028, 2012.

Bader, W., Bovy, B., Conway, S., Strong, K., Smale, D., Turner, A. J., Blumenstock, T., Boone, C., Collaud Coen, M., Coulon, A., Garcia, O., Griffith, D. W. T., Hase, F., Hausmann, P., Jones, N., Krummel, P., Murata, I., Morino, I., Nakajima, H., O'Doherty, S., Paton-Walsh, C., Robinson, J., Sandrin, R., Schneider, M., Servais, C., Sussmann, R., and Mahieu, E.: The recent increase of atmospheric methane from 10 years of ground-based NDACC FTIR observations since 2005, Atmos. Chem. Phys., 17, 2255–2277, https://doi.org/10.5194/acp-17-2255-2017, 2017.

Bergamaschi, P., Frankenberg, C., Meirink, J. F., Krol, M., Villani, M. G., Houweling, S., Dentener, F., Dlugokencky, E, J., Miller, J. B., Gatti, L. V., Engel, A., and Levin, I.: Inverse modeling of global and regional CH_4 emissions using SCIAMACHY satellite retrievals, J. Geophys. Res.-Atmos., 114, D22301, https://doi.org/10.1029/2009JD012287, 2009.

Bergamaschi, P., Houweling, S., Segers, A., Krol, M., Frankenberg, C., Scheepmaker, R. A., Dlugokencky, E., Wofsy, S. C., Kort, E. A., Sweeney, C., Schuck, T., Brenninkmeijer, C., Chen, H., Beck, V., and Gerbig, C.: Atmospheric CH_4 in the first decade of the 21st century: Inverse modeling analysis using SCIAMACHY satellite retrievals and NOAA surface measurements, J. Geophys. Res.-Atmos., 118, 7350–7369, https://doi.org/10.1002/jgrd.50480, 2013.

Blumenstock, T., Kopp, G., Hase, F., Hochschild, G., Mikuteit, S., Raffalski, U., and Ruhnke, R.: Observation of unusual chlorine activation by ground-based infrared and microwave spectroscopy in the late Arctic winter 2000/01, Atmos. Chem. Phys., 6, 897–905, https://doi.org/10.5194/acp-6-897-2006, 2006.

Blumstein, D., Chalon, G., Carlier, T., Buil, C., Hébert, P., Maciaszek, T., Ponce, G., Phulpin, T., Tournier, B., and Siméoni, D.: IASI instrument: Technical Overview and measured performances, in: Proccedings SPIE, SPIE, Denver, 2004.

Borger, C., Schneider, M., Ertl, B., Hase, F., García, O. E., Sommer, M., Höpfner, M., Tjemkes, S. A., and Calbet, X.: Evaluation of MUSICA MetOp/IASI tropospheric water vapour profiles by theoretical error assessments and comparisons to GRUAN Vaisala RS92 measurements, Atmos. Meas. Tech. Discuss., https://doi.org/10.5194/amt-2017-374, in review, 2017.

Bousquet, P., Ringeval, B., Pison, I., Dlugokencky, E. J., Brunke, E.-G., Carouge, C., Chevallier, F., Fortems-Cheiney, A., Frankenberg, C., Hauglustaine, D. A., Krummel, P. B., Langenfelds, R. L., Ramonet, M., Schmidt, M., Steele, L. P., Szopa, S., Yver, C., Viovy, N., and Ciais, P.: Source attribution of the changes in atmospheric methane for 2006–2008, Atmos. Chem. Phys., 11, 3689–3700, https://doi.org/10.5194/acp-11-3689-2011, 2011.

Clerbaux, C., Boynard, A., Clarisse, L., George, M., Hadji-Lazaro, J., Herbin, H., Hurtmans, D., Pommier, M., Razavi, A., Turquety, S., Wespes, C., and Coheur, P.-F.: Monitoring of atmospheric composition using the thermal infrared IASI/MetOp sounder, Atmos. Chem. Phys., 9, 6041–6054, https://doi.org/10.5194/acp-9-6041-2009, 2009.

Cressot, C., Chevallier, F., Bousquet, P., Crevoisier, C., Dlugokencky, E. J., Fortems-Cheiney, A., Frankenberg, C., Parker, R., Pison, I., Scheepmaker, R. A., Montzka, S. A., Krummel, P. B., Steele, L. P., and Langenfelds, R. L.: On the consistency between global and regional methane emissions inferred from SCIAMACHY, TANSO-FTS, IASI and surface measurements, Atmos. Chem. Phys., 14, 577–592, https://doi.org/10.5194/acp-14-577-2014, 2014.

Crevoisier, C., Nobileau, D., Fiore, A. M., Armante, R., Chédin, A., and Scott, N. A.: Tropospheric methane in the tropics – first year from IASI hyperspectral infrared observations, Atmos. Chem. Phys., 9, 6337–6350, https://doi.org/10.5194/acp-9-6337-2009, 2009.

Crevoisier, C., Nobileau, D., Armante, R., Crépeau, L., Machida, T., Sawa, Y., Matsueda, H., Schuck, T., Thonat, T., Pernin, J., Scott, N. A., and Chédin, A.: The 2007–2011 evolution of tropical methane in the mid-troposphere as seen from space by MetOp-A/IASI, Atmos. Chem. Phys., 13, 4279–4289, https://doi.org/10.5194/acp-13-4279-2013, 2013.

Crevoisier, C., Clerbaux, C., Guidard, V., Phulpin, T., Armante, R., Barret, B., Camy-Peyret, C., Chaboureau, J.-P., Coheur, P.-F., Crépeau, L., Dufour, G., Labonnote, L., Lavanant, L., Hadji-Lazaro, J., Herbin, H., Jacquinet-Husson, N., Payan, S., Péquignot, E., Pierangelo, C., Sellitto, P., and Stubenrauch, C.: Towards IASI-New Generation (IASI-NG): impact of improved spectral resolution and radiometric noise on the retrieval of thermodynamic, chemistry and climate variables, Atmos. Meas. Tech., 7, 4367–4385, https://doi.org/10.5194/amt-7-4367-2014, 2014.

Cuevas, E., Milford, C., Bustos, J. J., del Campo-Hernández, R., García, O. E., García, R. D., Gómez-Peláez, A. J., Ramos, R., Redondas, A., Reyes, E., Rodríguez, S., Romero-Campos, P. M., Schneider, M., Belmonte, J., Gil-Ojeda, M., Almansa, F., Alonso-Pérez, S., Barreto, A., González-Morales, Y., Guirado-Fuentes, C., López-Solano, C., Afonso, S., Bayo, C., Berjón, A., Bethencourt, J., Camino, C., Carreño, V., Castro, N. J., Cruz, A. M., Damas, M., De Ory-Ajamil, F., García, M. I., Fernández-de Mesa, C. M., González, Y., Hernández, C., Hernández, Y., Hernández, M. A., Hernández-Cruz, B., Jover, M., Kühl, S. O., López-Fernández, R., López-Solano, J., Peris, A., Rodríguez-Franco, J. J., Sálamo, C., Sepúlveda, E., and Sierra, M.: Izaña Atmospheric Research Center Activity Report 2012–2014, State Meteorological Agency (AEMET), Madrid, Spain, and World Meteorological Organization (WMO), Geneva, Switzerland, nIPO: 281-15-004-2, WMO/GAW Report No. 219, available at: http://izana.aemet.es, 2015.

De Mazière, M., Vigouroux, C., Bernath, P. F., Baron, P., Blumenstock, T., Boone, C., Brogniez, C., Catoire, V., Coffey, M., Duchatelet, P., Griffith, D., Hannigan, J., Kasai, Y., Kramer, I., Jones, N., Mahieu, E., Manney, G. L., Piccolo, C., Randall, C., Robert, C., Senten, C., Strong, K., Taylor, J., Tétard, C., Walker, K. A., and Wood, S.: Validation of ACE-FTS v2.2 methane profiles from the upper troposphere to the lower mesosphere, Atmos. Chem. Phys., 8, 2421–2435, https://doi.org/10.5194/acp-8-2421-2008, 2008.

De Mazière, M., Thompson, A. M., Kurylo, M. J., Wild, J. D., Bernhard, G., Blumenstock, T., Braathen, G. O., Hannigan, J. W., Lambert, J.-C., Leblanc, T., McGee, T. J., Nedoluha, G., Petropavlovskikh, I., Seckmeyer, G., Simon, P. C., Steinbrecht, W., and Strahan, S. E.: The Network for the Detection of Atmospheric Composition Change (NDACC): history, status and perspectives, Atmos. Chem. Phys., 18, 4935–4964, https://doi.org/10.5194/acp-18-4935-2018, 2018.

De Wachter, E., Kumps, N., Vandaele, A. C., Langerock, B., and De Mazière, M.: Retrieval and validation of MetOp/IASI methane, Atmos. Meas. Tech., 10, 4623–4638, https://doi.org/10.5194/amt-10-4623-2017, 2017.

Delamere, J. S., Clough, S. A., Payne, V. H., Mlawer, E. J., Turner, D. D., and Gamache, R. R.: A far-infrared radiative closure study in the Arctic: Application to water vapor, J. Geophys. Res.-Atmos., 115, D17106, https://doi.org/10.1029/2009JD012968, 2010.

EUMETSAT: IASI Level 2: Product Guide, EUM/OPS-EPS/MAN/04/0033, available at: http://www.eumetsat.int (last access: 11 July 2018), 2017.

Frankenberg, C., Meirink, J. F., Bergamaschi, P., Goede, A., Heimann, M., Korner, S., Platt, U., van Weele, M., and Wagner, T.: Satellite chartography of atmospheric methane from SCIAMACHY on board ENVISAT: Analysis of the years 2003 and 2004, J. Geophys. Res., 111, D07303, https://doi.org/10.1029/2005JD006235, 2006.

García, O. E., Sepúlveda, E., Schneider, M., Hase, F., August, T., Blumenstock, T., Kühl, S., Munro, R., Gómez-Peláez, Á. J., Hultberg, T., Redondas, A., Barthlott, S., Wiegele, A., González, Y., and Sanromá, E.: Consistency and quality assessment of the Metop-A/IASI and Metop-B/IASI operational trace gas products (O_3, CO, N_2O, CH_4, and CO_2) in the subtropical North Atlantic, Atmos. Meas. Tech., 9, 2315–2333, https://doi.org/10.5194/amt-9-2315-2016, 2016.

Gardiner, T., Forbes, A., de Mazière, M., Vigouroux, C., Mahieu, E., Demoulin, P., Velazco, V., Notholt, J., Blumenstock, T., Hase, F., Kramer, I., Sussmann, R., Stremme, W., Mellqvist, J., Strandberg, A., Ellingsen, K., and Gauss, M.: Trend analysis of greenhouse gases over Europe measured by a network of ground-based remote FTIR instruments, Atmos. Chem. Phys., 8, 6719–6727, https://doi.org/10.5194/acp-8-6719-2008, 2008.

Gordon, I. E., Rothman, L. S., Hill, C., Kochanov, R. V., Tan, Y., Bernath, P. F., Birk, M., Boudon, V., Campargue, A., Chance, K. V., Drouin, B. J., Flaud, J.-M., Gamache, R. R., Hodges, J. T., Jacquemart, D., Perevalov, V. I., Perrin, A., Shine, K. P., Smith, M.-A. H., Tennyson, J., Toon, G. C., Tran, H., Tyuterev, V. G., Barbe, A., Császár, A. G., Devi, V. M., Furtenbacher, T., Harrison, J. J., Hartmann, J.-M., Jolly, A., Johnson,T. J., Karman, T., Kleiner, I., Kyuberis, A. A., Loos, J., Lyulin, O. M., Massie,S. T., Mikhailenko, S. N., Moazzen-Ahmadi, N., Müller, H. S. P., Naumenko, O. V., Nikitin, A. V., Polyansky, O. L., Rey, M., Rotger, M., Sharpe, S. W., Sung, K., Starikova, E., Tashkun, S. A., Vander Auwera, J., Wagner, G., Wilzewski, J., Wcisło, P., Yu, S., and Zak, E. J.: The HITRAN2016 Molecular Spectroscopic Database, J. Quant. Spectrosc. Ra., 203, 3–69, https://doi.org/10.1016/j.jqsrt.2017.06.038, 2017.

Hase, F., Hanningan, J. W., Coffey, M. T., Goldman, A., Höfner, M., Jones, N. B., Rinsland, C. P., and Wood, S. W.: Intercomparison of retrieval codes used for the analysis of high-resolution ground-based FTIR measurements, J. Quant. Spectrosc. Ra., 87, 25–52, 2004.

Huang, J., Golombeck, A., Prinn, R., Weiss, R., Fraser, P., Simmonds, P., Dlugokencky, E., Hall, B., Elkins, J., Steele, P., Langenfelds, R., Krummel, P., Dutton, G., and Porter, L.: Estimation of regional emissions of nitrous oxide from 1997 to 2005 using multinetwork measurements, a chemical transport model, and an inverse method, J. Geophys. Res., 113, D17313, https://doi.org/10.1029/2007JD009381, 2008.

Kort, E. A., Patra, P. K., Ishijima, K., Daube, B. C., Jimenez, R., Elkins, J., Hurst, D., Moore, F. L., Sweeney, C., and Wofsy, S. C.: Tropospheric distribution and variability of N_2O: Evidence

for strong tropical emissions, Geophys. Res. Lett., 38, L15806, https://doi.org/10.1029/2011GL047612, 2011.

Masiello, G., Liuzzi, G., Serio, C., and Venafra, S.: Using the full IASI spectrum for the physical retrieval of Temperature, Water Vapour, Ozone and minor and trace gases: CO, CO_2, CH_4, N_2O, SO_2, HNO_3 and NH_3, IASI Conference 2016, Antibes Juan-les-Pins, France, 2016.

Massart, S., Agusti-Panareda, A., Aben, I., Butz, A., Chevallier, F., Crevoisier, C., Engelen, R., Frankenberg, C., and Hasekamp, O.: Assimilation of atmospheric methane products into the MACC-II system: from SCIAMACHY to TANSO and IASI, Atmos. Chem. Phys., 14, 6139–6158, https://doi.org/10.5194/acp-14-6139-2014, 2014.

Masuda, K., Takashima, T., and Takayama, Y.: Emissivity of pure and sea waters for the model sea surface in the infrared window regions, Remote Sensing Environment, 24, 313–329, https://doi.org/10.1016/0034-4257(88)90032-6, 1988.

Mlawer, E. J., Payne, V. H., Moncet, J.-L., Delamere, J. S., Alvarado, M. J., and Tobin, D. C.: Development and recent evaluation of the MT_CKD model of continuum absorption, Philos. T. Roy. Soc. A, 370, 2520–2556, https://doi.org/10.1098/rsta.2011.0295, 2012.

Nienerowski, K.: Qualitatssicherungs-Handbuch des UBA-Messnetzes, UBA Texte 28/04, (Handbook for quality assurance for the measurement network for the Federal Environmental Agency, Germany), Umweltbundesamt, Berlin, 2004.

Ostler, A., Sussmann, R., Rettinger, M., Deutscher, N. M., Dohe, S., Hase, F., Jones, N., Palm, M., and Sinnhuber, B.-M.: Multistation intercomparison of column-averaged methane from NDACC and TCCON: impact of dynamical variability, Atmos. Meas. Tech., 7, 4081–4101, https://doi.org/10.5194/amt-7-4081-2014, 2014.

Payan, S., Camy-Peyret, C., Oelhaf, H., Wetzel, G., Maucher, G., Keim, C., Pirre, M., Huret, N., Engel, A., Volk, M. C., Kuellmann, H., Kuttippurath, J., Cortesi, U., Bianchini, G., Mencaraglia, F., Raspollini, P., Redaelli, G., Vigouroux, C., De Mazière, M., Mikuteit, S., Blumenstock, T., Velazco, V., Notholt, J., Mahieu, E., Duchatelet, P., Smale, D., Wood, S., Jones, N., Piccolo, C., Payne, V., Bracher, A., Glatthor, N., Stiller, G., Grunow, K., Jeseck, P., Te, Y., and Butz, A.: Validation of version-4.61 methane and nitrous oxide observed by MIPAS, Atmos. Chem. Phys., 9, 413–442, https://doi.org/10.5194/acp-9-413-2009, 2009.

Payne, V. H., Mlawer, E. J., Cady-Pereira, K. E., and Moncet, J. L.: Water Vapor Continuum Absorption in the Microwave, IEEE T. Geosci. Remote, 49, 2194–2208, https://doi.org/10.1109/TGRS.2010.2091416, 2011.

Pequignot, E., Blumstein, D., and Larigauderie, C.: CNES Technical Note: IASI Noise Covariance Matrix, Tech. rep., 2008.

Plieninger, J., von Clarmann, T., Stiller, G. P., Grabowski, U., Glatthor, N., Kellmann, S., Linden, A., Haenel, F., Kiefer, M., Höpfner, M., Laeng, A., and Lossow, S.: Methane and nitrous oxide retrievals from MIPAS-ENVISAT, Atmos. Meas. Tech., 8, 4657–4670, https://doi.org/10.5194/amt-8-4657-2015, 2015.

Razavi, A., Clerbaux, C., Wespes, C., Clarisse, L., Hurtmans, D., Payan, S., Camy-Peyret, C., and Coheur, P. F.: Characterization of methane retrievals from the IASI space-borne sounder, Atmos. Chem. Phys., 9, 7889–7899, https://doi.org/10.5194/acp-9-7889-2009, 2009.

Ricaud, P., Attié, J.-L., Teyssèdre, H., El Amraoui, L., Peuch, V.-H., Matricardi, M., and Schluessel, P.: Equatorial total column of nitrous oxide as measured by IASI on MetOp-A: implications for transport processes, Atmos. Chem. Phys., 9, 3947–3956, https://doi.org/10.5194/acp-9-3947-2009, 2009.

Risi, C., Noone, D., Worden, J., Frankenberg, C., Stiller, G., Kiefer, M., Funke, B., Walker, K., Bernath, P., Schneider, M., Wunch, D., Sherlock, V., Deutscher, N., Griffith, D., Wennberg, P., Strong, K., Barthlott, S., Hase, F., Garcia, O., Smale, D., Mahieu, E., Sayres, D., Bony, S., Lee, J., Brown, D., Uemura, R., , and Sturm, C.: Process-evaluation of tropospheric humidity simulated by general circulation models using water vapor isotopic observations. Part 1: comparison between models and datasets, J. Geophys. Res., 117, D05303, https://doi.org/10.1029/2011JD016621, 2012.

Rodgers, C.: Inverse Methods for Atmospheric Sounding: Theory and Praxis, World Scientific Publishing Co., Singapore, 2000.

Rodgers, C. and Connor, B.: Intercomparison of remote sounding instruments, J. Geophys. Res., 108, 4116–4129, https://doi.org/10.1029/2002JD002299, 2003.

Rothman, L. S., Gordon, I. E., Barbe, A., Benner, D. C., Bernath, P. F., Birk, M., Boudon, V., Brown, L. R., Campargue, A., Champion, J.-P., Chance, K., Coudert, L. H., Dana, V., Devi, V. M., Fally, S., Flaud, J.-M., Gamache, R. R., Goldmanm, A., Jacquemart, D., Kleiner, I., Lacome, N., Lafferty, W., Mandin, J.-Y., Massie, S. T., Mikhailenko, S. N., Miller, C. E., Moazzen-Ahmadi, N., Naumenko, O. V., Nikitin, A. V., Orphal, J., Perevalov, V. I., A. Perrin, A. P.-C., Rinsland, C. P., Rotger, M., Šimečková, M., Smith, M. A. H., Sung, K., Tashkun, S. A., Tennyson, J., Toth, R. A., Vandaele, A. C., and VanderAuwera, J.: The HITRAN 2008 Molecular Spectroscopic Database, J. Quant. Spectrosc. Ra., 110, 533–572, 2009.

Santoni, G. W., Daube, B. C., Kort, E. A., Jiménez, R., Park, S., Pittman, J. V., Gottlieb, E., Xiang, B., Zahniser, M. S., Nelson, D. D., McManus, J. B., Peischl, J., Ryerson, T. B., Holloway, J. S., Andrews, A. E., Sweeney, C., Hall, B., Hintsa, E. J., Moore, F. L., Elkins, J. W., Hurst, D. F., Stephens, B. B., Bent, J., and Wofsy, S. C.: Evaluation of the airborne quantum cascade laser spectrometer (QCLS) measurements of the carbon and greenhouse gas suite – CO_2, CH_4, N_2O, and CO – during the CalNex and HIPPO campaigns, Atmos. Meas. Tech., 7, 1509–1526, https://doi.org/10.5194/amt-7-1509-2014, 2014.

Schneider, M. and Hase, F.: Optimal estimation of tropospheric H_2O and δD with IASI/METOP, Atmos. Chem. Phys., 11, 11207–11220, https://doi.org/10.5194/acp-11-11207-2011, 2011.

Schneider, M., Blumenstock, T., Chipperfield, M. P., Hase, F., Kouker, W., Reddmann, T., Ruhnke, R., Cuevas, E., and Fischer, H.: Subtropical trace gas profiles determined by ground-based FTIR spectroscopy at Izaña (28° N, 16° W): Five-year record, error analysis, and comparison with 3-D CTMs, Atmos. Chem. Phys., 5, 153–167, https://doi.org/10.5194/acp-5-153-2005, 2005.

Schneider, M., Hase, F., and Blumenstock, T.: Water vapour profiles by ground-based FTIR spectroscopy: study for an optimised retrieval and its validation, Atmos. Chem. Phys., 6, 811–830, https://doi.org/10.5194/acp-6-811-2006, 2006.

Schneider, M., Barthlott, S., Hase, F., González, Y., Yoshimura, K., García, O. E., Sepúlveda, E., Gomez-Pelaez, A., Gisi, M.,

Kohlhepp, R., Dohe, S., Blumenstock, T., Wiegele, A., Christner, E., Strong, K., Weaver, D., Palm, M., Deutscher, N. M., Warneke, T., Notholt, J., Lejeune, B., Demoulin, P., Jones, N., Griffith, D. W. T., Smale, D., and Robinson, J.: Ground-based remote sensing of tropospheric water vapour isotopologues within the project MUSICA, Atmos. Meas. Tech., 5, 3007–3027, https://doi.org/10.5194/amt-5-3007-2012, 2012.

Schneider, M., González, Y., Dyroff, C., Christner, E., Wiegele, A., Barthlott, S., García, O. E., Sepúlveda, E., Hase, F., Andrey, J., Blumenstock, T., Guirado, C., Ramos, R., and Rodríguez, S.: Empirical validation and proof of added value of MUSICA's tropospheric δD remote sensing products, Atmos. Meas. Tech., 8, 483–503, https://doi.org/10.5194/amt-8-483-2015, 2015.

Schneider, M., Wiegele, A., Barthlott, S., González, Y., Christner, E., Dyroff, C., García, O. E., Hase, F., Blumenstock, T., Sepúlveda, E., Mengistu Tsidu, G., Takele Kenea, S., Rodríguez, S., and Andrey, J.: Accomplishments of the MUSICA project to provide accurate, long-term, global and high-resolution observations of tropospheric {H2O,dD} pairs – a review, Atmos. Meas. Tech., 9, 2845–2875, https://doi.org/10.5194/amt-9-2845-2016, 2016.

Seemann, S., Borbas, E., Knuteson, R., Stephenson, G., and Huang, H.-L.: Development of a Global Infrared Land Surface Emissivity Database for Application to Clear Sky Sounding Retrievals from Multispectral Satellite Radiance Measurements, J. Appl. Meteorol. Clim., 47, 108–123, https://doi.org/10.1175/2007JAMC1590.1, 2008.

Sepúlveda, E., Schneider, M., Hase, F., García, O. E., Gomez-Pelaez, A., Dohe, S., Blumenstock, T., and Guerra, J. C.: Long-term validation of tropospheric column-averaged CH_4 mole fractions obtained by mid-infrared ground-based FTIR spectrometry, Atmos. Meas. Tech., 5, 1425–1441, https://doi.org/10.5194/amt-5-1425-2012, 2012.

Sepúlveda, E., Schneider, M., Hase, F., Barthlott, S., Dubravica, D., García, O. E., Gomez-Pelaez, A., González, Y., Guerra, J. C., Gisi, M., Kohlhepp, R., Dohe, S., Blumenstock, T., Strong, K., Weaver, D., Palm, M., Sadeghi, A., Deutscher, N. M., Warneke, T., Notholt, J., Jones, N., Griffith, D. W. T., Smale, D., Brailsford, G. W., Robinson, J., Meinhardt, F., Steinbacher, M., Aalto, T., and Worthy, D.: Tropospheric CH_4 signals as observed by NDACC FTIR at globally distributed sites and comparison to GAW surface in situ measurements, Atmos. Meas. Tech., 7, 2337–2360, https://doi.org/10.5194/amt-7-2337-2014, 2014.

Siddans, R., Knappett, D., Kerridge, B., Waterfall, A., Hurley, J., Latter, B., Boesch, H., and Parker, R.: Global height-resolved methane retrievals from the Infrared Atmospheric Sounding Interferometer (IASI) on MetOp, Atmos. Meas. Tech., 10, 4135–4164, https://doi.org/10.5194/amt-10-4135-2017, 2017.

Stocker, T. F., Qin, D., Plattner, G.-K., Tignor, M., Allen, S. K., Boschung, J., Nauels, A., Xia, Y., Bex, V., and Midgley, P. M.: Climate Change 2013: The Physical Science Basis, Tech. rep., 1535 pp., 2013.

Tikhonov, A.: On the solution of incorrectly stated problems and a method of regularization, Dokl. Acad. Nauk SSSR, 151, 501–504, 1963.

Turquety, S., Hadji-Lazaro, J., Clerbaux, C., Hauglustaine, D., Clough, S. A., Cassé, V., Schulüssel, P., and Mégie, G.: Operational trace gas retrieval algorithm for the Infrared Atmospheric Sounding Interferometer, J. Geophys. Res., 109, D21301, https://doi.org/10.1029/2004JD004821, 2004.

Wecht, K. J., Jacob, D. J., Wofsy, S. C., Kort, E. A., Worden, J. R., Kulawik, S. S., Henze, D. K., Kopacz, M., and Payne, V. H.: Validation of TES methane with HIPPO aircraft observations: implications for inverse modeling of methane sources, Atmos. Chem. Phys., 12, 1823–1832, https://doi.org/10.5194/acp-12-1823-2012, 2012.

Wiegele, A., Schneider, M., Hase, F., Barthlott, S., García, O. E., Sepúlveda, E., González, Y., Blumenstock, T., Raffalski, U., Gisi, M., and Kohlhepp, R.: The MUSICA MetOp/IASI H_2O and δD products: characterisation and long-term comparison to NDACC/FTIR data, Atmos. Meas. Tech., 7, 2719–2732, https://doi.org/10.5194/amt-7-2719-2014, 2014.

WMO: 18th WMO/IAEA Meeting on Carbon Dioxide, Other Greenhouse Gases and Related Tracers Measurement Techniques (GGMT-2015), La Jolla, CA, USA, 13–17 September 2015, GAW Report No. 229, World Meteorological Organization, Geneva, Switzerland, 2016.

Wofsy, S. C., the HIPPO Science Team, Modellers, C., and Teams, S.: HIAPER Pole-to-Pole Observations (HIPPO): fine-grained, global-scale measurements of climatically important atmospheric gases and aerosols, Philos. T. Roy. Soc. A, 369, 2073–2086, 2011.

Worden, J., Kulawik, S., Frankenberg, C., Payne, V., Bowman, K., Cady-Peirara, K., Wecht, K., Lee, J.-E., and Noone, D.: Profiles of CH_4, HDO, H_2O, and N_2O with improved lower tropospheric vertical resolution from Aura TES radiances, Atmos. Meas. Tech., 5, 397–411, https://doi.org/10.5194/amt-5-397-2012, 2012.

Wunch, D., Toon, G. C., Blavier, J.-F. L., Washenfelder, R. A., Notholt, J., Connor, B. J., Griffith, D. W. T., Sherlock, V., and Wennberg, P. O.: The total carbon column observing network, Philos. T. Roy. Soc. A, 369, 2087–112, https://doi.org/10.1098/rsta.2010.0240, 2011.

Xiong, X., Barnet, C., Maddy, E. S., Gambacorta, A., King, T. S., and Wofsy, S. C.: Mid-upper tropospheric methane retrieval from IASI and its validation, Atmos. Meas. Tech., 6, 2255–2265, https://doi.org/10.5194/amt-6-2255-2013, 2013.

Xiong, X., Maddy, E., C., B., Gambacorta, A., Patra, P., Sun, F., and Goldberg, M.: Retrieval of nitrous oxide from Atmospheric Infrared Sounder: Characterization and validation, J. Geophys. Res.-Atmos., 119, https://doi.org/10.1002/2013JD021406, 2014.

Xiong, X., Weng, F., Liu, Q., and Olsen, E.: Space-borne observation of methane from atmospheric infrared sounder version 6: validation and implications for data analysis, Atmos. Meas. Tech. Discuss., 8, 8563–8597, https://doi.org/10.5194/amtd-8-8563-2015, 2015.

Yokota, T., Yoshida, Y., Eguchi, N., Ota, Y., Tanaka, T., Watanabe, H., , and Maksyutov, S.: Global Concentrations of CO_2 and CH_4 Retrieved from GOSAT: First Preliminary Results, SOLA, 5, 160–163, https://doi.org/10.2151/sola.2009-041, 2009.